Draw Your Mission to (16) Psyche Storyboard Book

Plan your journey with Dr. Lindy Elkins-Tanton by exploring what she thinks are the 16 most important things about the Psyche Mission

Artwork by Psyche Inspired Intern
AARTI PATEL

Artwork by Psyche Inspired Intern
NOAH KEIME

The first 16 asteroids discovered

Color in the asteroids of how you think they look up close.

1. The Psyche asteroid was the 16th asteroid discovered.

2. Annibale de Gasparis, the astronomer who discovered Psyche in 1852, named the asteroid after the Greek goddess of the soul.

GODDESS PSYCHE AND PSYCHE

Artwork by Psyche
Inspired Intern
CHRISTINE ZHOU

ANNIBALE DE GASPARIS

3. If Psyche were a perfect sphere, it would be about the length of the state of Massachusetts (leaving out Cape Cod).

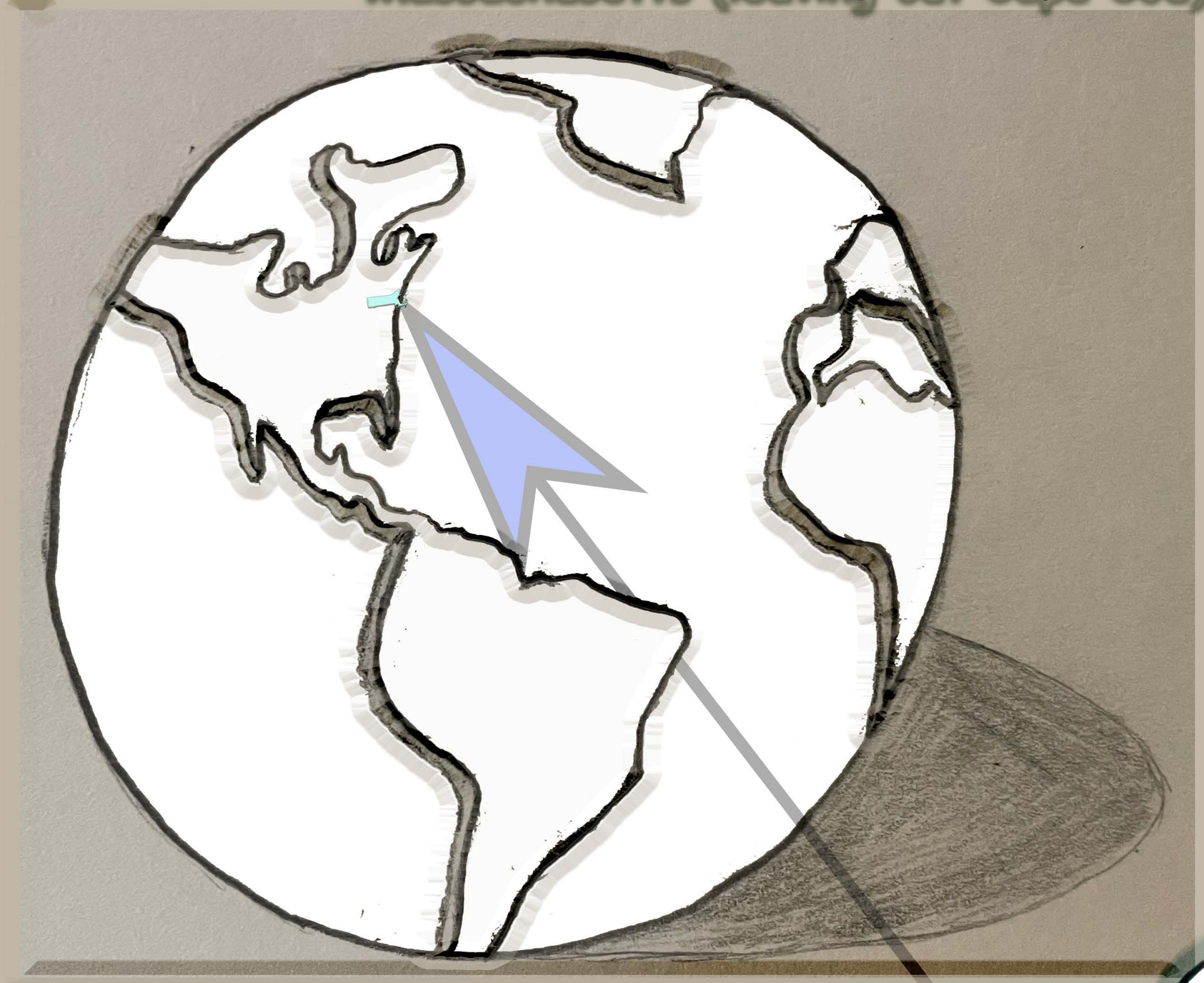

The arrow is pointing to where Massachusetts is on the globe with its approximate size.

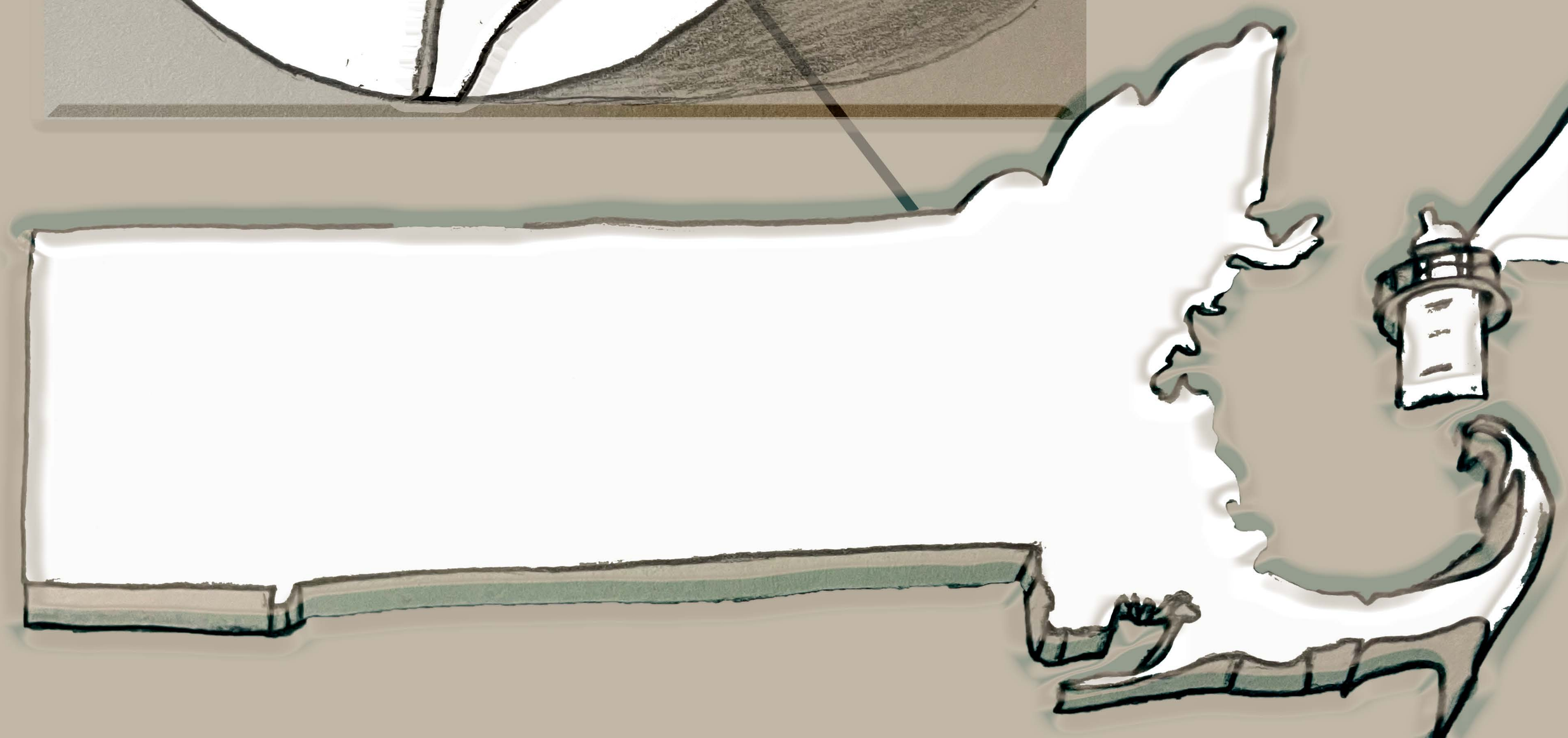

4. The Psyche asteroid is hypothesized to be made largely of metal.

Color the Psyche Asteroid

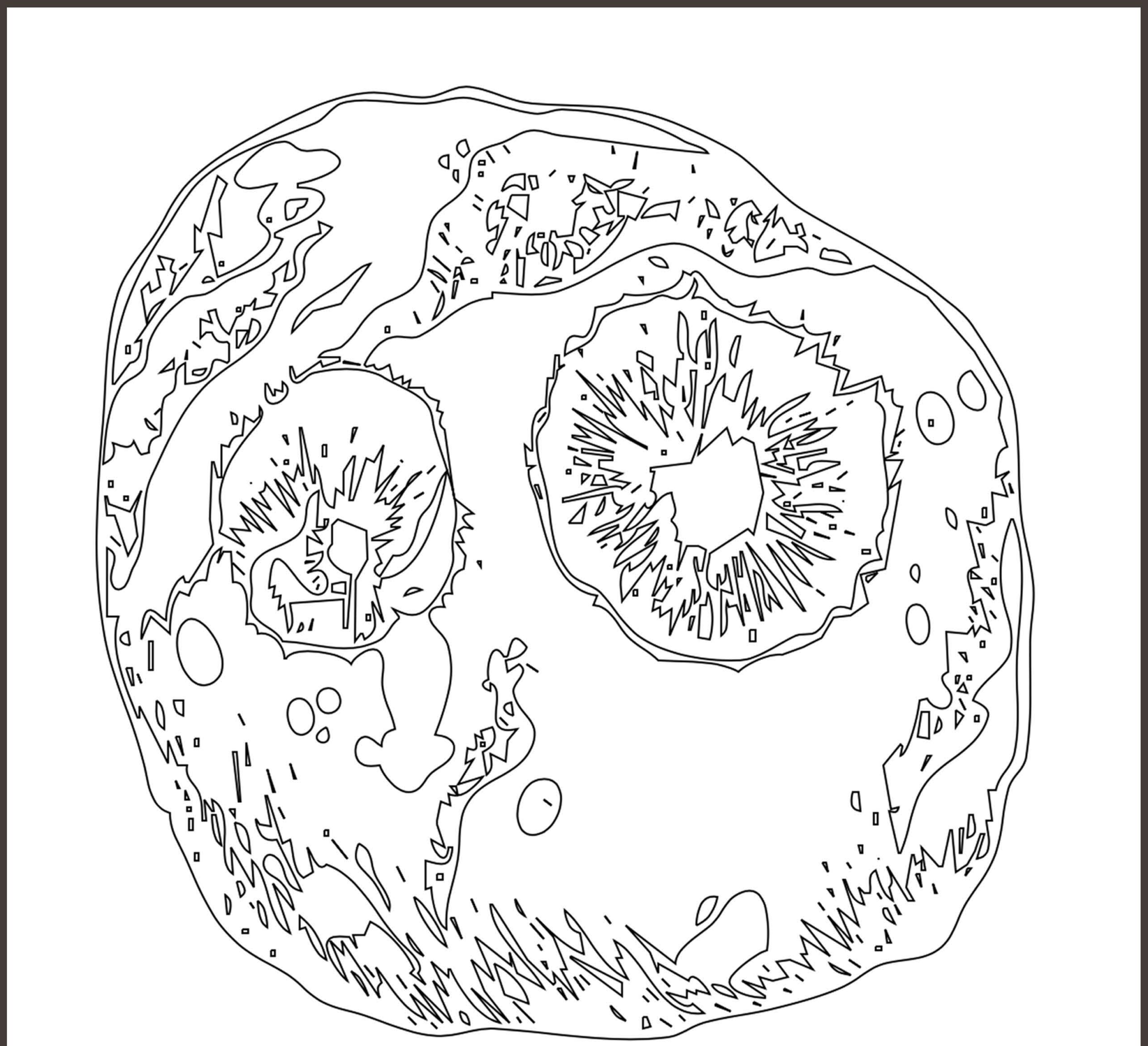

Periodic Table of Psyche

1 H 1.0078																	2 He 4.0026
3 Li 6.938	4 Be 9.0122											5 B 10.806	6 C 12.009	7 N 14.006	8 O 15.999	9 F 18.998	10 Ne 20.180
11 Na 22.990	12 Mg 24.305											13 Al 26.982	14 Si 28.084	15 P 30.974	16 S 32.059	17 Cl 35.446	18 Ar 39.948
19 K 39.098	20 Ca 40.078	21 Sc 44.956	22 Ti 47.867	23 V 50.942	24 Cr 51.996	25 Mn 54.938	26 Fe 55.845	27 Co 58.933	28 Ni 58.693	29 Cu 63.546	30 Zn 65.38	31 Ga 69.723	32 Ge 72.63	33 As 74.922	34 Se 78.96	35 Br 79.904	36 Kr 83.798
37 Rb 85.468	38 Sr 87.62	39 Y 88.906	40 Zr 91.224	41 Nb 92.906	42 Mo 95.96	43 Tc 98.9062	44 Ru 101.07	45 Rh 102.91	46 Pd 106.42	47 Ag 107.87	48 Cd 112.41	49 In 114.82	50 Sn 118.71	51 Sb 121.76	52 Te 127.60	53 I 126.90	54 Xe 131.29
55 Cs 132.91	56 Ba 137.33		72 Hf 178.49	73 Ta 180.95	74 W 183.84	75 Re 186.21	76 Os 190.23	77 Ir 192.22	78 Pt 195.08	79 Au 196.97	80 Hg 200.59	81 Tl 204.83	82 Pb 207.2	83 Bi 208.98	84 Po (209)	85 At (210)	86 Rn (222)
87 Fr (223)	88 Ra (226)		104 Rf (261)	105 Db (262)	106 Sg (266)	107 Bh (264)	108 Hs (269)	109 Mt (268)	110 Ds (268)	111 Rg (268)	112 Cn (268)	113 Uut (268)	114 Fl (268)	115 Uup (268)	116 Lv (268)	117 Uus (268)	118 Uuo (268)

57 La 138.91	58 Ce 140.12	59 Pr 140.91	60 Nd 144.24	61 Pm (145)	62 Sm 150.36	63 Eu 151.96	64 Gd 157.25	65 Tb 158.93	66 Dy 162.50	67 Ho 164.93	68 Er 167.26	69 Tm 168.93	70 Yb 173.04	71 Lu 174.97
89 Ac (227)	90 Th 232.04	91 Pa 231.04	92 U 238.03	93 Np (237)	94 Pu (244)	95 Am (243)	96 Cm (247)	97 Bk (247)	98 Cf (251)	99 Es (252)	100 Fm (257)	101 Md (258)	102 No (259)	103 Lr (262)

Draw your own pattern in the Fe (Iron) and Ni (Nickel) superimposed (large) images. Then tell what other elements you think Psyche could be made of.

5. THE PSYCHE MISSION IS THE FIRST MISSION TO VISIT A PLANETARY BODY HYPOTHESIZED TO BE MADE LARGELY OF METAL.

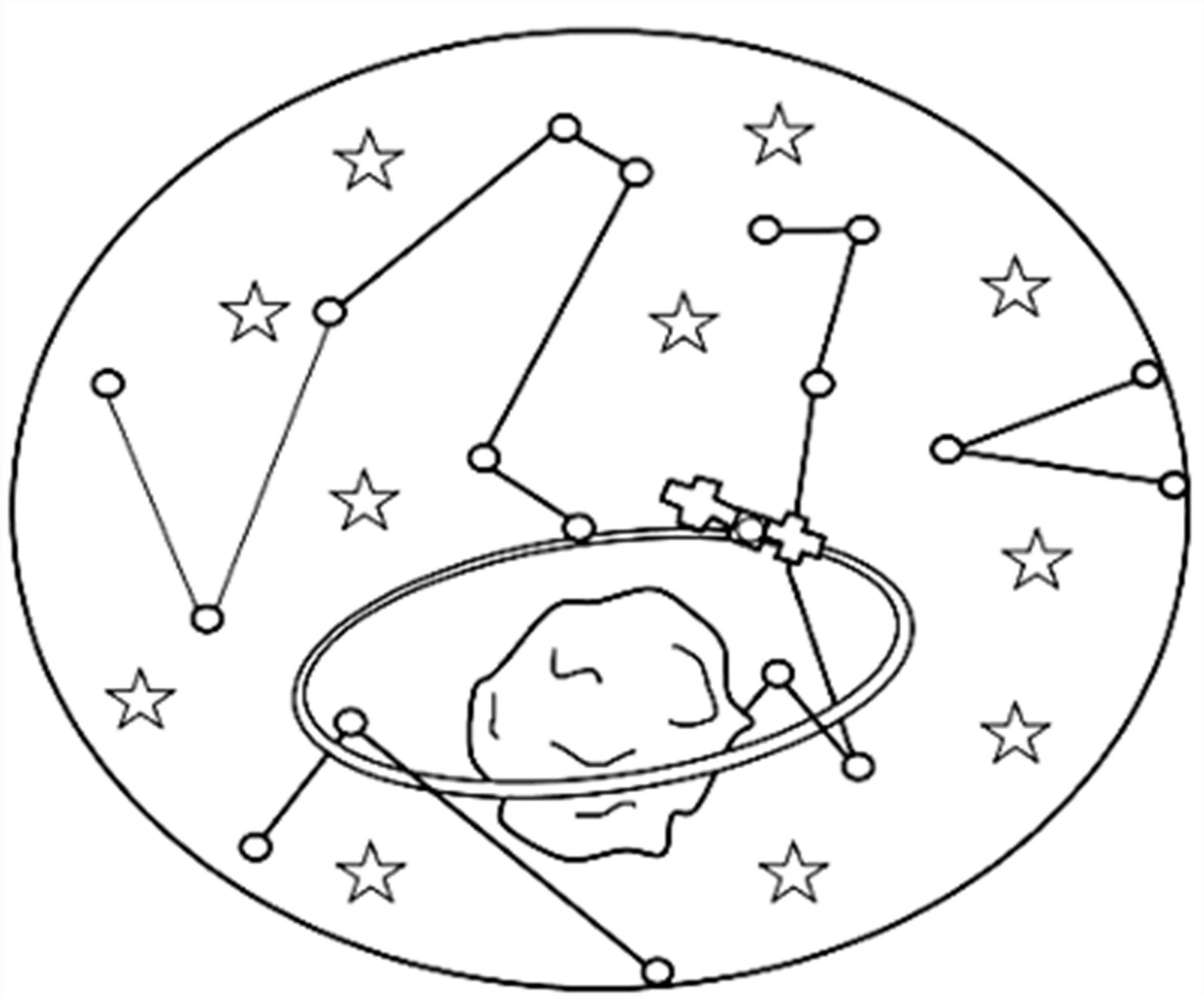

Artwork by Psyche Inspired Intern
CARALIE CEDARLEAF

In the space, draw the Psyche spacecraft on its way to the Psyche asteroid as it passes by Mars for its gravity assist.

7

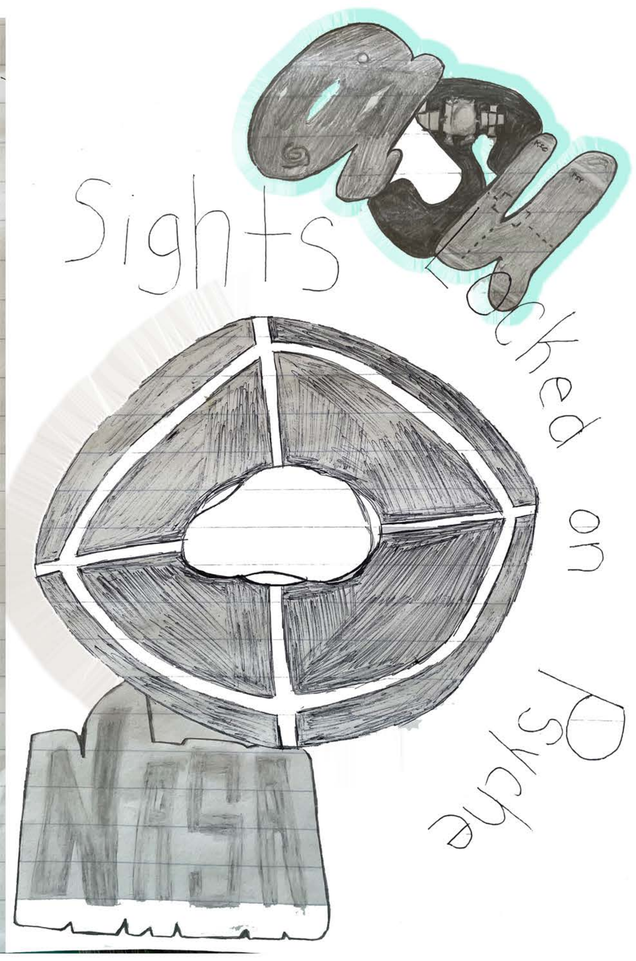

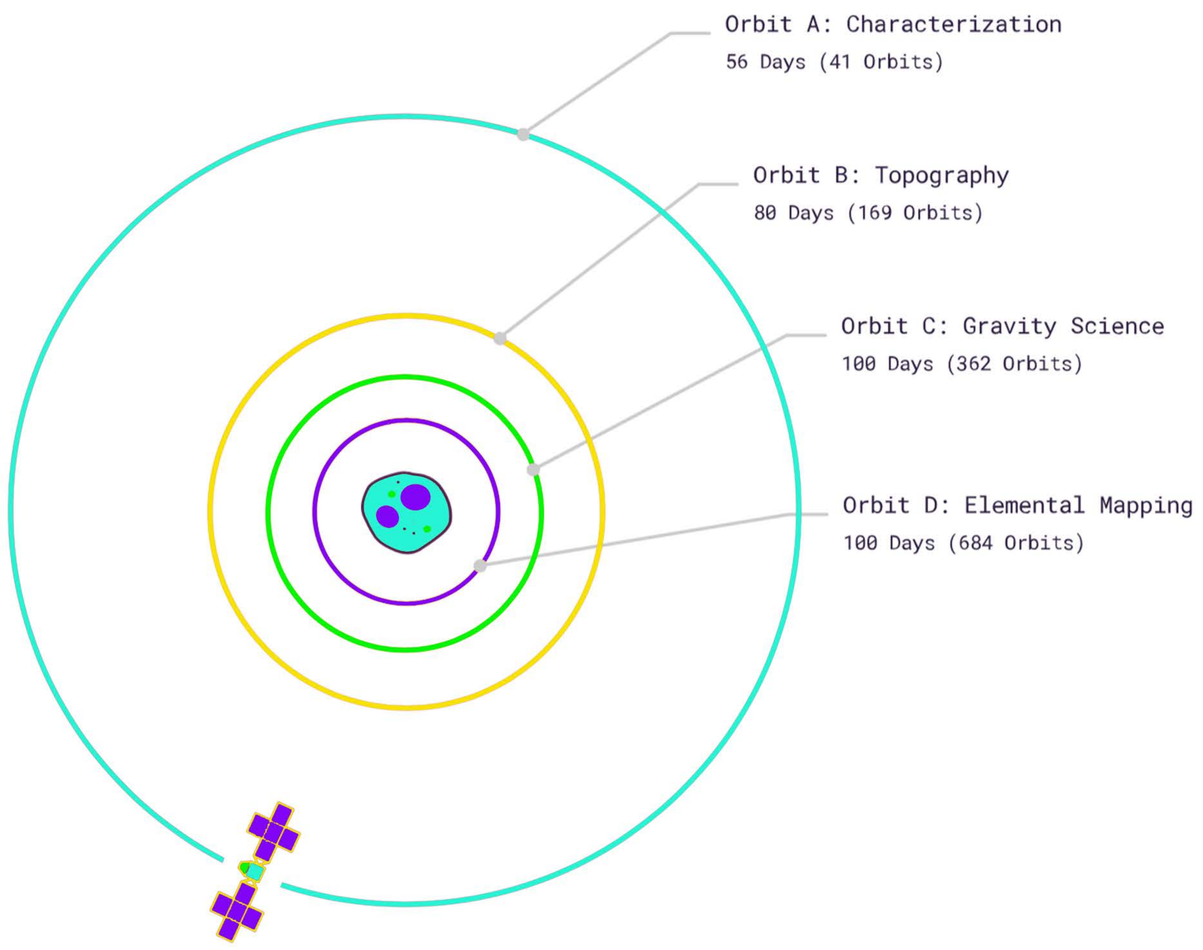

https://psyche.asu.edu/mission/launch/

6. Psyche's metal-rich composition may provide clues on planetary formation.

Dr. Lindy Elkins-Tanton, et. al, suggests the occurrence of planetary formation from about 5 billion years ago to the present time of the solar system. It is believed that giant molecular clouds collapsed due to shock, leading to the formation of protoplanetary disks. At about 4.5673 billion years, the first solids formed. Emmanuel Swedenborg's (1734) Principia Rerum Naturalium theorized that planets came from the Sun via centrifugal expulsion. It is also believed that planets formed from calcium aluminum inclusion.You can find more information about Building Planets with Dr. Lindy Elkins-Tanton's talk visit: https://youtu.be/B5xgifnw_3g

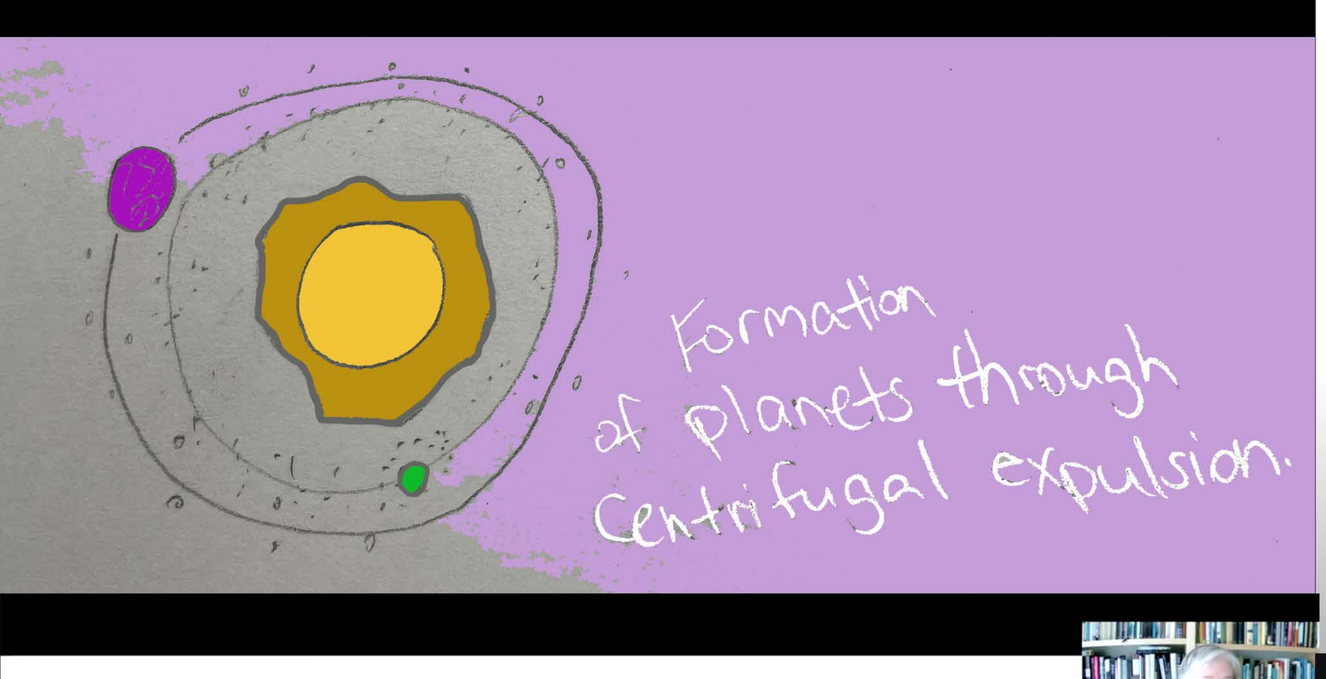

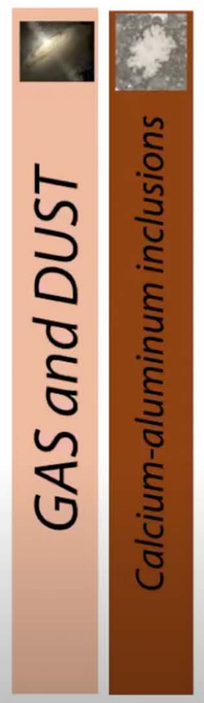

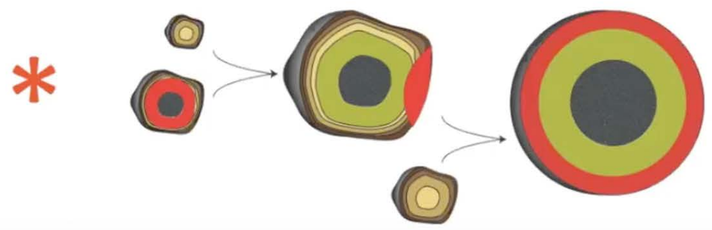

Accretion of gas and dust into planetesimals. The red section is molten.

Elkins-Tanton (2012) Ann.Rev.

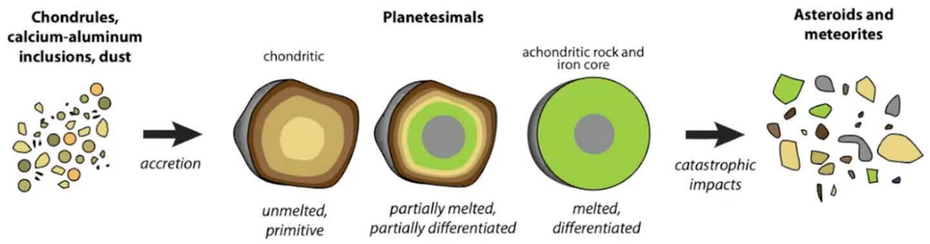

Artwork by Psyche Inspired Intern JOHN DOMENICO

Draw your own planet formation. Feel free to look online for more resources.

7. Aside from meteorites, the Psyche asteroid may be the only other way to directly observe material that may be similar in composition to a planetary core.

Draw what other ways you think planets can form.

8. It is hypothesized that Psyche may have been formed from a large impact that stripped a protoplanet of its outer crust and mantle.

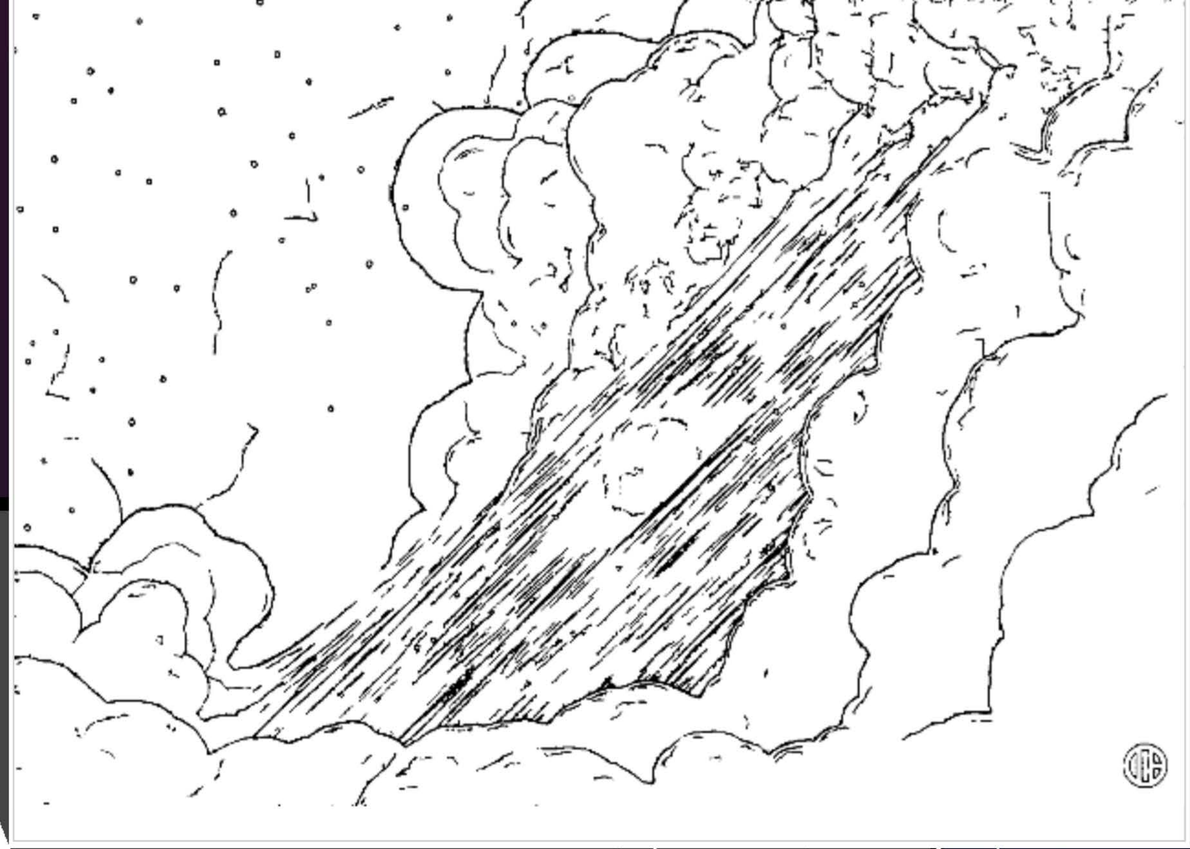

Artwork by Psyche Inspired Intern
SAM HOLLASCH

Draw what you think the impact looked like.

9. If it is not a remnant (left-over) core, the next most likely thing Psyche could be is something totally unexpected that scientists currently don't have an analog for.

Draw what you think Psyche could look like

10.Psyche has a large, diverse team spread around the world fulfilling important roles for the success of the mission!

Artwork by Psyche Inspied
Ben Conway

United States of America

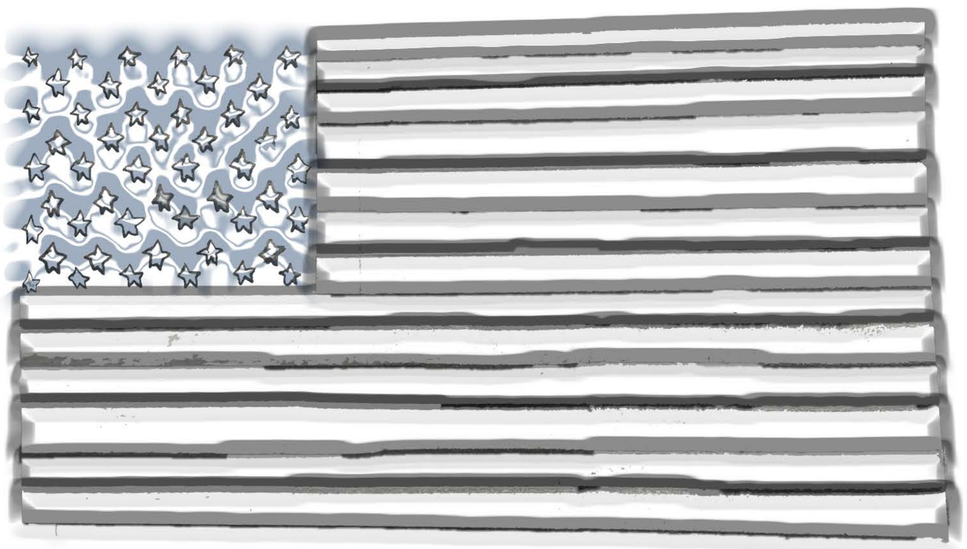

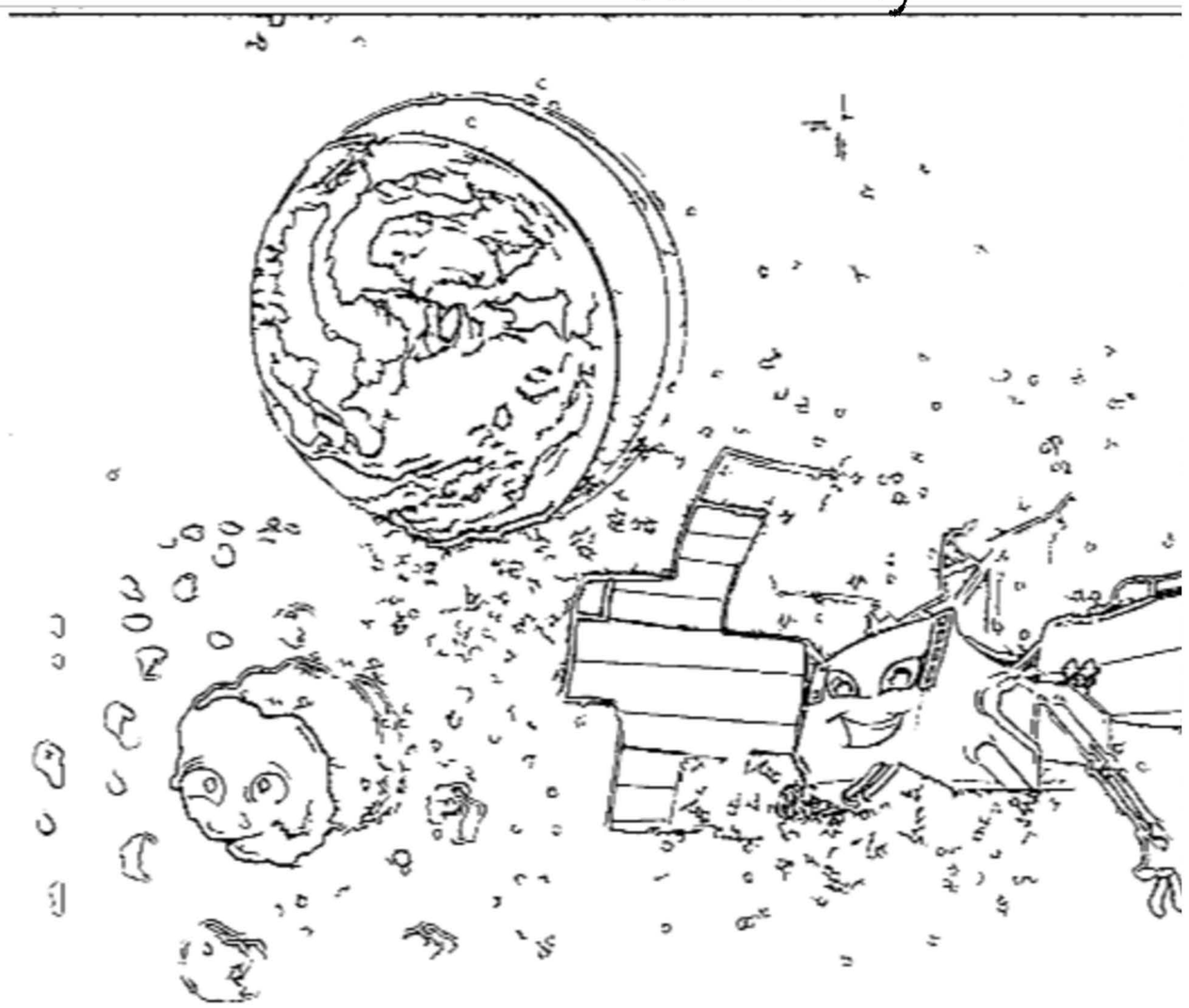

Denmark

France

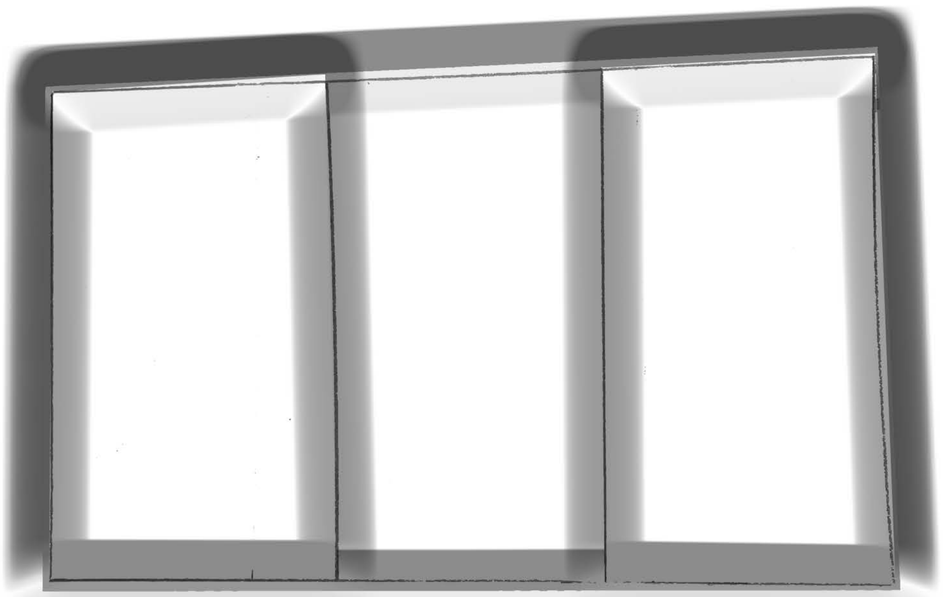

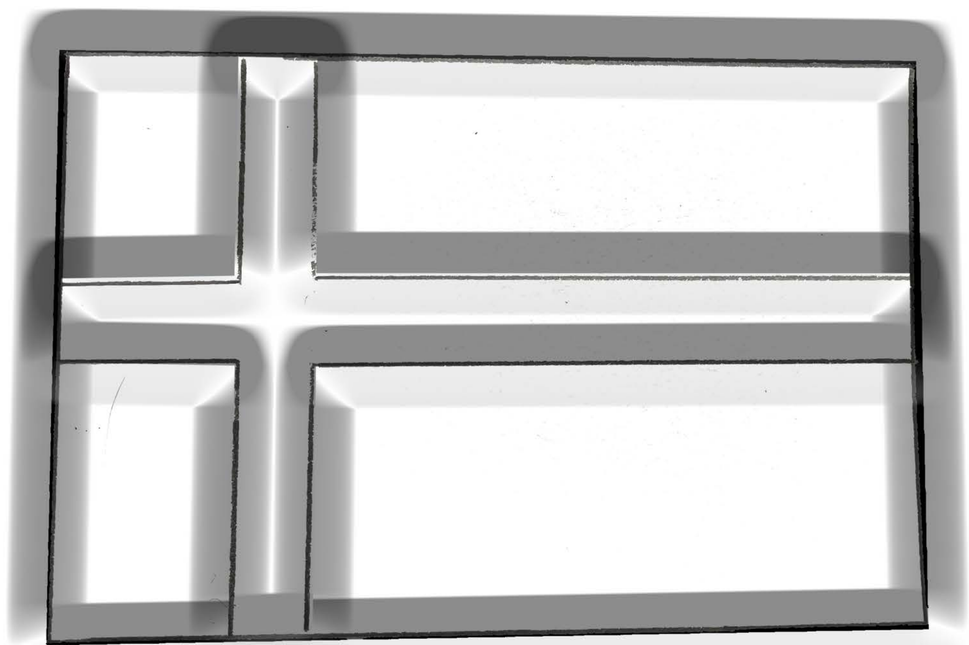

11.The Psyche spacecraft is set to be launched on a Falcon Heavy rocket from Launch Complex 39A at Cape Canaveral Air Force Station in Florida.

16 Draw what you think it would be like to watch a rocket launch.

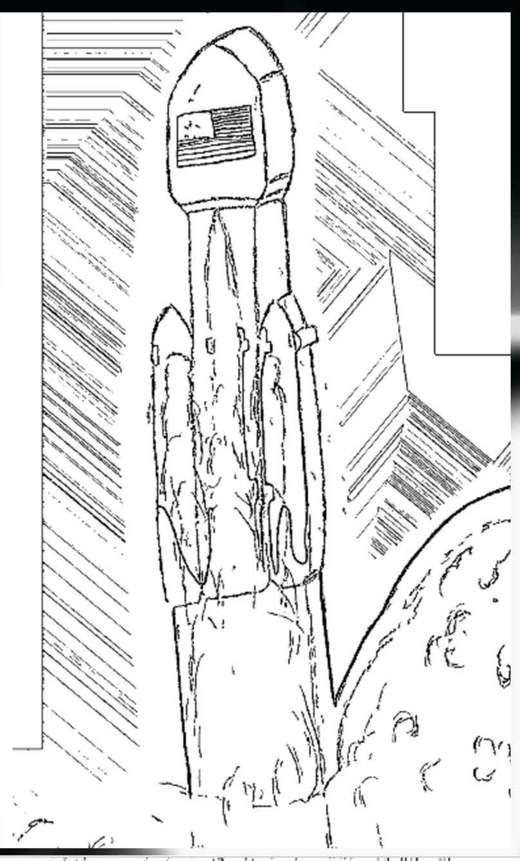

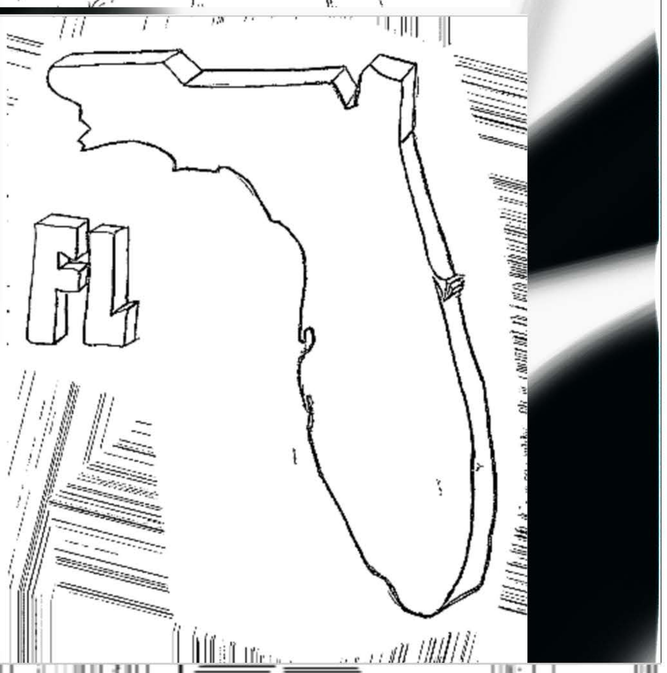

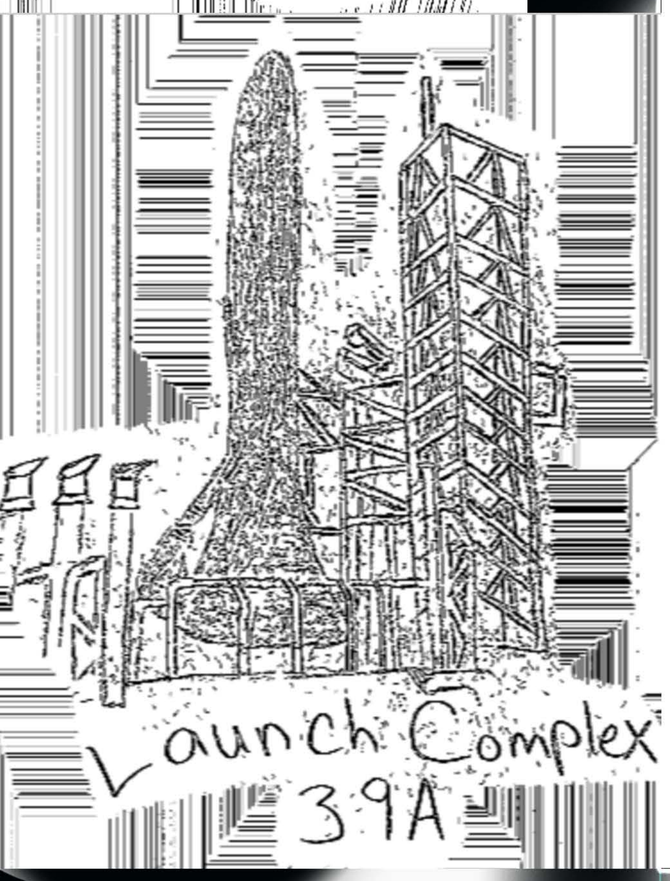

12.The spacecraft will launch in August of 2022, and it will arrive at the Psyche asteroid in January of 2026.

Launch Month

	1	2	3	4	5	6
7	8	9	10	11	12	13
14	15	16	17	18	19	20
21	22	23	24	25	26	27
28	29	30	31			

August 2022

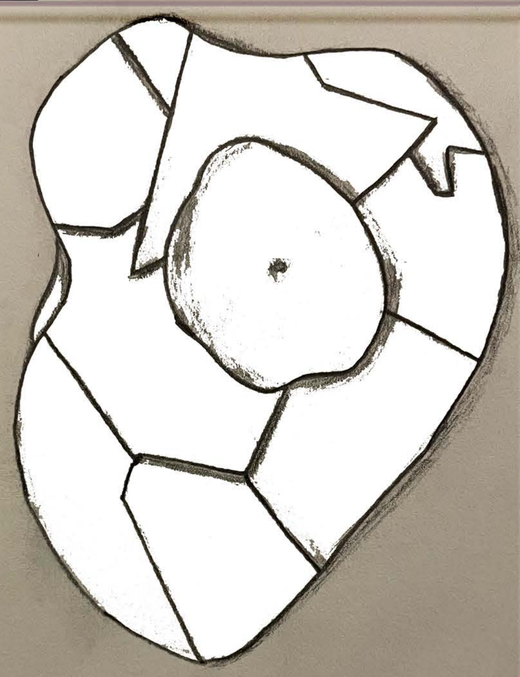

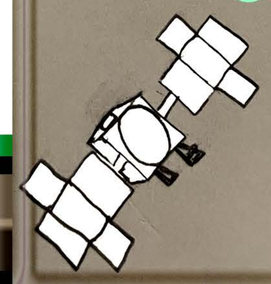

Color in the calendrs with what you think will happen on each day.

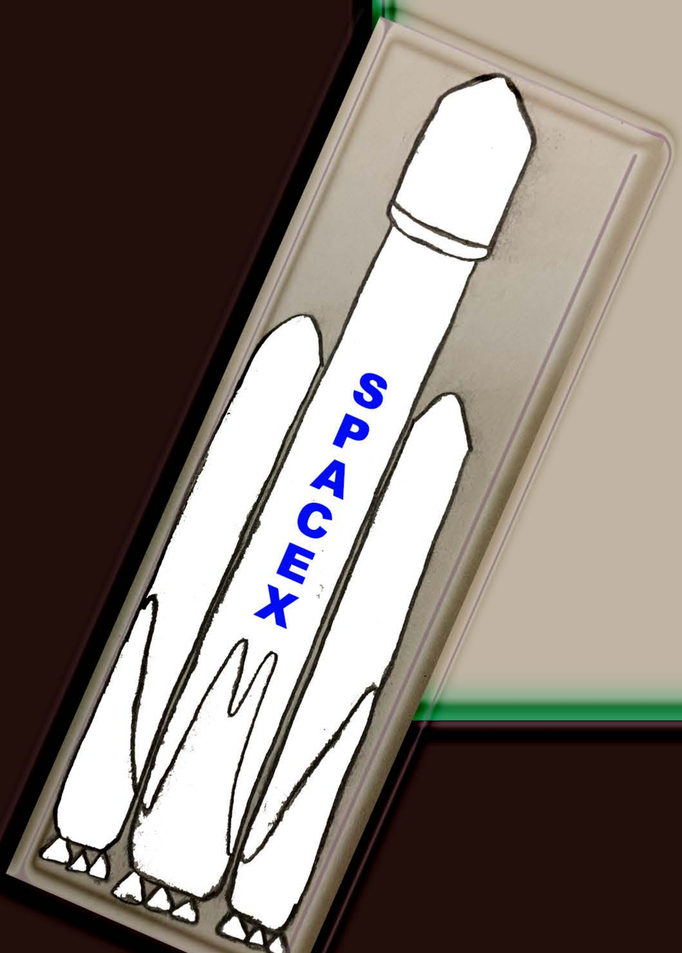

					1	2	3
4	5	6	7	8	9	10
11	12	13	14	15	16	17
18	19	20	21	22	23	24
25	26	27	28	29	30	31

January 2026

Arrival Month

13.The spacecraft will travel through space using solar electric propulsion.

Image Credit: Maxar

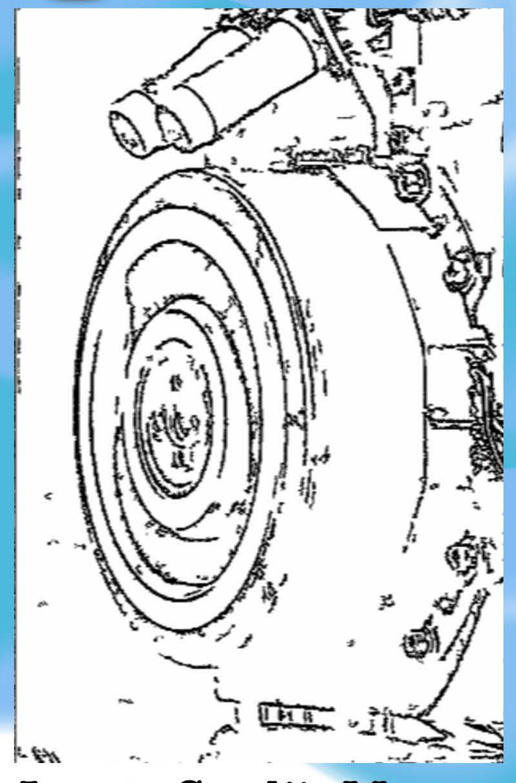

Image Credit: Maxar

Draw your own spacecraft engines here

14.ON ITS WAY TO THE ASTEROID, THE PSYCHE SPACECRAFT WILL RECEIVE A GRAVITY ASSIST FROM MARS IN MAY 2023.

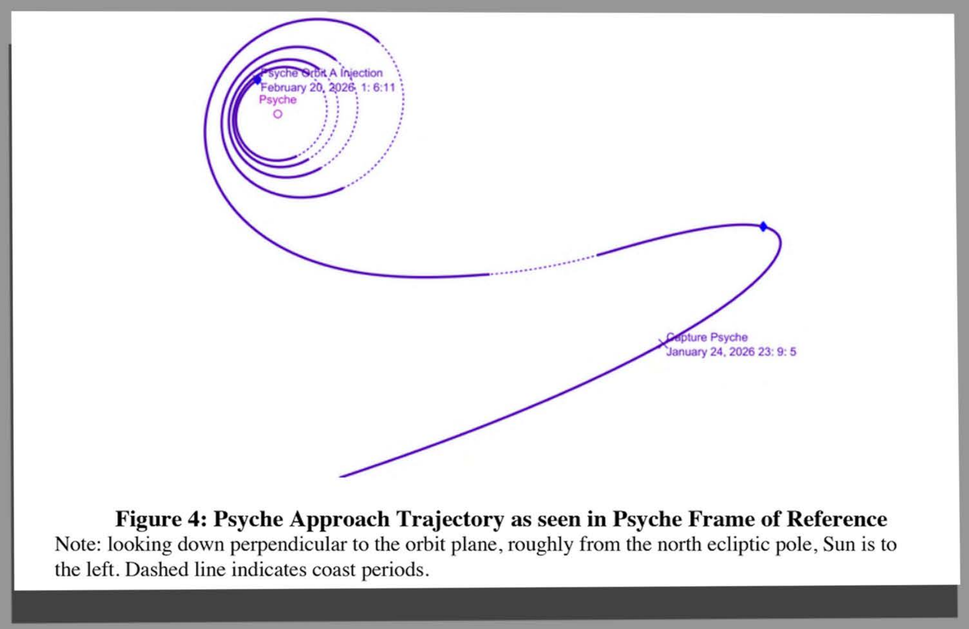

Figure 4: Psyche Approach Trajectory as seen in Psyche Frame of Reference
Note: looking down perpendicular to the orbit plane, roughly from the north ecliptic pole, Sun is to the left. Dashed line indicates coast periods.

Oh, D. et al., 2019

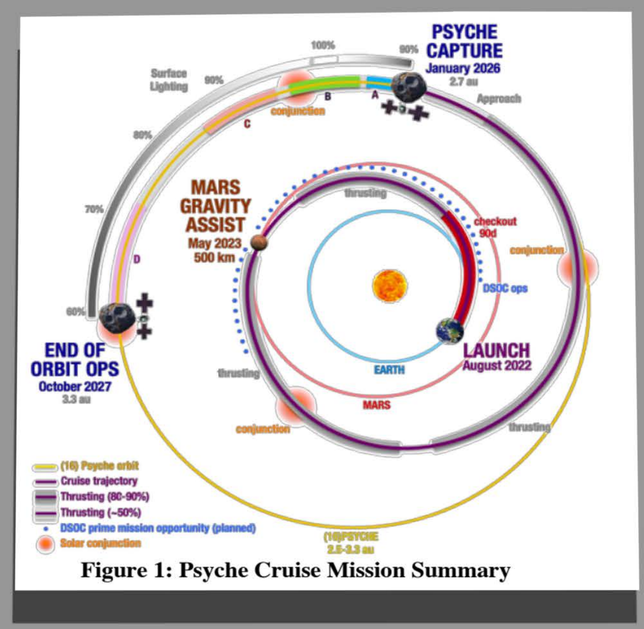

Figure 1: Psyche Cruise Mission Summary

Oh, D. et al., 2019

IMAGINATION STATION: IF YOU WERE TO FLY BY MARS, WHAT WOULD YOU WANT TO SEE AS YOU PASSED?

15.The Psyche spacecraft will carry a multispectral imager, a gamma ray and neutron spectrometer, and a magnetometer, and will conduct radio science.

Psyche Spacecraft: High Gain Antenna

Image Credit: Maxar

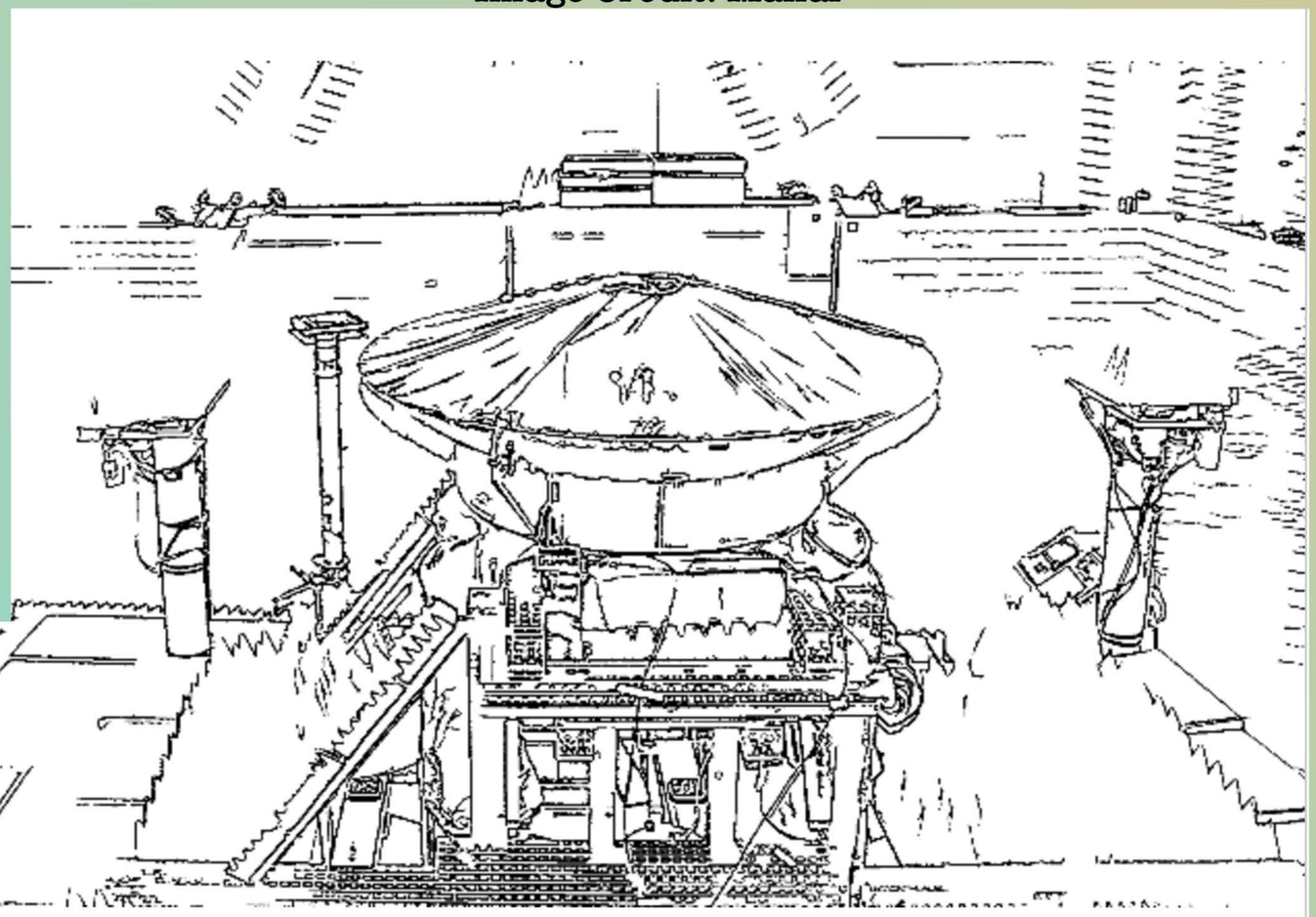

Psyche Multispectral Imager Filter Wheel

Image Credit: Arizona State University/Malin Space Science Systems/Motiv

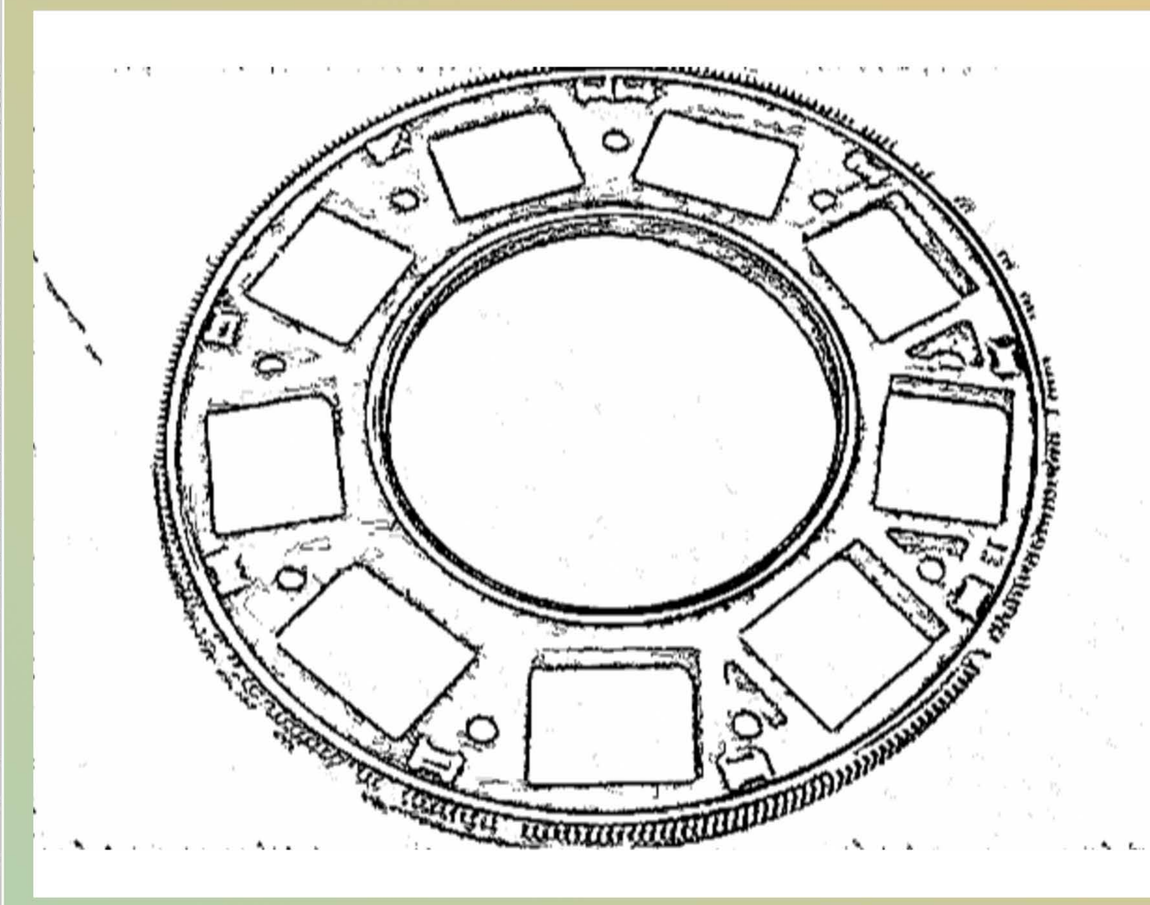

Psyche Spacecraft: Main Body

Image Credit: Maxar

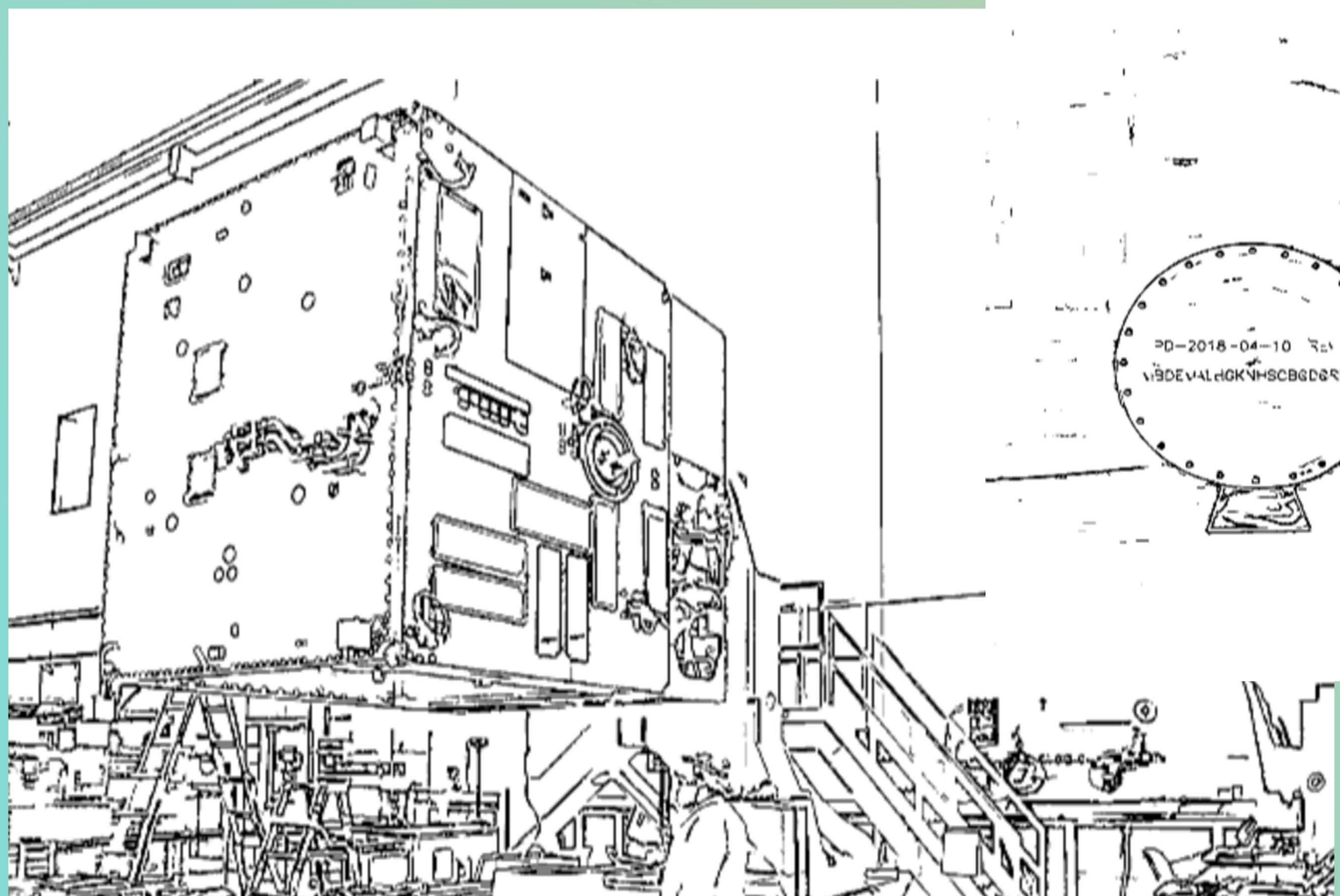

Gamma Ray Spectrometer

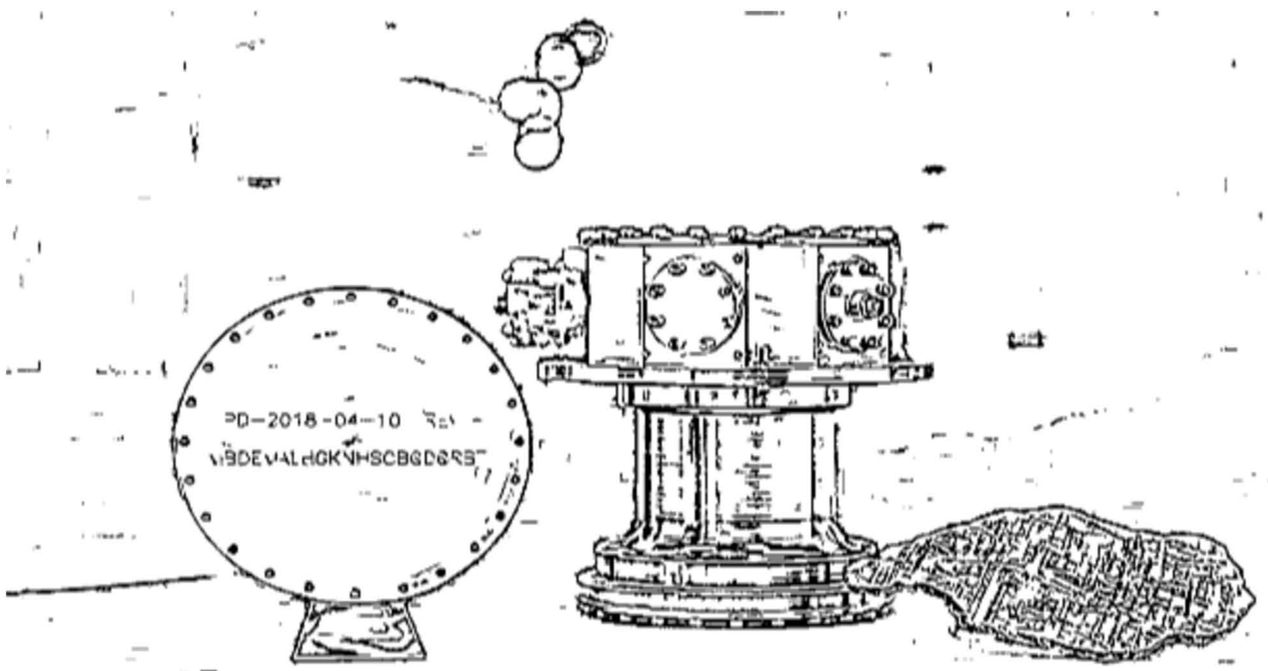

Morgan Burks & Garry McLeod, Lawrence Livermore National Labs (LLNL)

16.The Psyche spacecraft will test a new communication technology, Deep Space Optical Communication (DSOC), that allows the spacecraft to communicate more data in a given amount of time through the use of lasers.

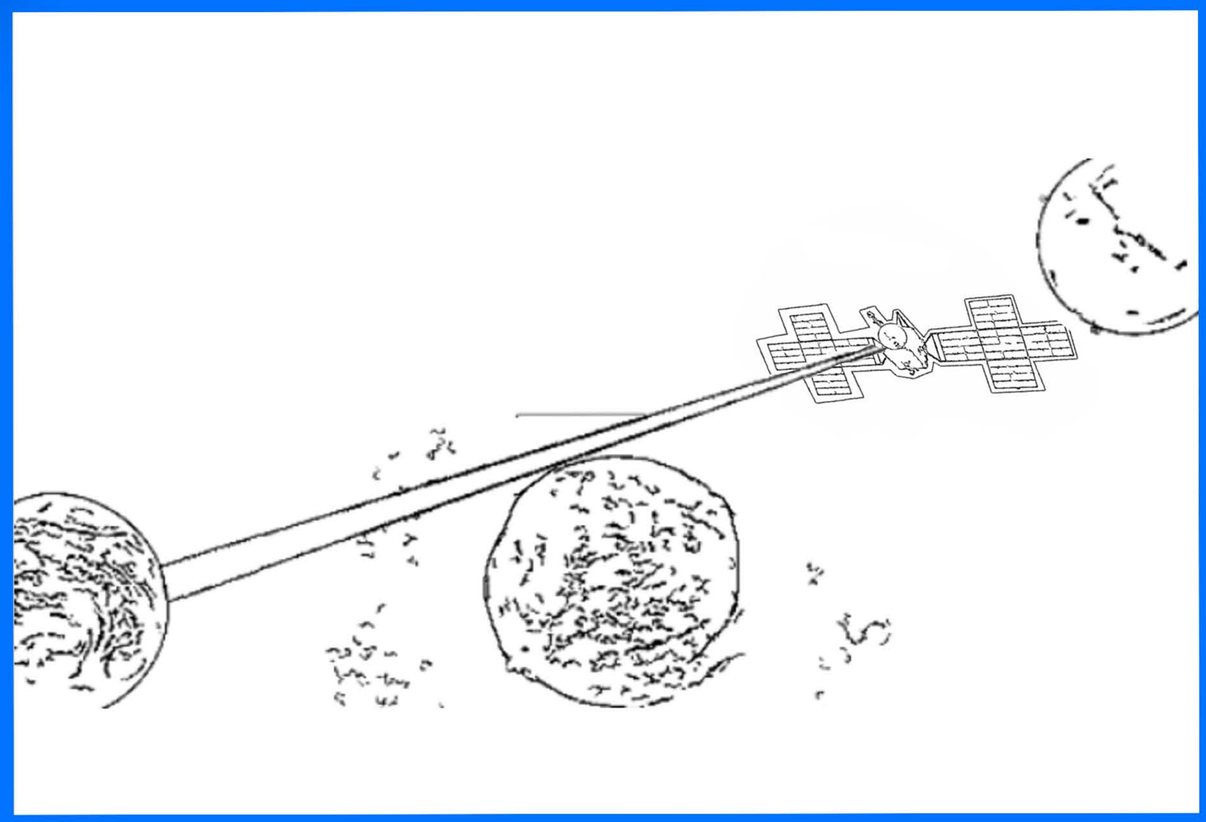

Psyche Spacecraft
Image Credt: Maxar

Planets and Psyche Image Credit: NASA

Write why you think it is helpful to be able to communicate more data between a spacecraft and the Earth.

https://gameon.nasa.gov/archived-projects-2/deep-space-optical-communications-dsoc/

LENGUITO, G. ET AL. 2019.

Figure 7. XFC development unit set-up inside the chamber

LENGUITO, G. ET AL. 2019.

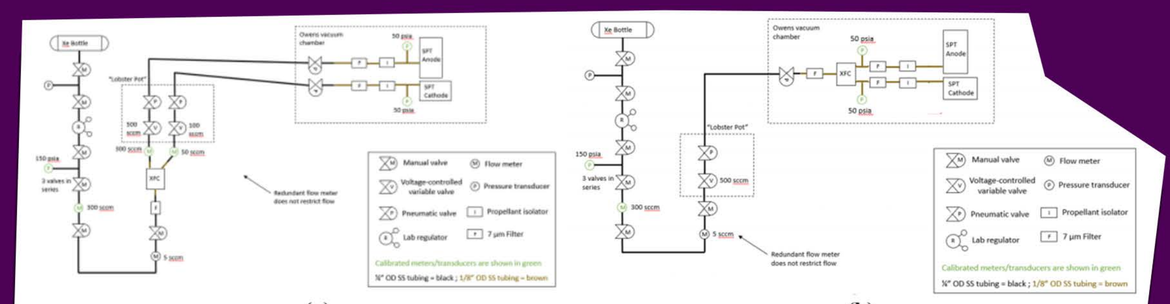

Figure 8. Integrated test set-up with the XFC placed: a) outside the chamber; b) inside the chamber.

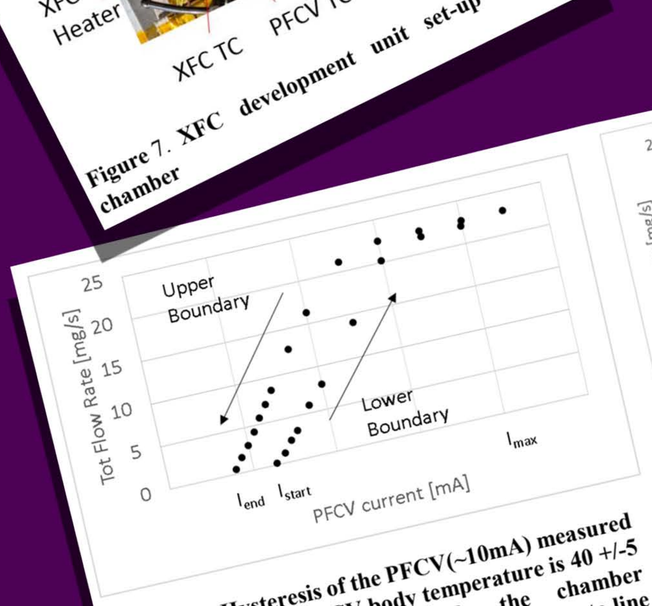

Figure 9. Hysteresis of the PFCV(~10mA) measured during cold flow; PFCV body temperature is 40 +/-5 C, with XFC place outside the chamber (configuration not more than 0.5ohm loss due to line resistance).

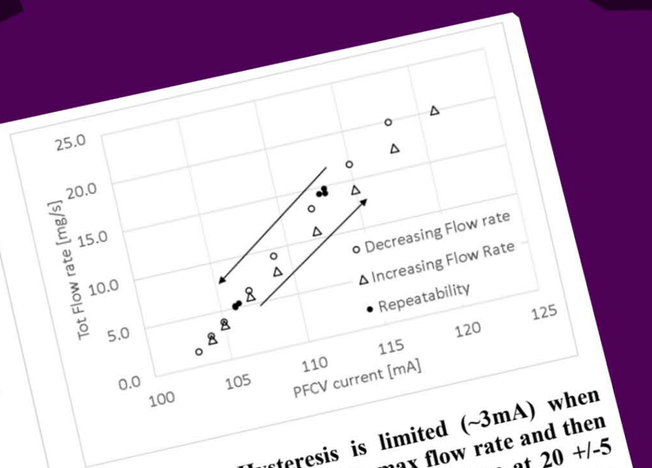

Figure 10. Hysteresis is limited (~3mA) when the PFCV current is set to max flow rate and then dialed down. PFCV body temperature at 20 +/-5 °C. XFC set up inside the vacuum chamber (Configuration #2).

LENGUITO, G. ET AL. 2019.

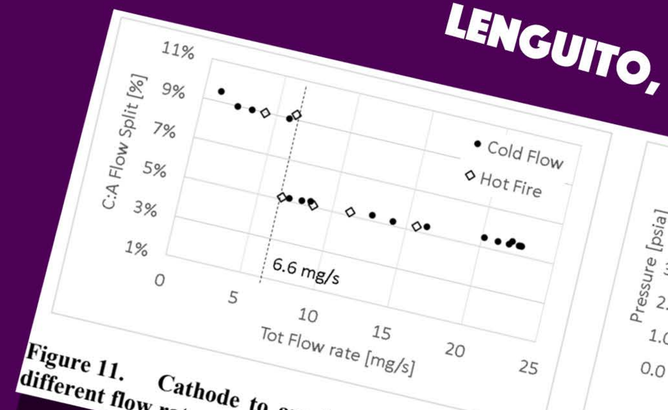

Figure 11. Cathode to anode flow split ration at different flow rates during cold flow and hot fire.

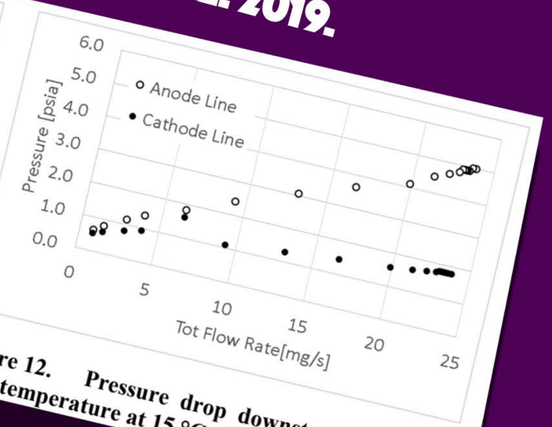

Figure 12. Pressure drop downstream the XFC. XFC temperature at 15 °C +/- 5 °C.

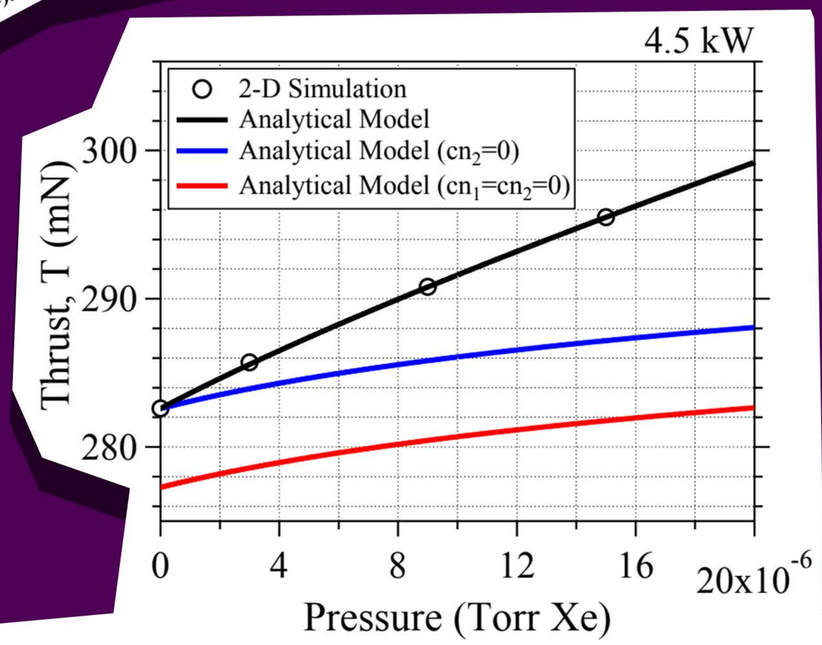

Fig 4. Comparison of the 2-D numerical simulation predictions with three different solutions of the analytical model for the thrust (Eq. (13)). For all three solutions α=1.

MIKELLIDES, I. ET AL. 2019.

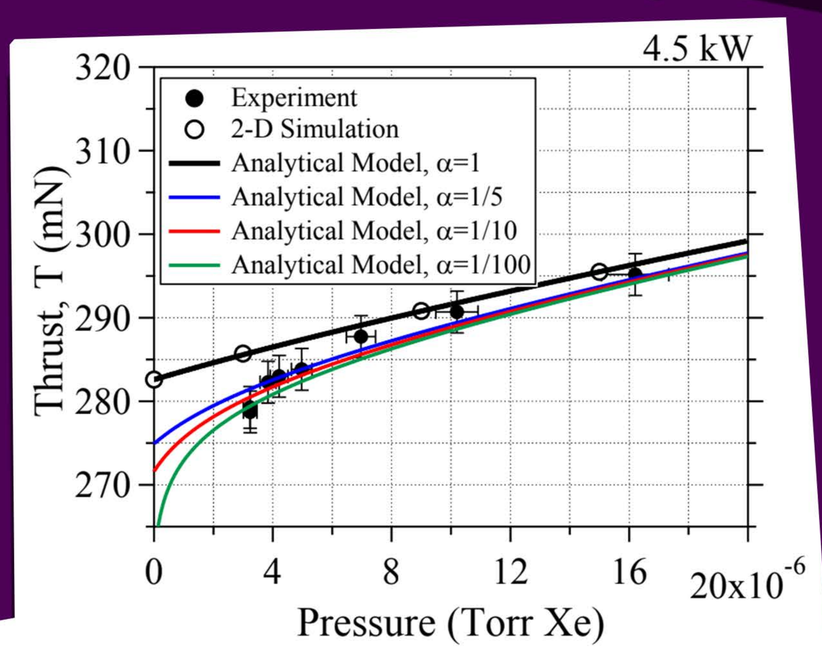

Fig 5. Comparison between Hall2De simulations, measurements and solutions of the analytical; thrust model (Eq. (13)) for different values of the coefficient α.

MIKELLIDES, I. ET AL. 2019.

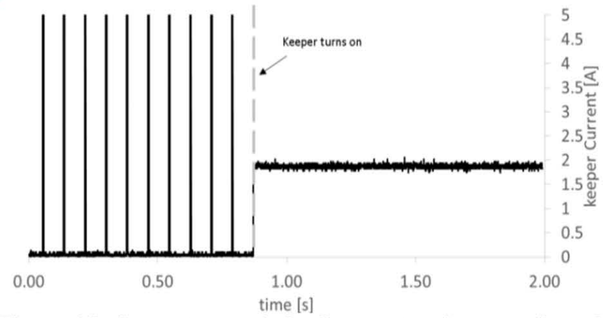

Figure 27. Scope trace of the keeper turning on when the discharge current 5.4A

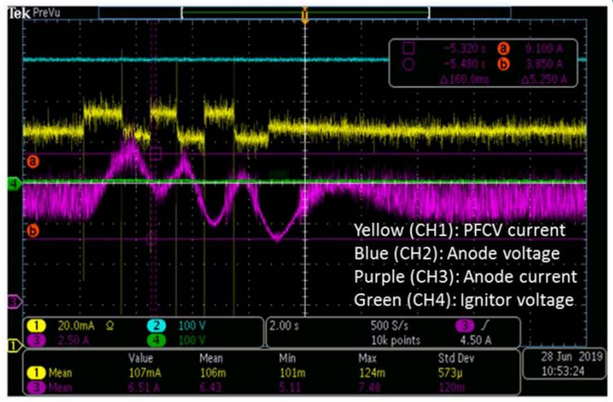

Figure 28. Thruster perturbation case and PFCV control loop response

MALONE, S. ET AL. 2019.

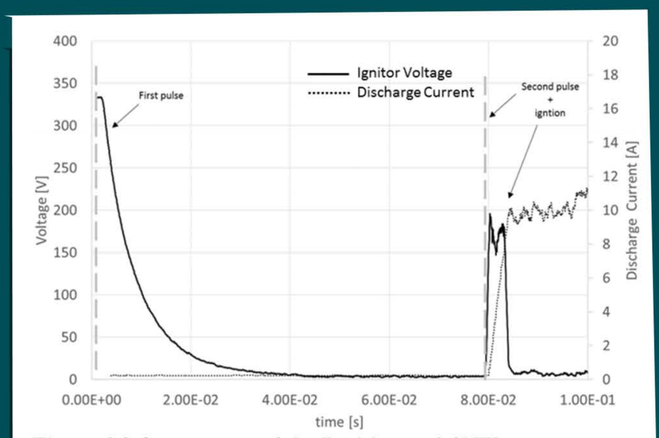

Figure 26. Scope trace of the Ignition at 3.0kW

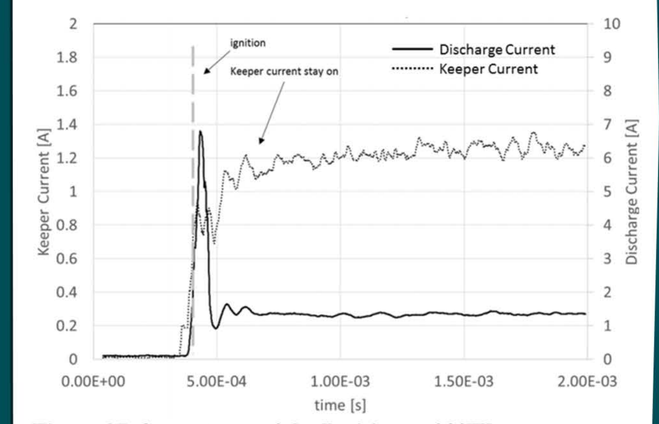

Figure 27. Scope trace of the Ignition at 900W

MALONE, S. ET AL. 2019.

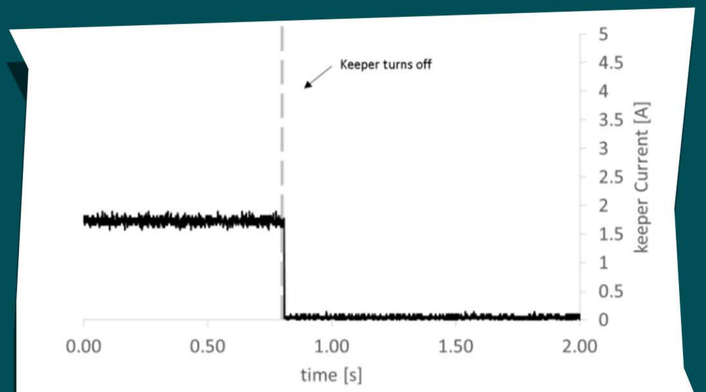

Figure 26. Scope trace of the keeper turning off when the discharge current is 6.2A

MALONE, S. ET AL. 2019.

LENGUITO, G. ET AL. 2019.

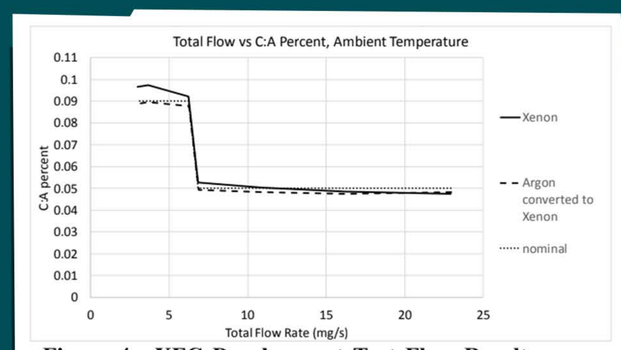

Figure 4. XFC Development Test Flow Results – Ambient Temperature

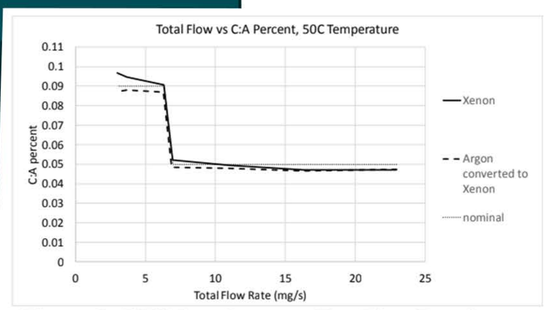

Figure 5. XFC Development Test Flow Results – Hot Temperature

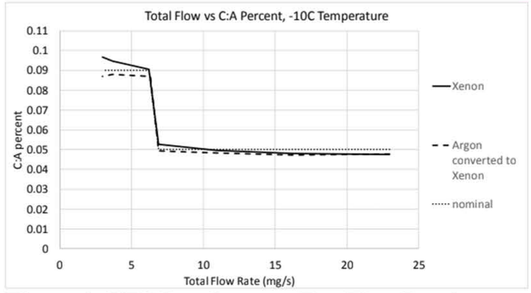

Figure 6. XFC Development Test Flow Results – Cold Temperature

LENGUITO, G. ET AL. 2019.

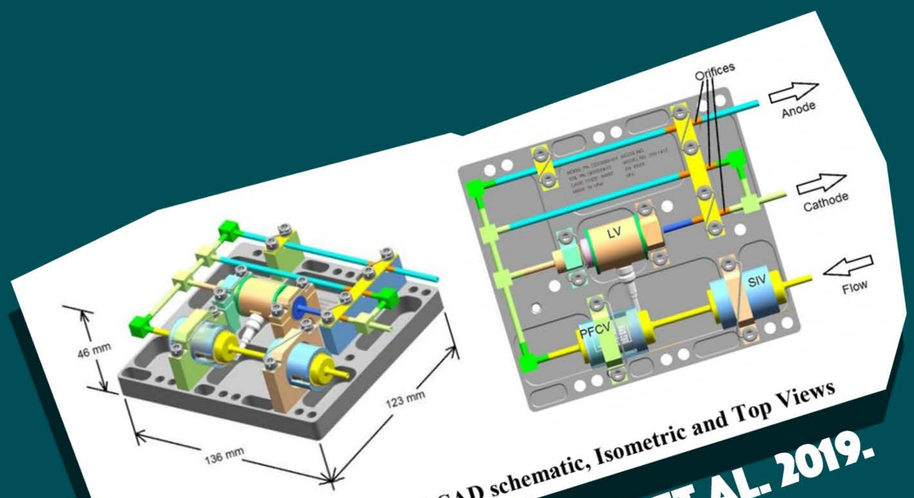

Figure 2. Moog XFC CAD schematic, Isometric and Top Views

LENGUITO, G. ET AL. 2019.

Figure 3. XFC Development Unit and XFC Development Unit with Thermocouples

LENGUITO, G. ET AL. 2019.

BPG 3

MALONE, S. ET AL. 2019.

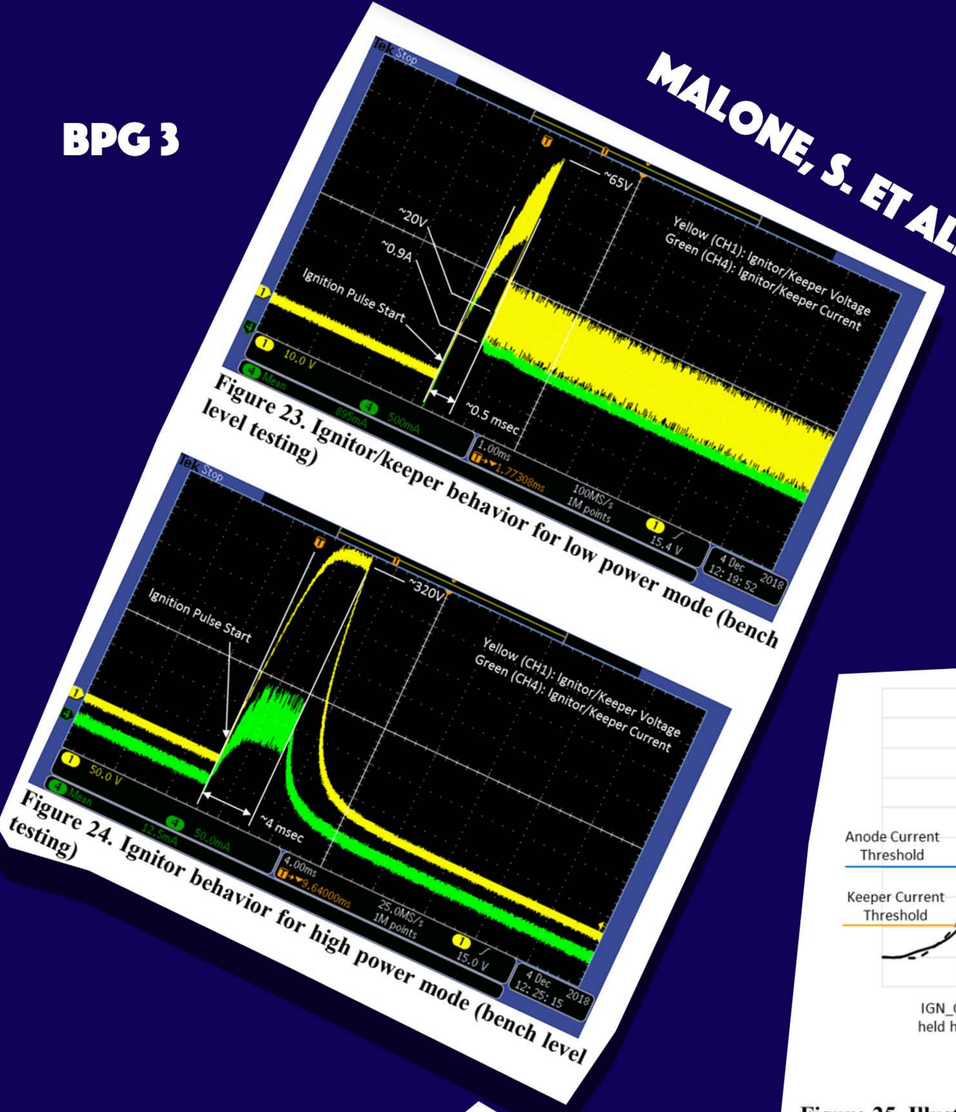

Figure 23. Ignitor/keeper behavior for low power mode (bench level testing)

Figure 24. Ignitor behavior for high power mode (bench level testing)

MALONE, S. ET AL. 2019.

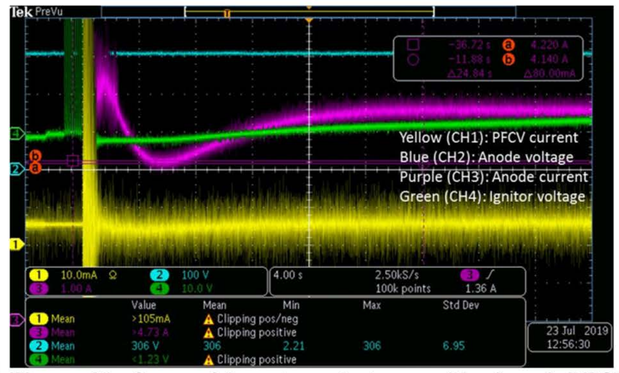

Figure 21. Successful system start up with slowed PFCV controller and no filter on PFCV output

Noise on PFCV controller still causes significant fluctuation in anode current but startup is successful

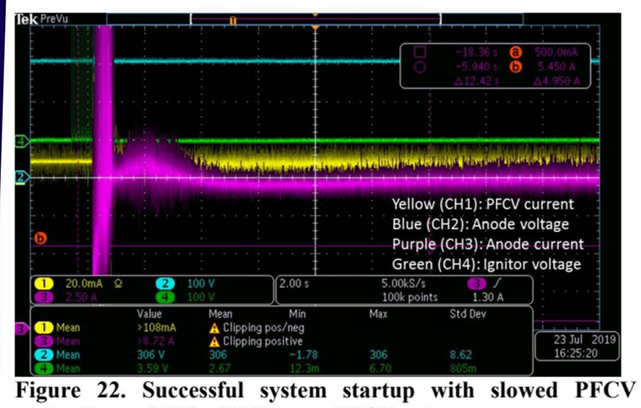

Figure 22. Successful system startup with slowed PFCV controller and 330 mH filter on PFCV output

Noise on PFCV controller is significantly reduced, resulting in much tighter and faster control of anode current during successful startup.

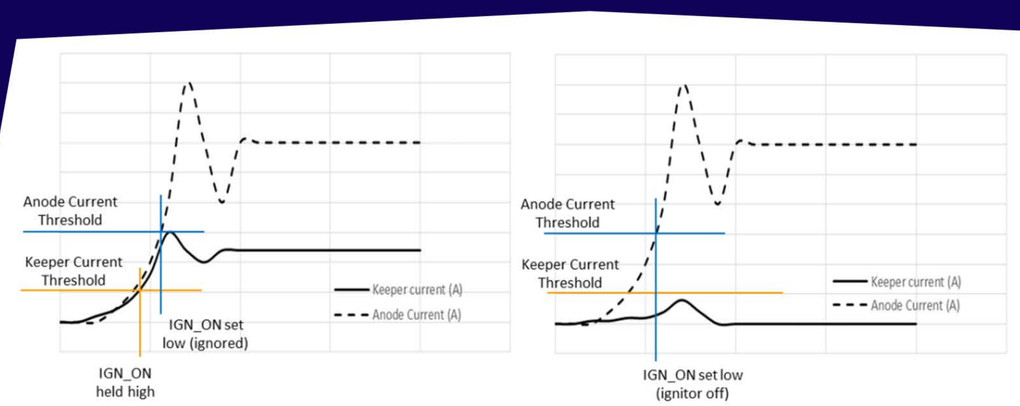

Figure 25. Illustration of anode/keeper current race condition showing successful (a) and failed (b) keeper operation

MALONE, S. ET AL. 2019.

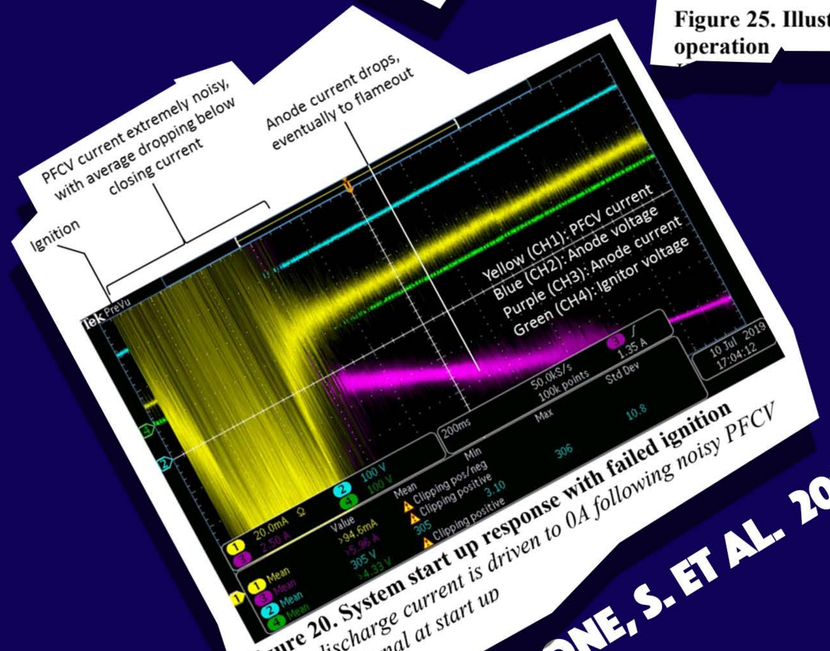

Figure 20. System start up response with failed ignition

Anode discharge current is driven to 0A following noisy PFCV controller signal at start up

MALONE, S. ET AL. 2019.

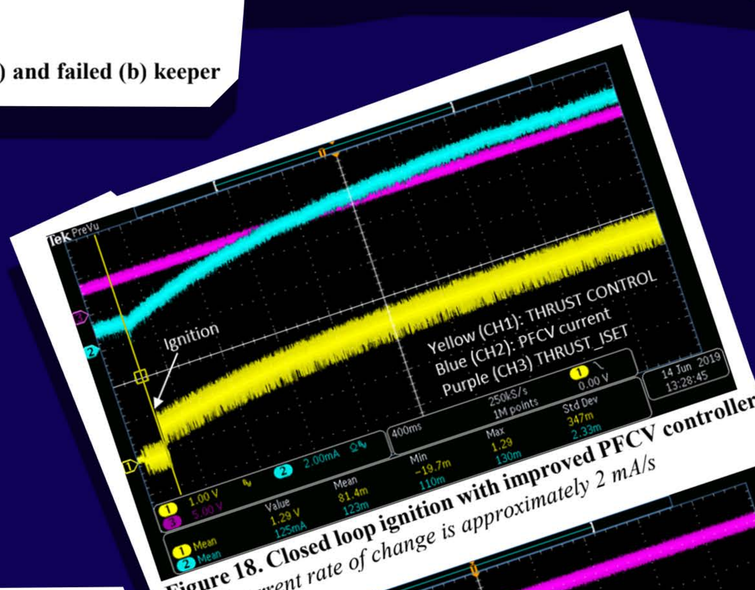

Figure 18. Closed loop ignition with improved PFCV controller

PFCV current rate of change is approximately 2 mA/s

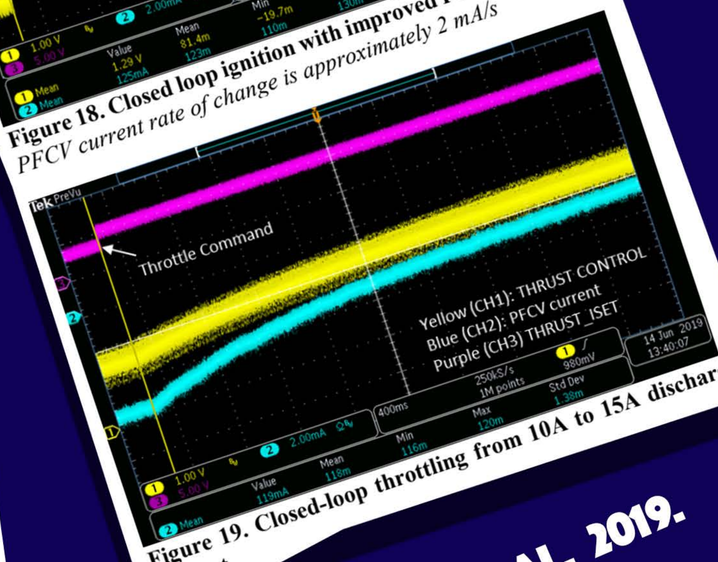

Figure 19. Closed-loop throttling from 10A to 15A discharge current

MALONE, S. ET AL. 2019.

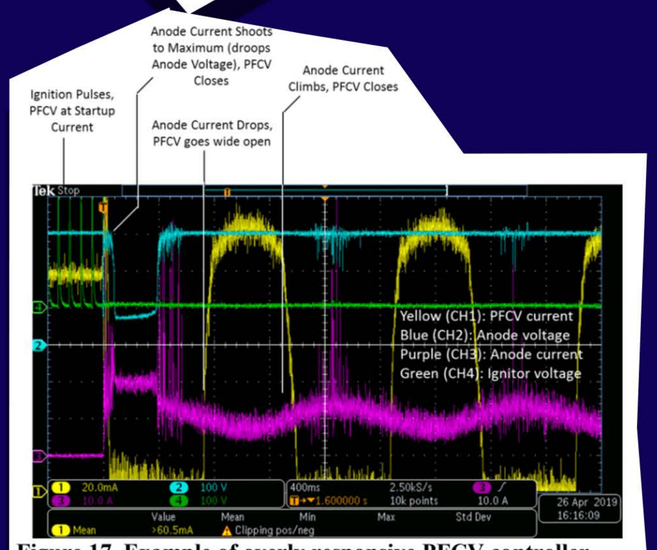

Figure 17. Example of overly responsive PFCV controller

The high gain of the PFCV control loop causes PFCV current to switch rapidly between 140 mA and 0 mA as the anode current transitions above or below its setpoint of 10A.

MALONE, S. ET AL. 2019.

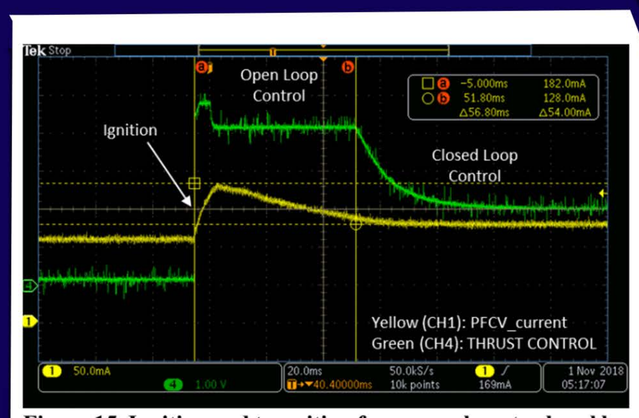

Figure 15. Ignition and transition from open loop to closed loop

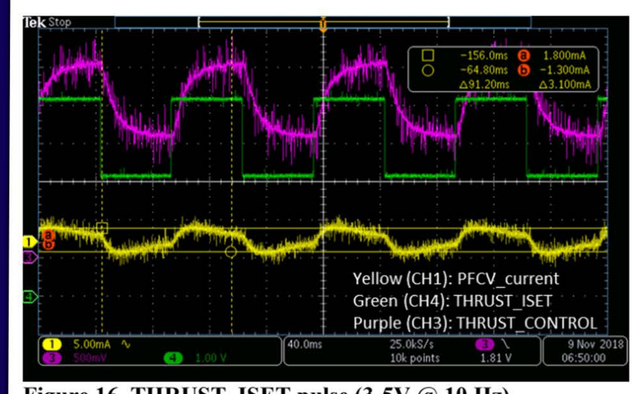

Figure 16. THRUST_ISET pulse (3-5V @ 10 Hz)

MALONE, S. ET AL. 2019.

BPG 4

Figure 13. CAFC tray test feedback circuit

MALONE, S. ET AL. 2019.

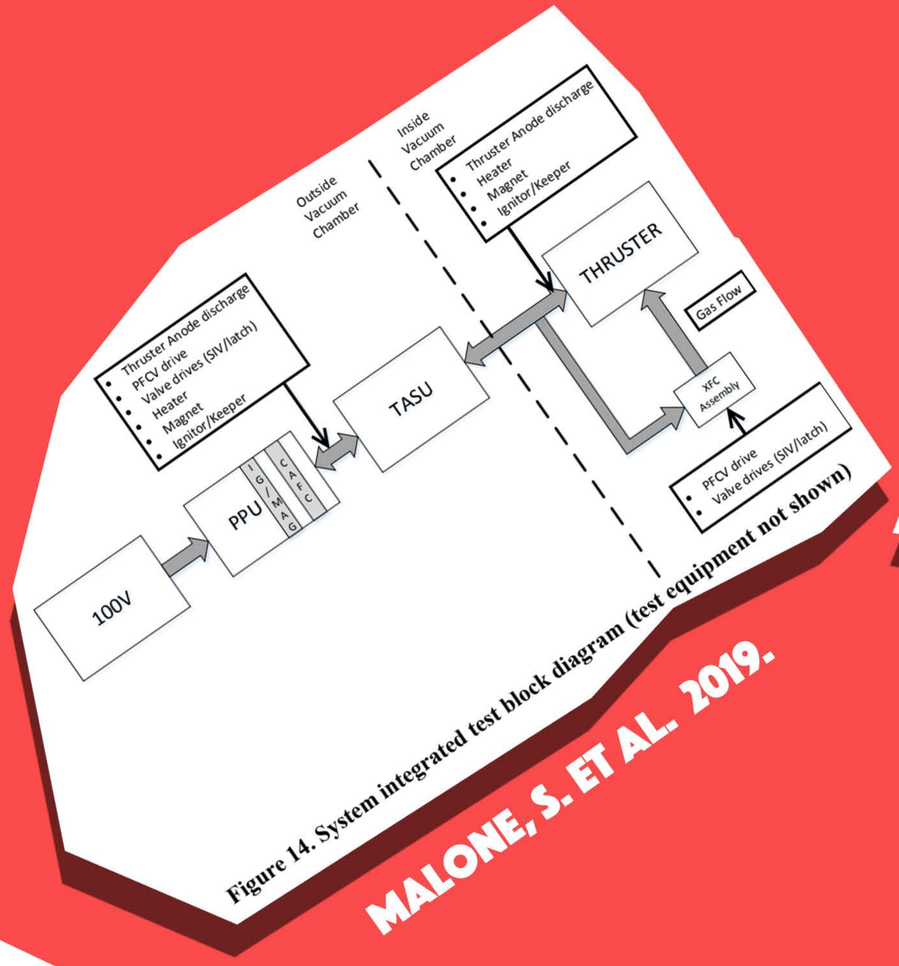

Figure 14. System integrated test block diagram (test equipment not shown)

MALONE, S. ET AL. 2019.

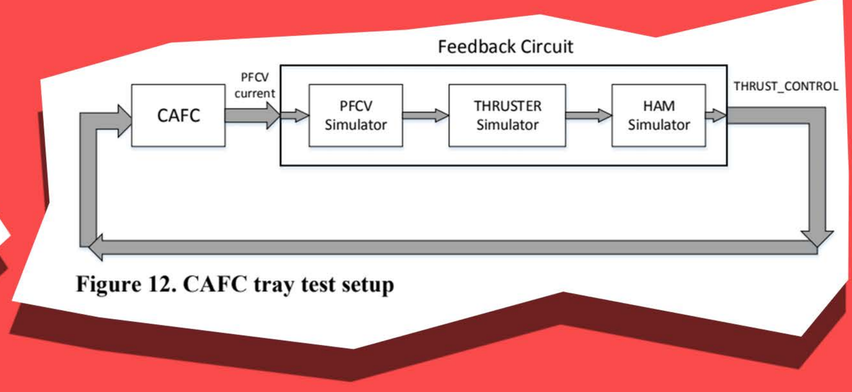

Figure 12. CAFC tray test setup

MALONE, S. ET AL. 2019.

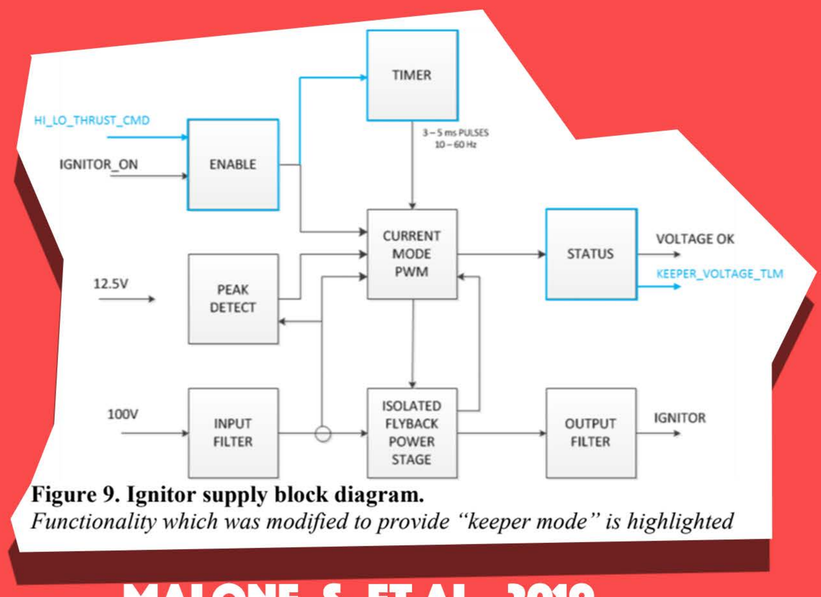

Figure 9. Ignitor supply block diagram.
Functionality which was modified to provide "keeper mode" is highlighted

MALONE, S. ET AL. 2019.

MALONE, S. ET AL. 2019.

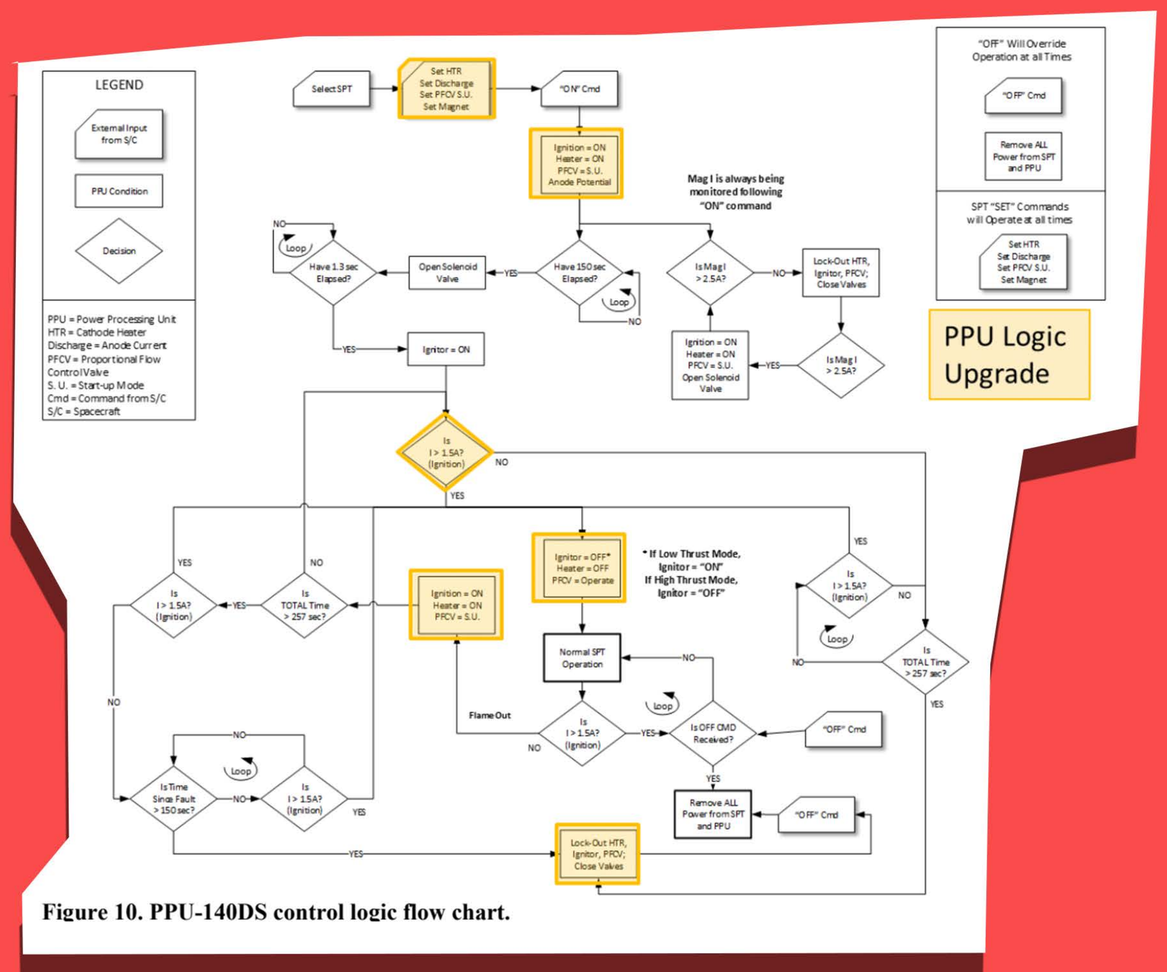

Figure 10. PPU-140DS control logic flow chart.

MALONE, S. ET AL. 2019.

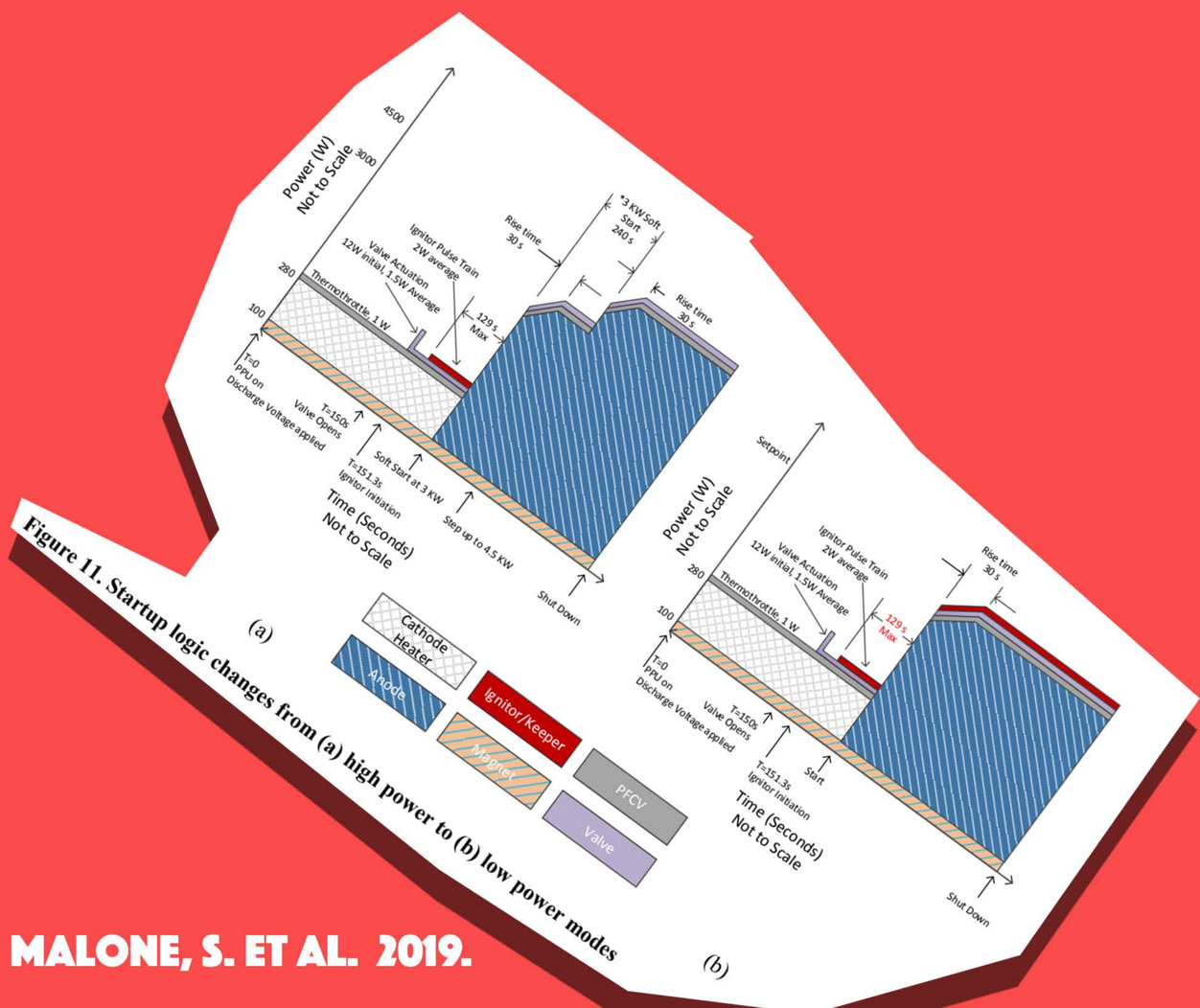

Figure 11. Startup logic changes from (a) high power to (b) low power modes

MALONE, S. ET AL. 2019.

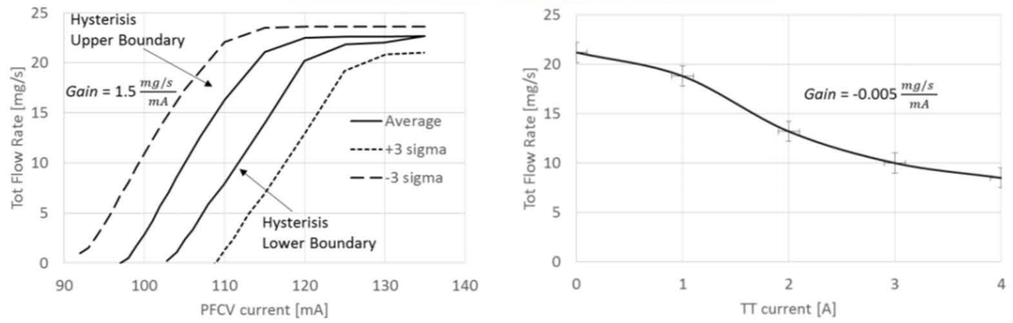

(a) (b)

Figure 6. Comparison of PFCV (a) and Thermothrottle (b) Flow Rate vs. Current at 40 psia
PFCV is nearly 300x more responsive to current than the thermothrottle. Note also that thermothrottle has a limited flow control range of about 2:1

MALONE, S. ET AL. 2019.

Ignition Pulse	Typical	Minimum	Maximum
Pulse Repetition Rate	10 Hz	9 Hz	20 Hz
Pulse Width	4 msec	3 msec	5 msec
@ 3kOhm Load	320V	290V	350V
With Open Load			370V

Sustaining Pulse	Typical	Minimum	Maximum
Pulse Repetition Rate	10 Hz	9 Hz	20 Hz
Pulse Width	4 msec	3 msec	5 msec
@ 5.26 Ohm Load	5A	4A	8A
With Open Load			14A

Ignition Pulse	Typical	Minimum	Maximum
Pulse Repetition Rate	10 Hz	9 Hz	20 Hz
Pulse Width	4 msec	3 msec	5 msec
@ 3kOhm Load	320V	290V	350V
With Open Load			370V

Keeper Mode	Typical	Minimum	Maximum
@ 17.4 Ohm Load	1.2A	1A	1.5A
With Open Load			14A

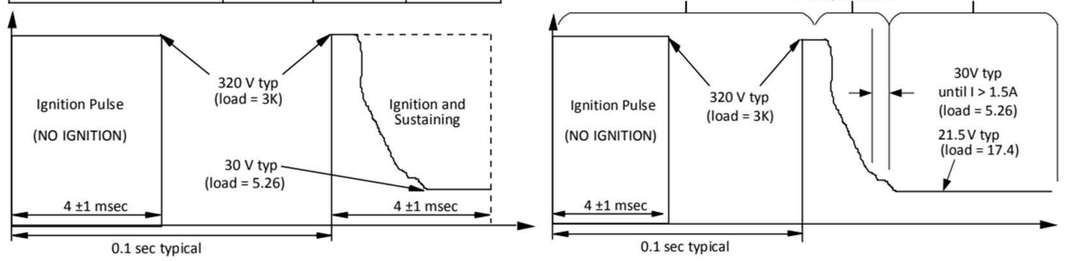

(a) (b)

Figure 8. Ignitor/Keeper performance requirements for (a) high power and (b) low power mode
In low power mode, the ignitor supply post-ignition sustaining pulse transitions to "keeper mode" to provide continuous power to the cathode.

MALONE, S. ET AL. 2019.

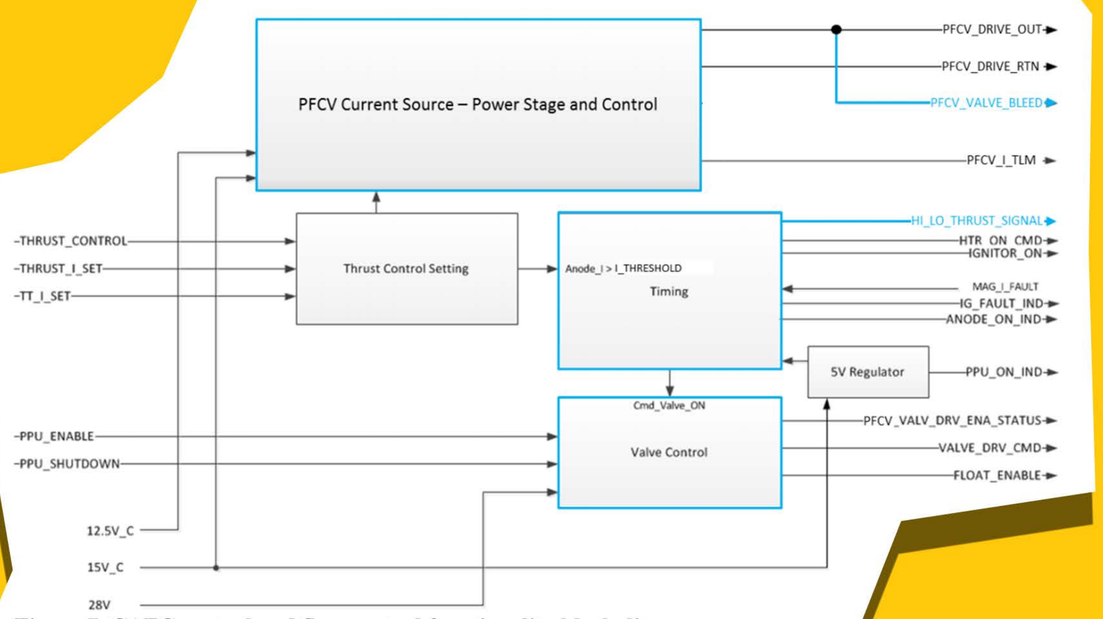

Figure 7. CAFC control and flow control functionality block diagram
Updated blocks are highlighted, along with new or significantly changed signals

MALONE, S. ET AL. 2019.

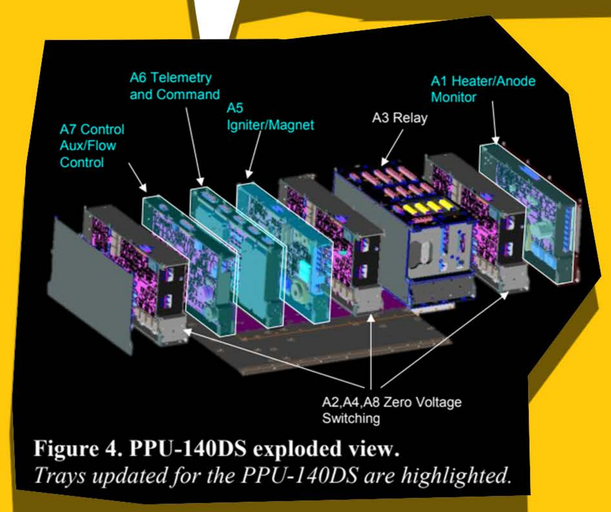

Figure 4. PPU-140DS exploded view.
Trays updated for the PPU-140DS are highlighted.

MALONE, S. ET AL. 2019.

Figure 5. Block diagram of PPU-140DS
PFCV control and Keeper mode are new features relative to the heritage PPU-140.

MALONE, S. ET AL. 2019.

Figure 2. Functional Block Diagram of the ZVS Anode Converter

MALONE, S. ET AL. 2019.

Figure 3. PPU-140. Tray locations shown.

MALONE, S. ET AL. 2019.

BPG 6

ORTEGA, A. ET AL. 2019.

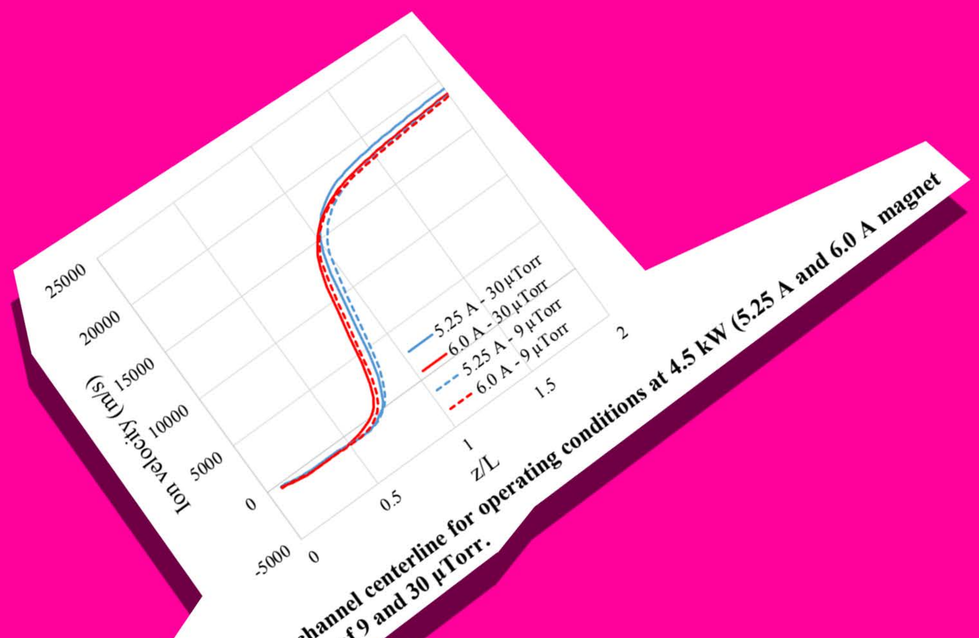

Fig. 10. Ion velocity along the channel centerline for operating conditions at 4.5 kW (5.25 A and 6.0 A magnet current) at background pressure of 9 and 30 µTorr.

ORTEGA, A. ET AL. 2019.

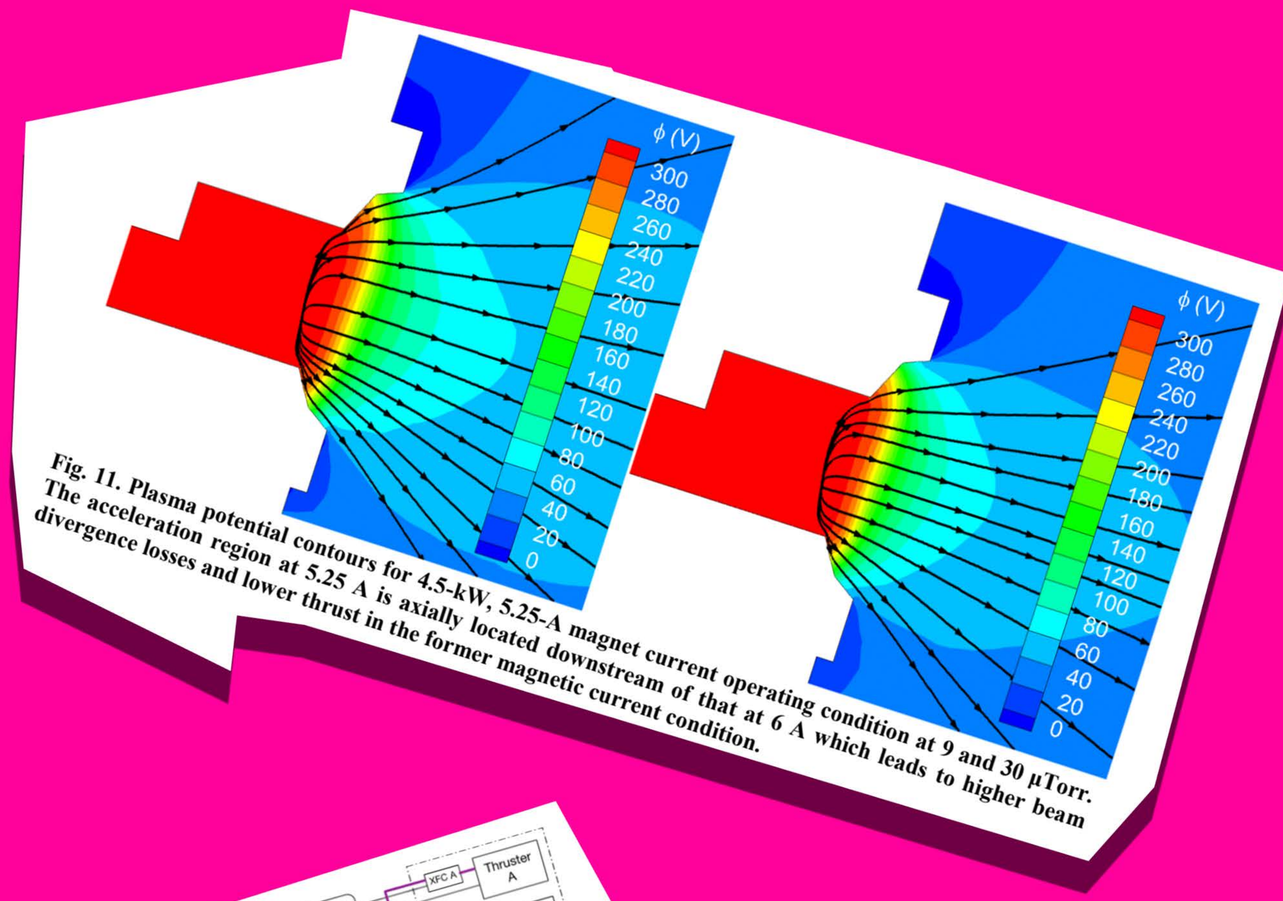

Fig. 11. Plasma potential contours for 4.5-kW, 5.25-A magnet current operating condition at 9 and 30 µTorr. The acceleration region at 5.25 A is axially located downstream of that at 6 A which leads to higher beam divergence losses and lower thrust in the former magnetic current condition.

MALONE, S. ET AL. 2019.

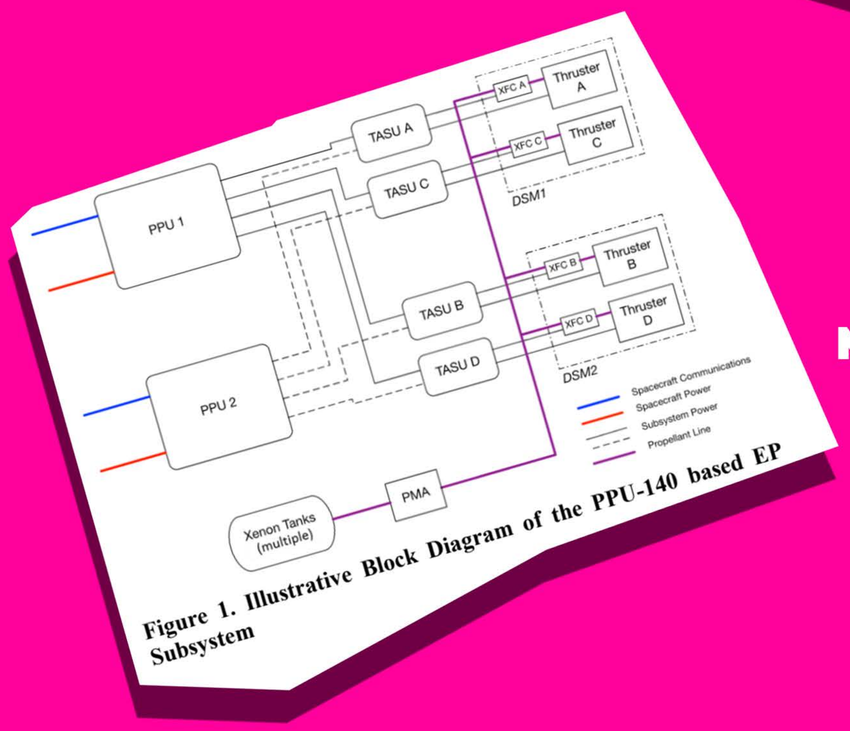

Figure 1. Illustrative Block Diagram of the PPU-140 based EP Subsystem

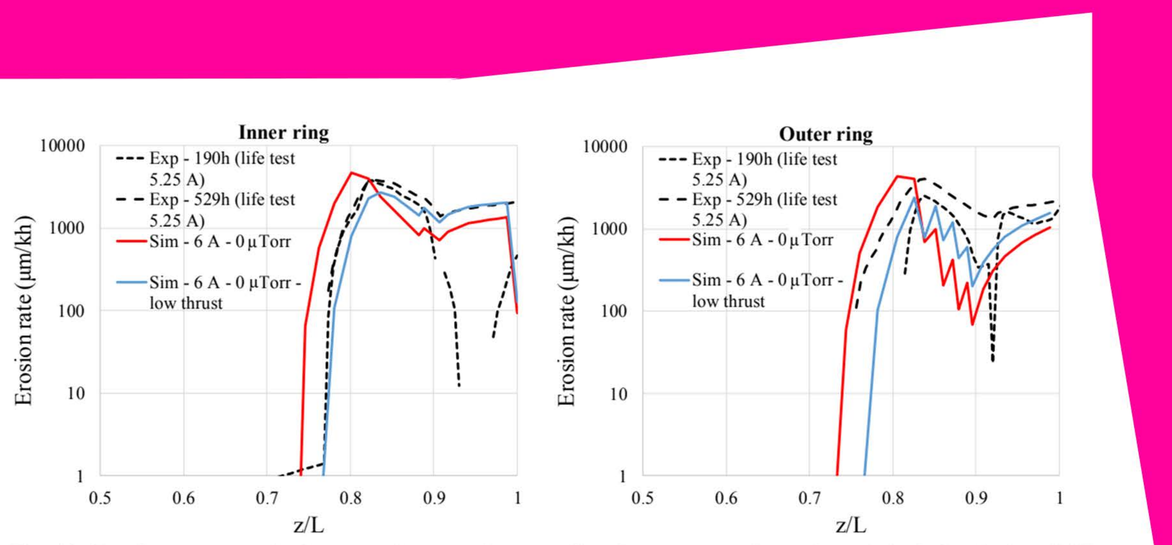

Fig. 13. Erosion rates at the inner and outer rings predicted at vacuum from the original simulation (LIF-

ORTEGA, A. ET AL. 2019.

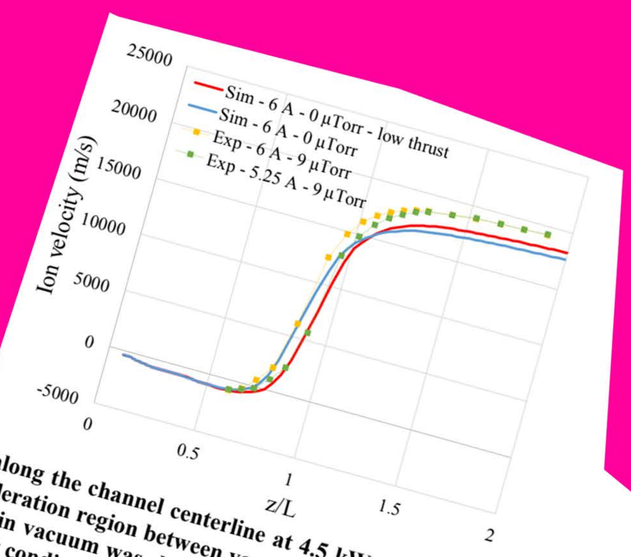

Fig. 12. Ion velocity profile along the channel centerline at 4.5 kW, 6 A magnet current from the simulation without axial shift in the acceleration region between vacuum and 9 µTorr and the "low thrust" simulation in which the acceleration region in vacuum was shifted downstream. The LIF measurements at 9 µTorr for the 5.25-A and 6-A magnet current conditions are also included for reference.

ORTEGA, A. ET AL. 2019.

BPG 7

ORTEGA, A. ET AL. 2019.

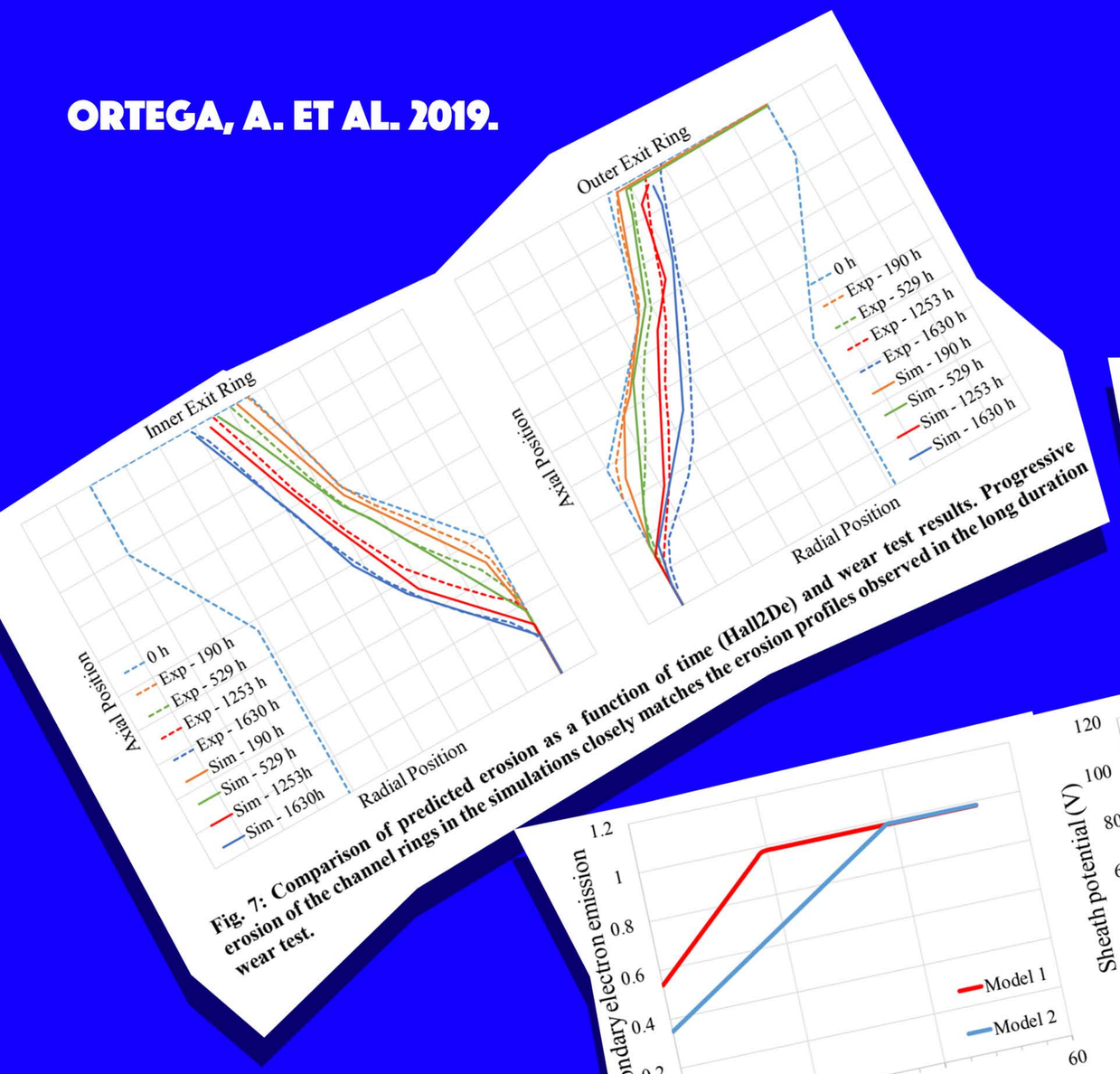

Fig. 7: Comparison of predicted erosion as a function of time (Hall2De) and wear test results. Progressive erosion of the channel rings in the simulations closely matches the erosion profiles observed in the long duration wear test.

ORTEGA, A. ET AL. 2019.

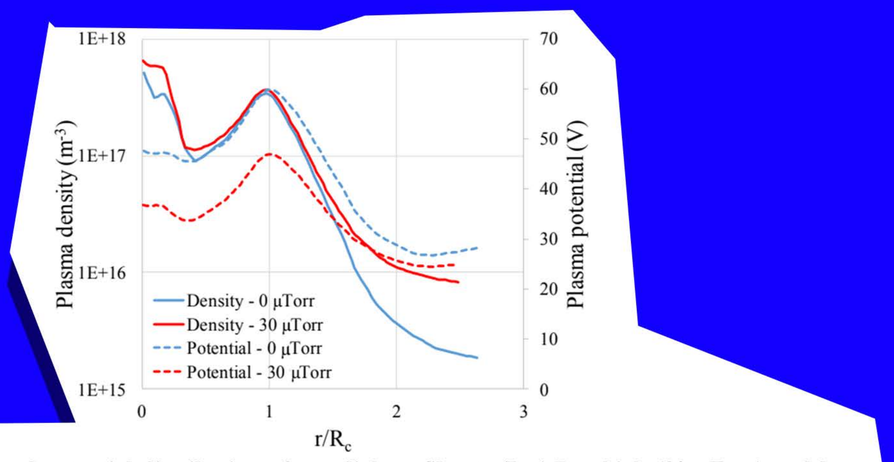

Fig. 9: Plasma density and potential distribution of a radial profile at z/L=1.7 at high (30 μTorr) and low (vacuum) background pressures. R_c is the distance between the centerline of the acceleration channel and the thruster centerline.

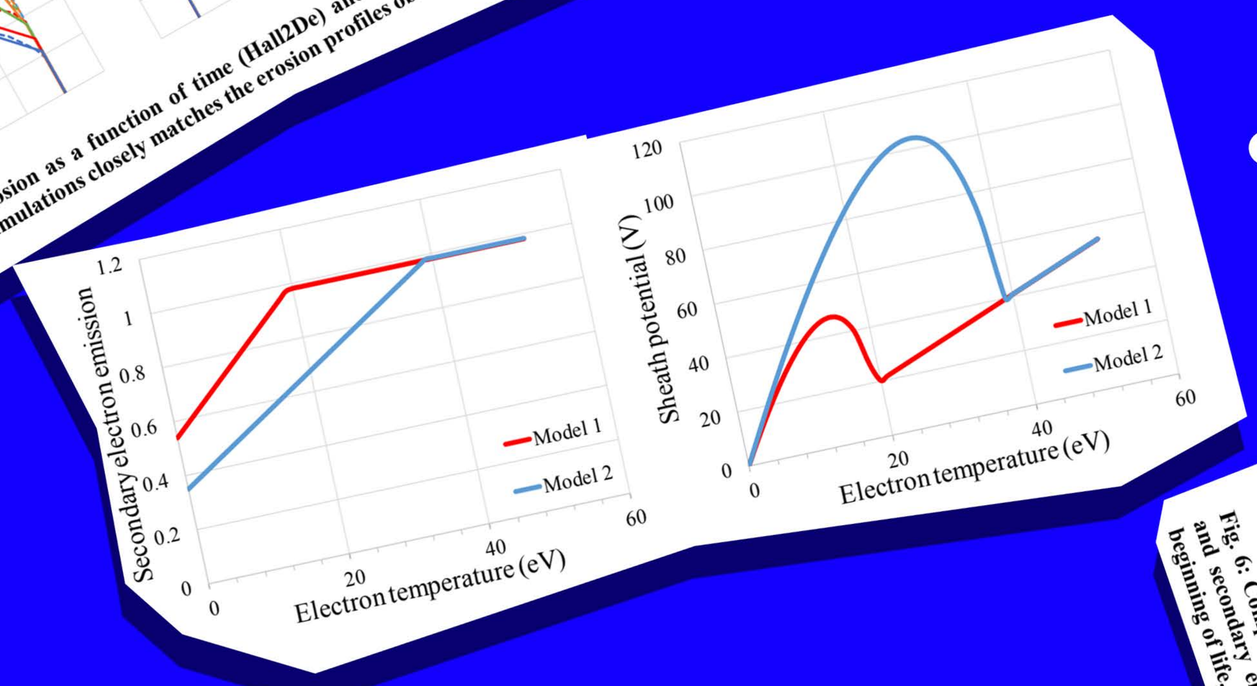

ORTEGA, A. ET AL. 2019.

ORTEGA, A. ET AL. 2019.

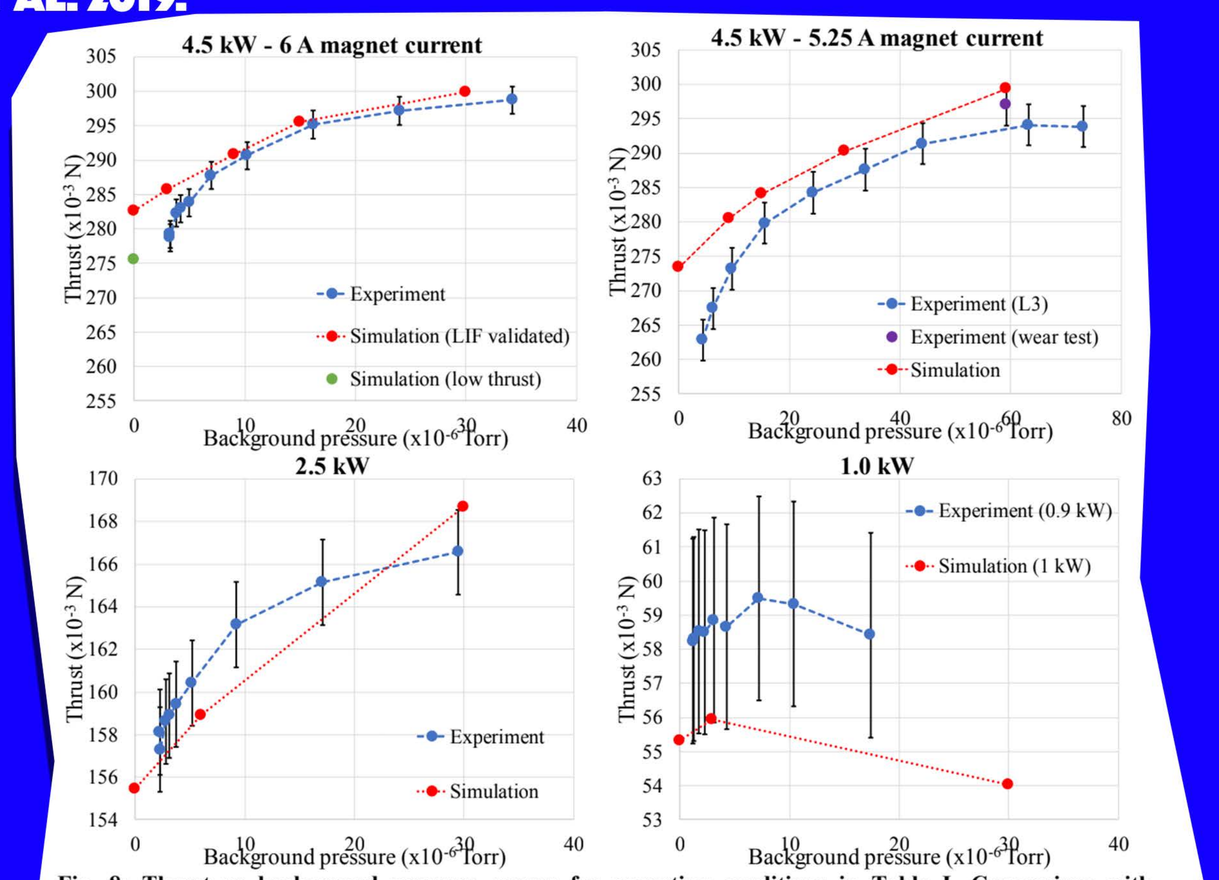

Fig. 8: Thrust vs background pressure curves for operating conditions in Table I. Comparison with experimental measurements from [1]

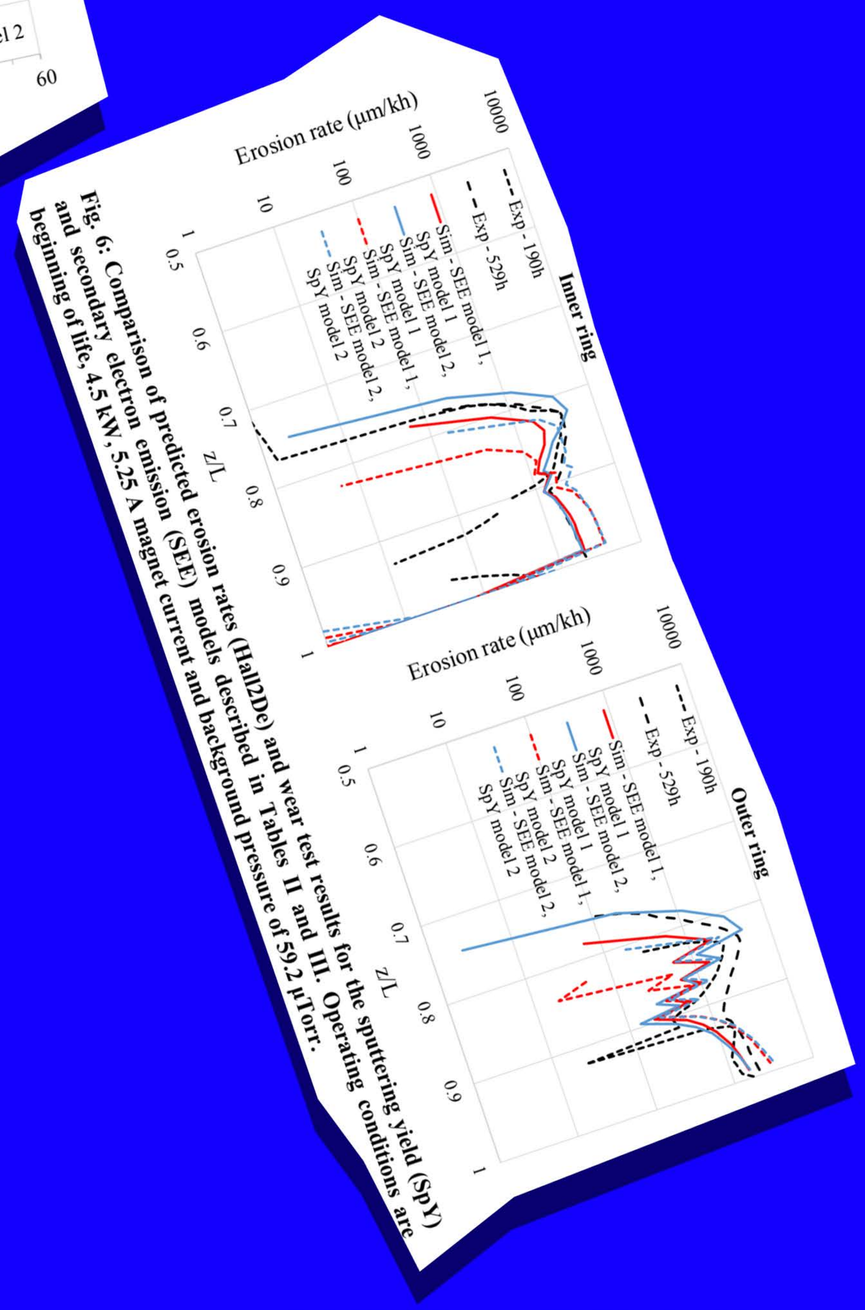

Fig. 6: Comparison of predicted erosion rates (Hall2De) and wear test results for the sputtering yield (SpY) and secondary electron emission (SEE) models described in Tables II and III. Operating conditions are beginning of life, 4.5 kW, 5.25 A magnet current and background pressure of 59.2 μTorr.

ORTEGA, A. ET AL. 2019.

BPG 8

ORTEGA, A. ET AL. 2019.

Table II. Coefficients in Bohdansky equation for sputtering yield models 1 and 2

Model	A (mm^3/C)	E_T (eV)
1	0.015	25
2	0.035	35

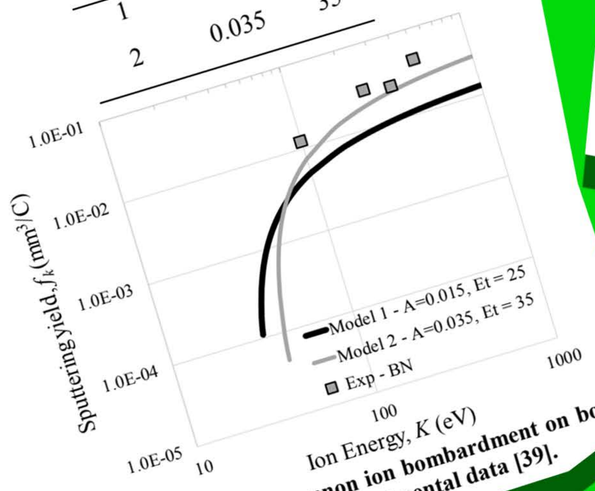

Fig. 4. Left: Sputtering yield for perpendicular xenon ion bombardment on boron nitride (BN). Comparison between Models 1 and 2 (Eq. (1) and Table II) and experimental data [39].

ORTEGA, A. ET AL. 2019.

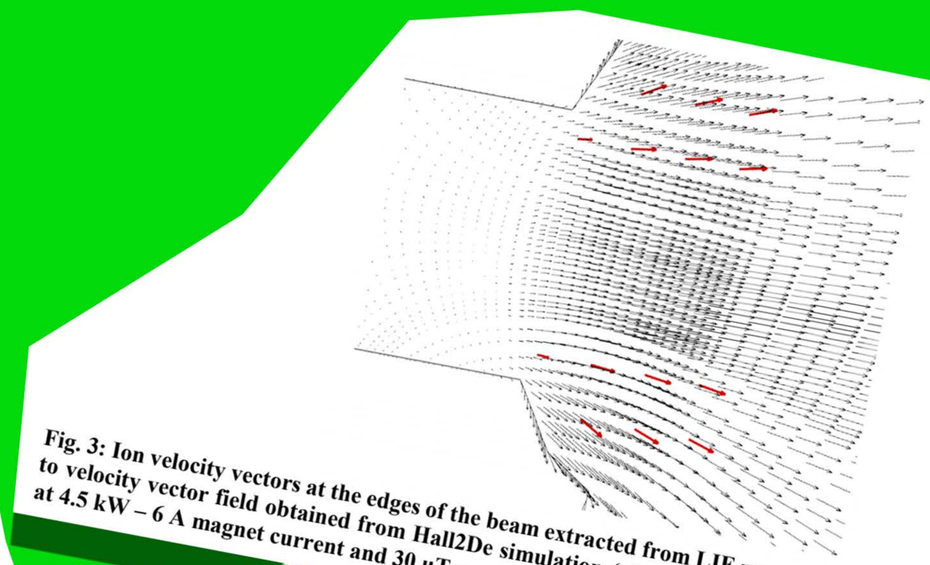

Fig. 3: Ion velocity vectors at the edges of the beam extracted from LIF measurements (red) and superimposed to velocity vector field obtained from Hall2De simulation (plotted at each computational cell) of the SPT-140 at 4.5 kW – 6 A magnet current and 30 µTorr.

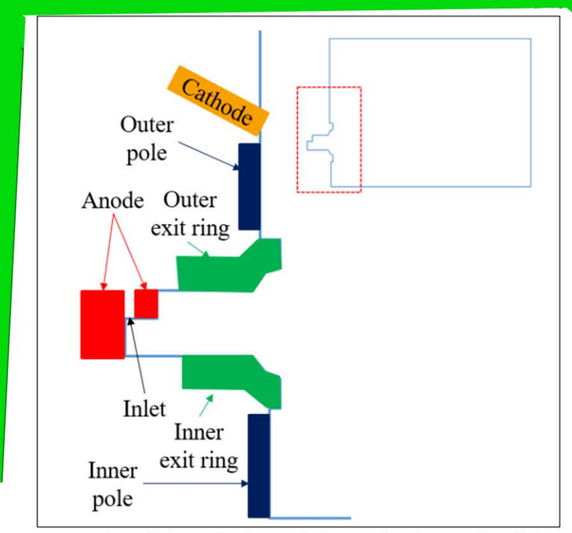

Fig. 1: Hall2De computational domain (top-right) and schematic of the thruster geometry

ORTEGA, A. ET AL. 2019.

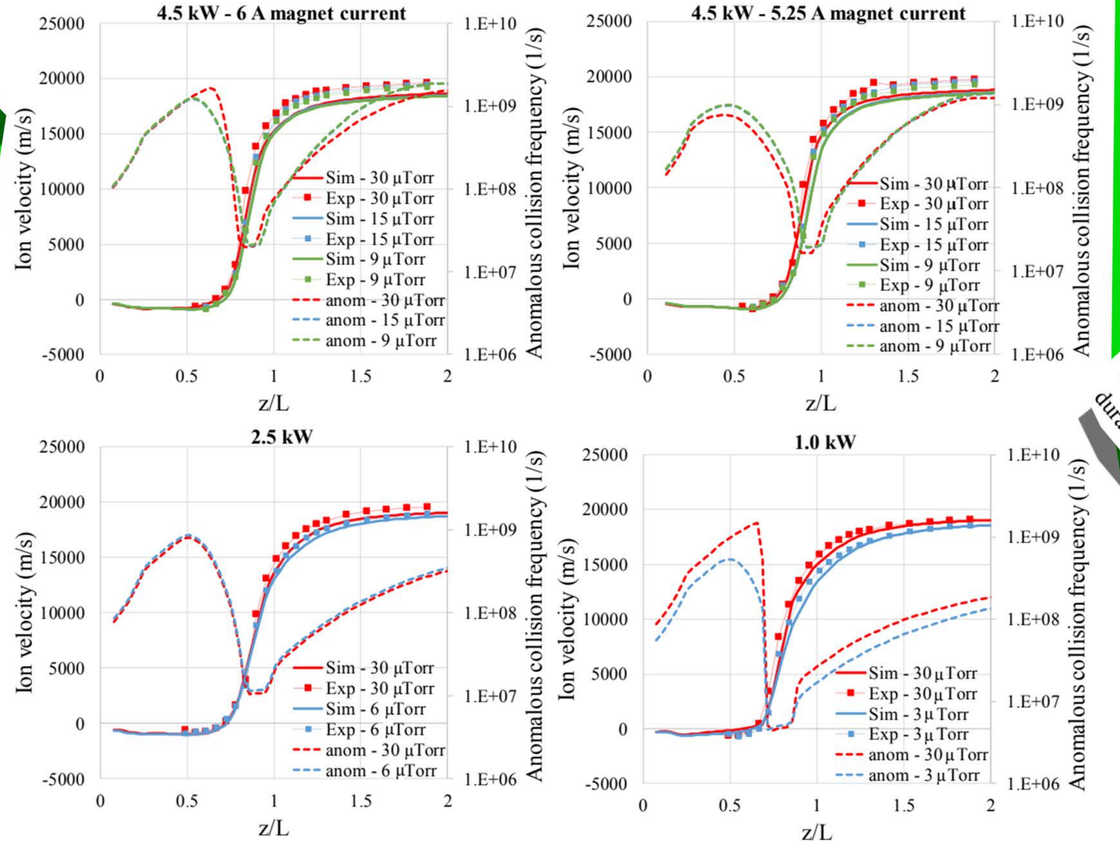

Fig. 2: Comparison between ion velocity at the channel centerline from simulations and LIF measurements for all operating conditions and background pressures for which LIF measurements were available. Anomalous collision frequency distribution employed is predicted in the simulation in dashed lines.

ORTEGA, A. ET AL. 2019.

Table I. Input parameters for SPT-140 simulations

Discharge power (kW)	Magnet current (A)	Discharge voltage (V)	Anode mass flow rate (mg/s) (Background pressure (µTorr))	Electron temperature at cathode exit (eV)	Plasma potential at cathode exit (V)	Cathode flow rate (% of anode flow rate)
4.5	6.0	300	14.97 (30)	4.0	20.4	5
4.5	5.25	300	15.00 (15)	4.0	17.0	5
2.5	4.0	300	14.95 (9)	4.0	19.9	5
2.5	4.0	300	14.95 (0)	4.0	26.0	9
2.75	4.0	300	*14.5 (59.2)	4.0		
1.0	4.0	300	14.58 (30)	4.0		
1.0	4.0	300	14.50 (15)	4.0		
1.0	4.0	300	14.48 (9)	4.0		
1.0	4.0	300	14.48 (0)	4.0		
1.0	4.0	300	9.1 (30)	4.0		
1.0	4.0	300	9.1 (15)	4.0		
1.0	4.0	300	9.1 (9)	4.0		
1.0	4.0	300	9.1 (6)	4.0		
1.0	4.0	300	9.1 (0)	4.0		
1.0	4.0	300	3.9 (30)	4.27 (2.9)		
1.0	4.0	300	4.27 (0)	4.0		

*Conditions of long duration life test. No LIF measurement at this background pressure. Mass flow rate from long duration life test data

ORTEGA, A. ET AL. 2019.

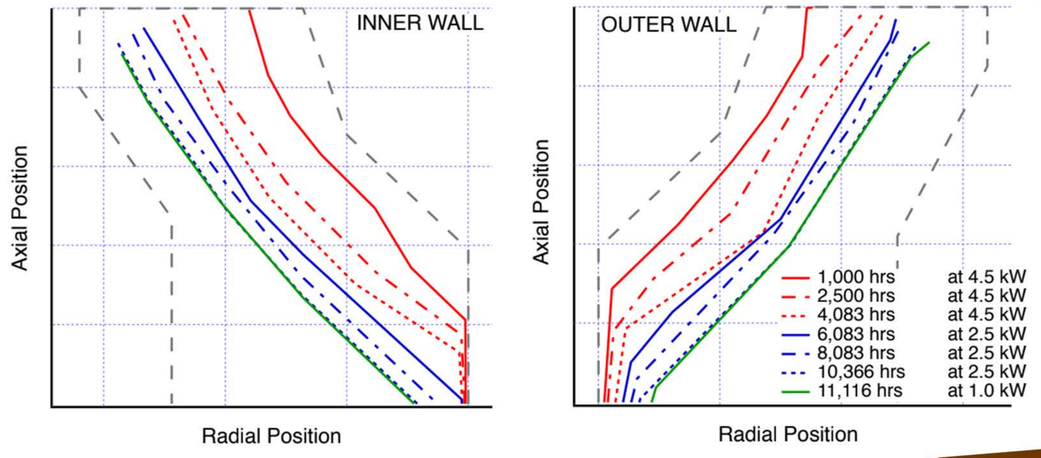

Fig. 16. Thruster Erosion Simulations for Representative Mission Profile.

SNYDER, J. S. ET AL. 2019.

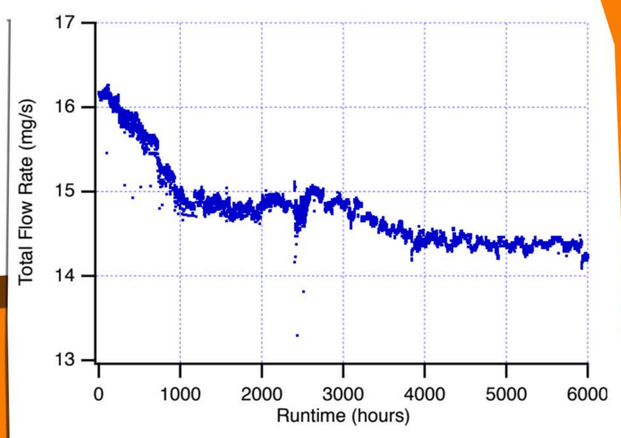

Fig. 13. Measured Total Flow Rate at 4.5 kW Thruster Discharge Power.

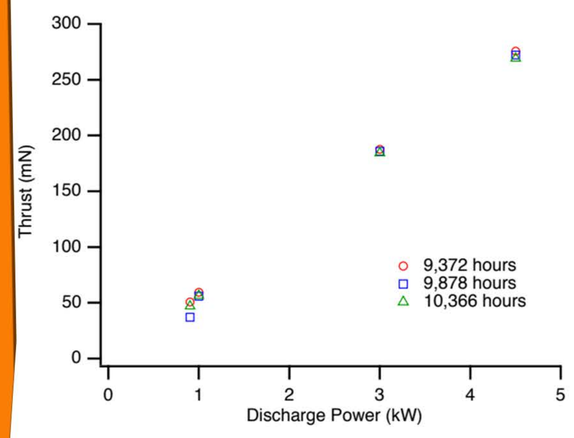

Fig. 14. Measured Thrust During Life Test Extension.

SNYDER, J. S. ET AL. 2019.

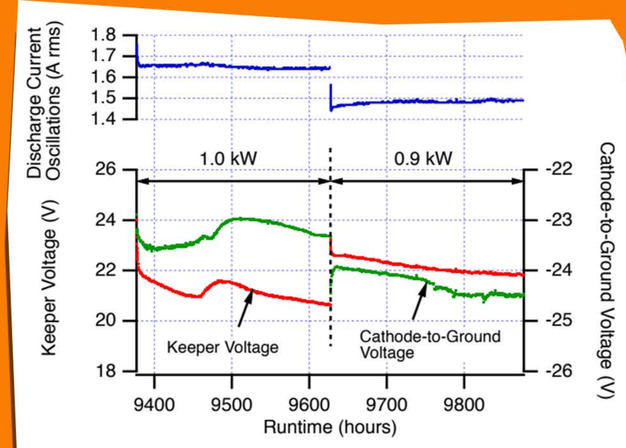

Fig. 15. Cathode Performance Indicators During Life Test Extension.

SNYDER, J. S. ET AL. 2019.

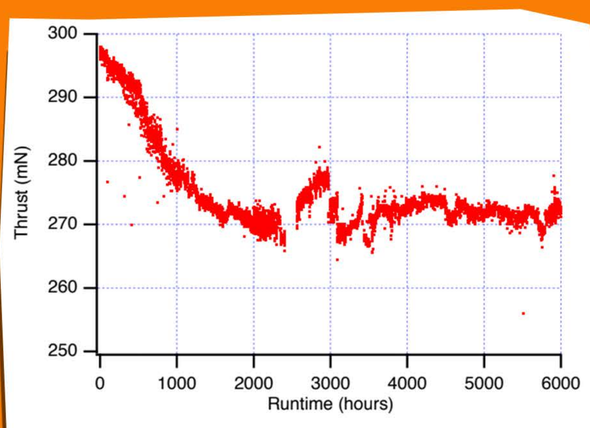

Fig. 12. Measured Thrust at 4.5 kW Thruster Discharge Power.

SNYDER, J. S. ET AL. 2019.

Table 4. Mission Total Impulse Requirements.

Mission Phase / Propellant Allocation	Impulse Required MN-sec
Deterministic Cruise Through Capture to Orbit A	14.5*
Cruise Momentum Management	0.1†
Asteroid Proximity Operations	0.3*
Spacecraft Initial Checkout/Commissioning	0.3†
Margin – Missed Thrust	0.6†
Margin – Thruster Performance Uncertainties	0.7†
Mission Total	**16.5**

** for baseline mission design at Project PDR.*
† assumes all operation at 4.5 kW.

SNYDER, J. S. ET AL. 2019.

Table 3. Measured Thrust at 0.9 kW Discharge Power for Several SPT-140 Thrusters and Test Conditions.

Thruster	Thruster Age, hours	Facility Background Pressure, µTorr (Xe)	Measured Thrust, mN
QM002	~790	~1	57 ± 2
QM001	~9,400	~10	58 ± 5
	~9,900		54 ± 5
	~10,400		55 ± 5
Psyche FM029	~40	~10	58 ± 5
Psyche FM030			60 ± 5
Psyche FM031			58 ± 5
Psyche FM032			57 ± 5

SNYDER, J. S. ET AL. 2019.

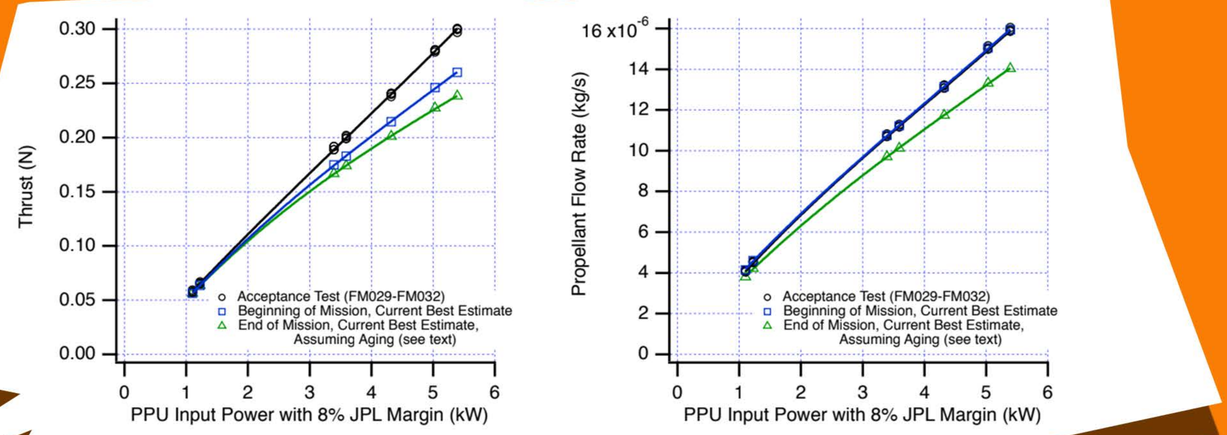

a) **Thrust Curve.** b) **Propellant Flow Rate Curve.**

Fig. 11. Current-Best-Estimate Throttle Curves for Mission Design.

SNYDER, J. S. ET AL. 2019.

Table 2. Cathode Performance Characterization Data for 0.9 kW Discharge Power.

Parameter	Measured Value Psyche FM029	Psyche FM030	Psyche FM031	Psyche FM032	In-Family Range Based on Previous Testing
Cathode-to-Ground Voltage, V	-29.2	-28.5	-27.3	-28.9	-24 to -32
Cathode Keeper Voltage, V	17.8	18.3	16.5	17.3	20 to 27
Discharge Current Oscillations, A RMS	0.3	0.3	0.3	0.3	0.06 to 1.6

SNYDER, J. S. ET AL. 2019.

SNYDER, J. S. ET AL. 2019.

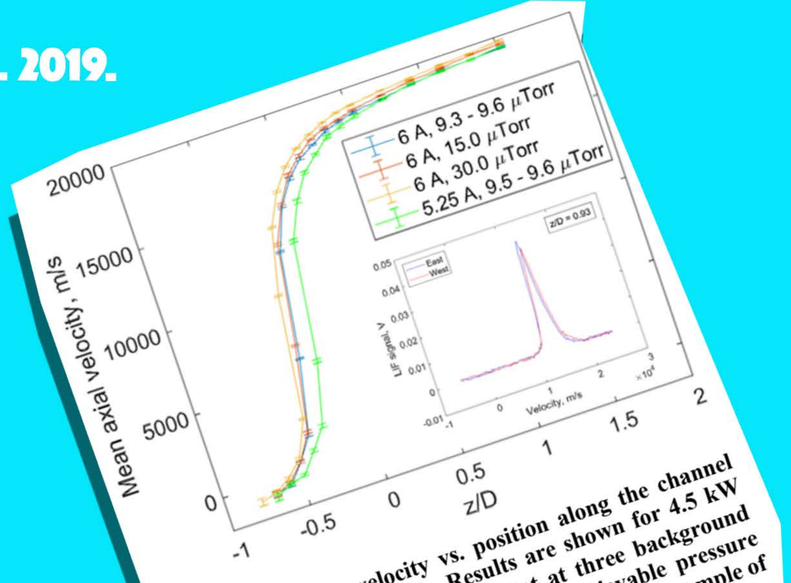

Fig. 7. Mean ion velocity vs. position along the channel centerline from LIF data. Results are shown for 4.5 kW operation with 6 A magnet current at three background pressures, and also at the minimum achievable pressure with 5.25 A magnet current. The inset shows an example of the measured IVDFs at one spatial location, from which the mean v_z was calculated.

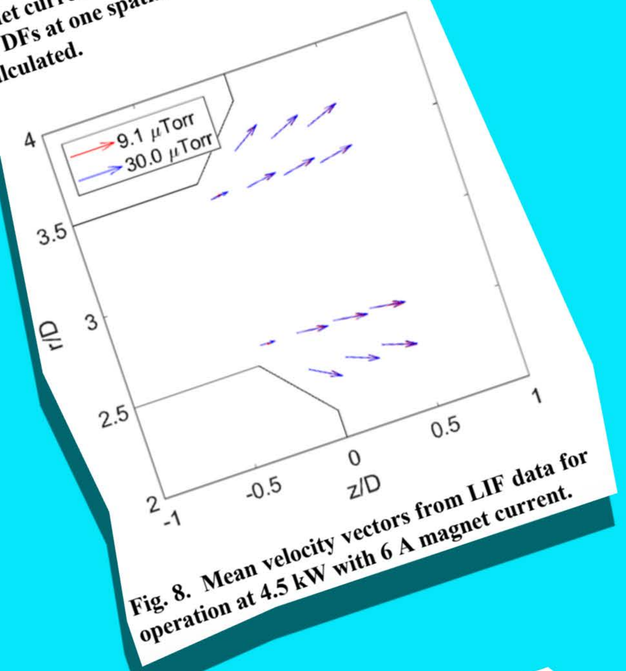

Fig. 8. Mean velocity vectors from LIF data for operation at 4.5 kW with 6 A magnet current.

SNYDER, J. S. ET AL. 2019.

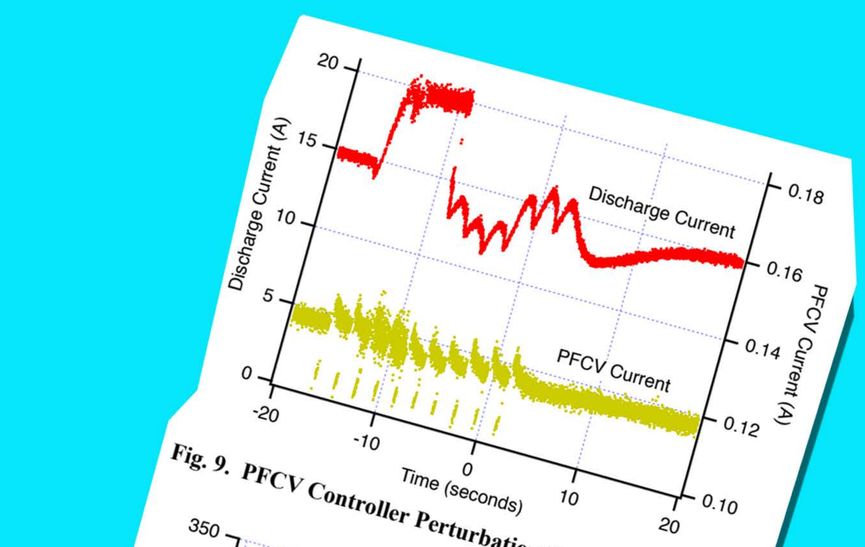

Fig. 9. PFCV Controller Perturbation Test.

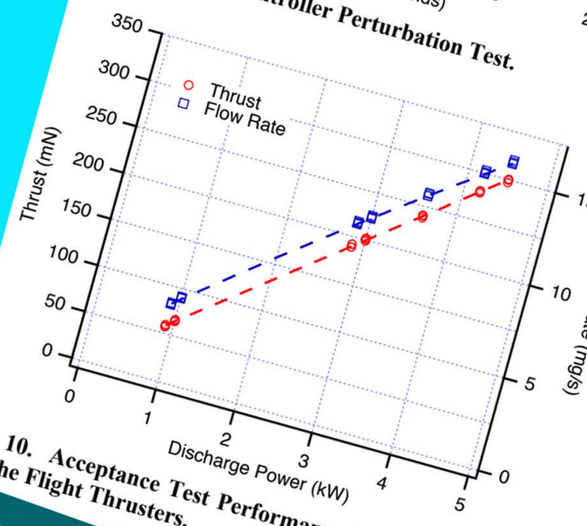

Fig. 10. Acceptance Test Performance Data for the Four Psyche Flight Thrusters.

SNYDER, J. S. ET AL. 2019.

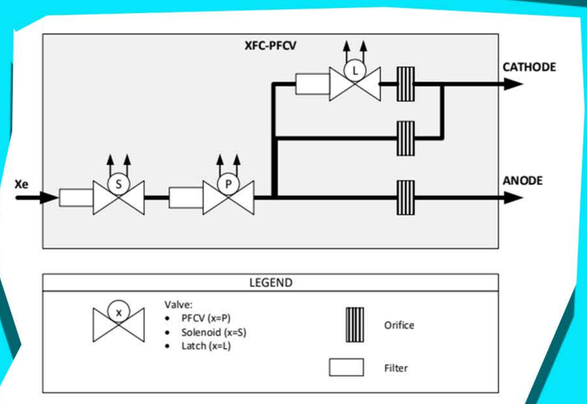

Fig. 6. Psyche Xenon Flow Controller Schematic.

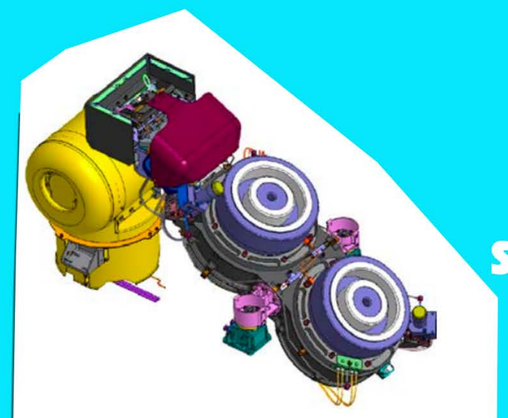

Fig. 5. Thruster Gimbal Module (i.e. DSM).

SNYDER, J. S. ET AL. 2019.

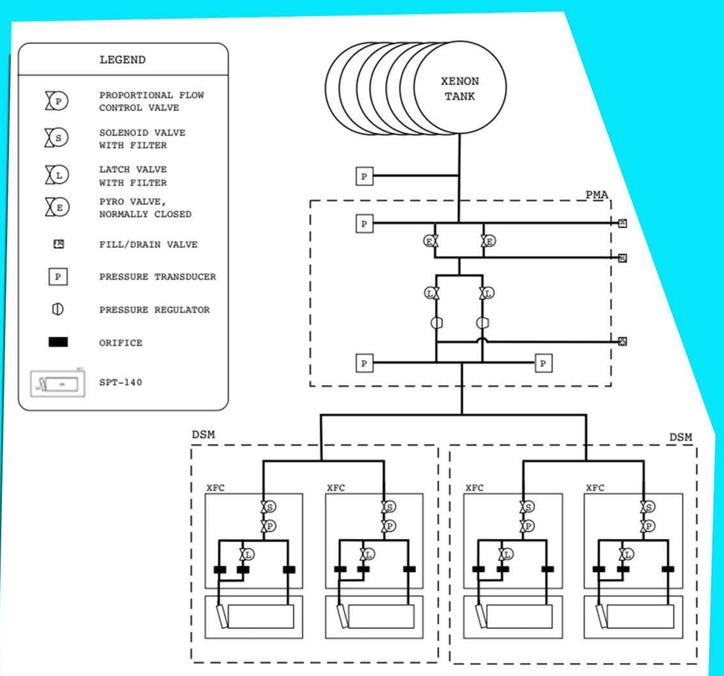

Fig. 4. Electric Propulsion System Pneumatic Diagram.

SNYDER, J. S. ET AL. 2019.

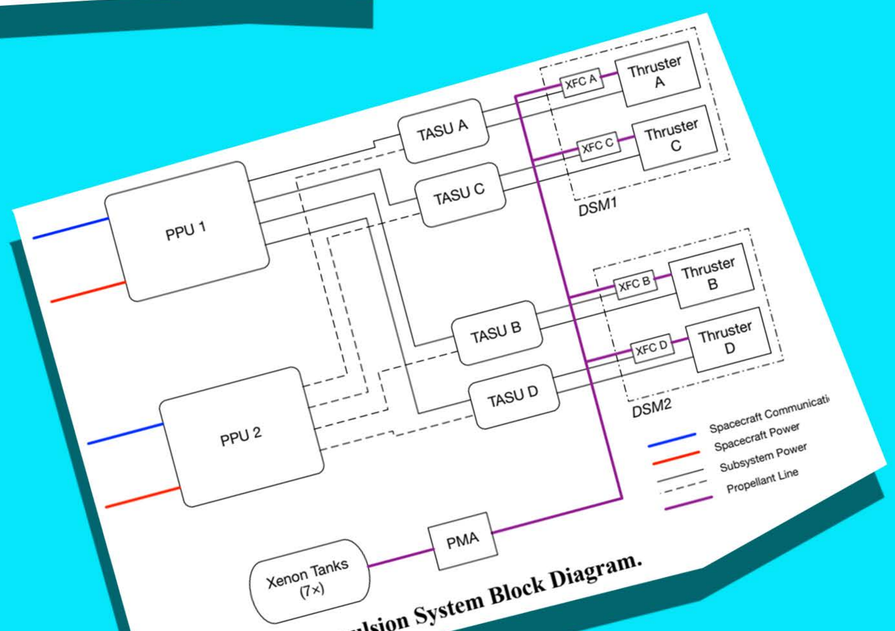

Fig. 3. Electric Propulsion System Block Diagram.

SNYDER, J. S. ET AL. 2019.

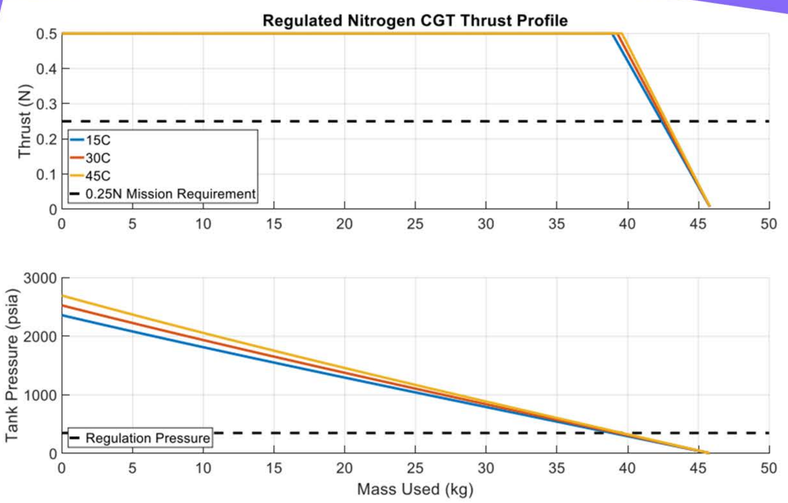

Figure 19: Cold Gas Thruster subsystem thrust and pressure curves vs. mass usage.

	Mass (kg)
Maximum Potential Load Mass (2700psi, 45C)	**45.9**
Launch Detumble	0.9
Initial Checkout/Commissioning	0.2
Momentum Management	2.4
Allocated Leak	2.1
Tank Residuals	6.9
Minimum Required Load for Nominal Mission	**12.5**
If Loaded, Available Nitrogen Propellant for Contingencies	**33.4**

Table 9: Nitrogen Cold Gas propellant budget

OH, D. ET AL. 2019.

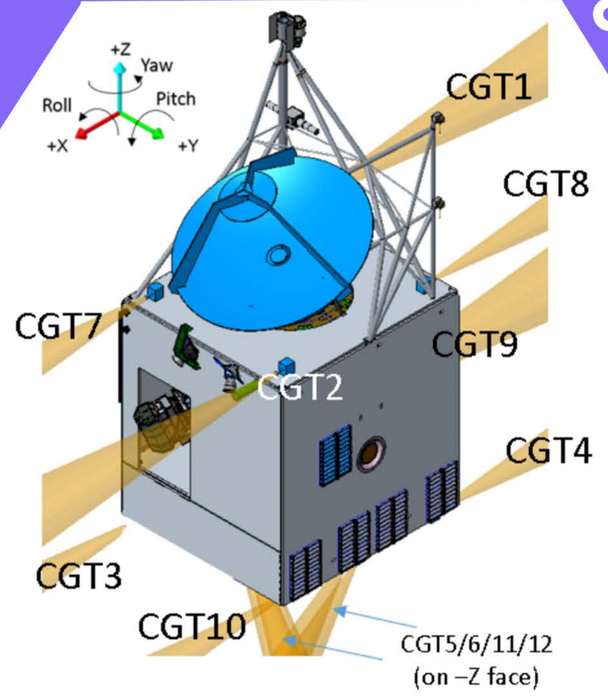

Figure 18: Placement of Cold Gas Thrusters on the Psyche spacecraft

OH, D. ET AL. 2019.

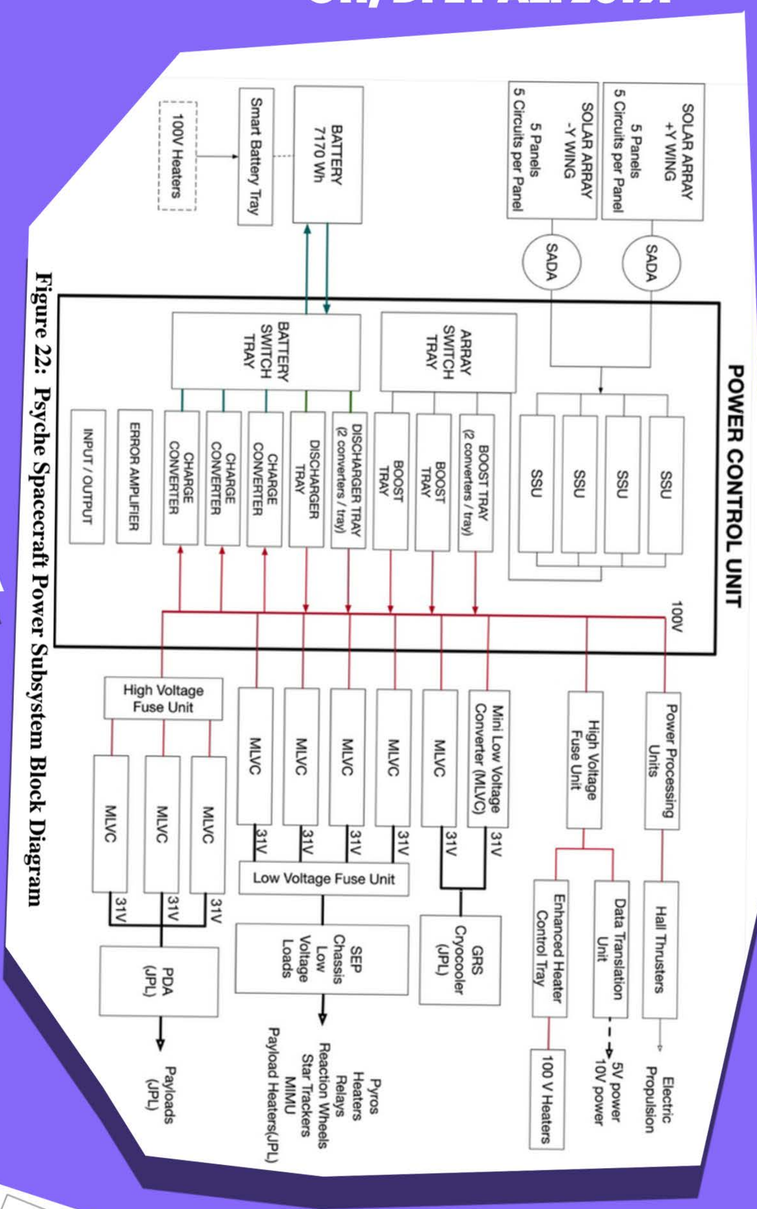

Figure 22: Psyche Spacecraft Power Subsystem Block Diagram

OH, D. ET AL. 2019.

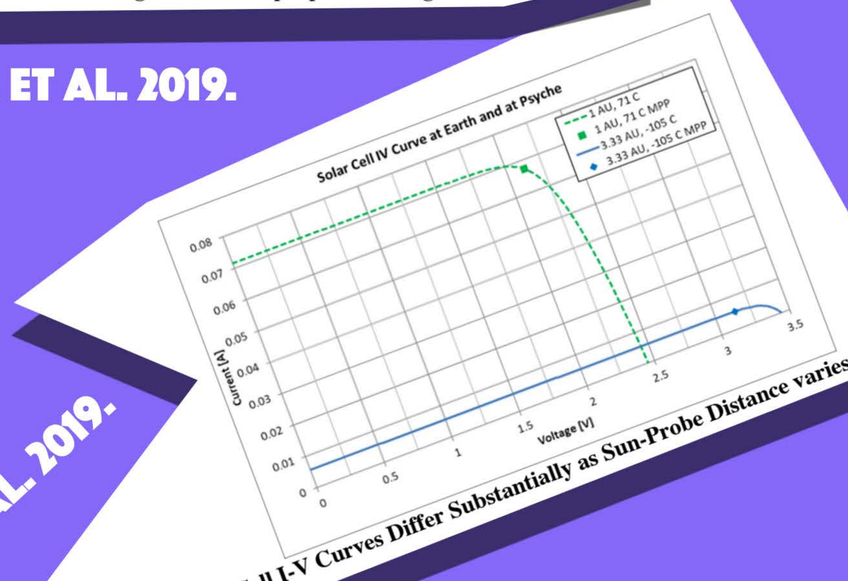

Figure 20: Solar Cell I-V Curves Differ Substantially as Sun-Probe Distance varies from 1 AU to 3.33 AU

OH, D. ET AL. 2019.

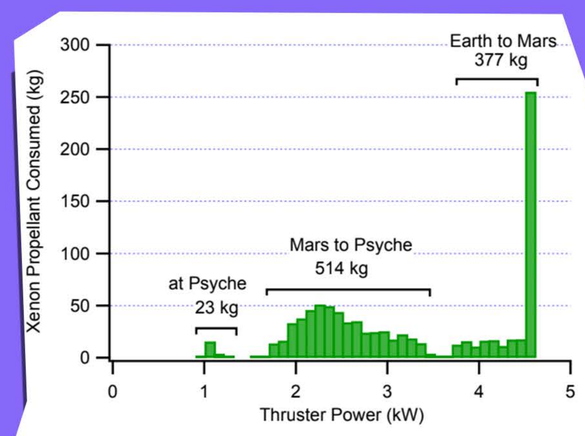

Fig. 2. Thruster Throughput for Baseline Trajectory at Project PDR.

Table 1. Xenon Propellant Budget at Project PDR.

Usage Category	Propellant Allocation, kg
Deterministic Cruise	885.0
Cruise Momentum Management	5.0
Capture to Orbit A	6.4
Orbit Transfer: A to B	2.4
Orbit Transfer: B to C	1.8
Orbit Transfer: C to D	15.8
Orbit Maintenance	2.5
Non-Usable Propellant (residuals, leakage, fill error, thruster startup/shutdown, initial checkout)	38.9
Margin: Missed Thrust	35.4
Margin: Thruster Performance Uncertainties	36.8
Total	**1030.0 kg**

SNYDER, J. S. ET AL. 2019.

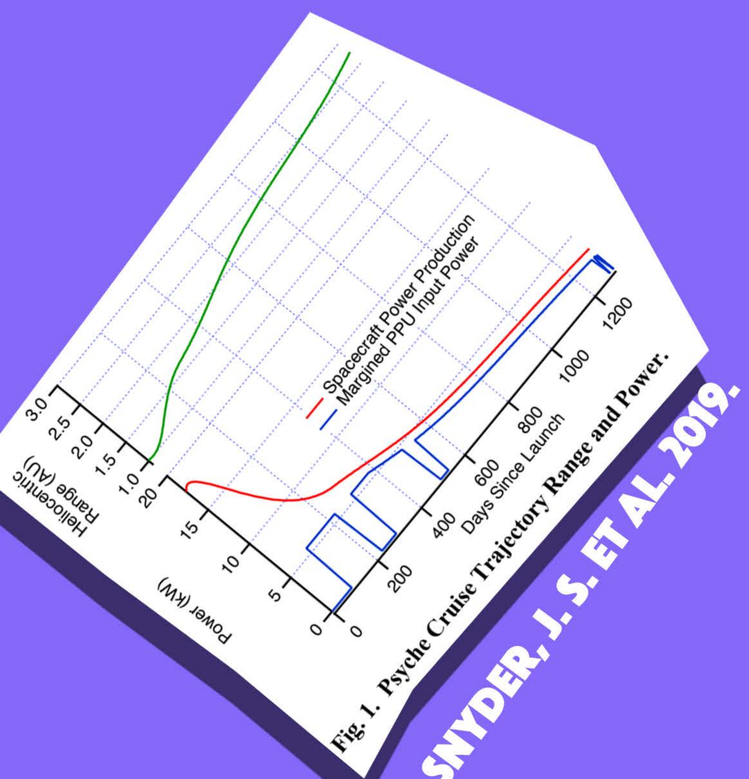

Fig. 1. Psyche Cruise Trajectory Range and Power.

SNYDER, J. S. ET AL. 2019.

OH, D. ET AL. 2019.

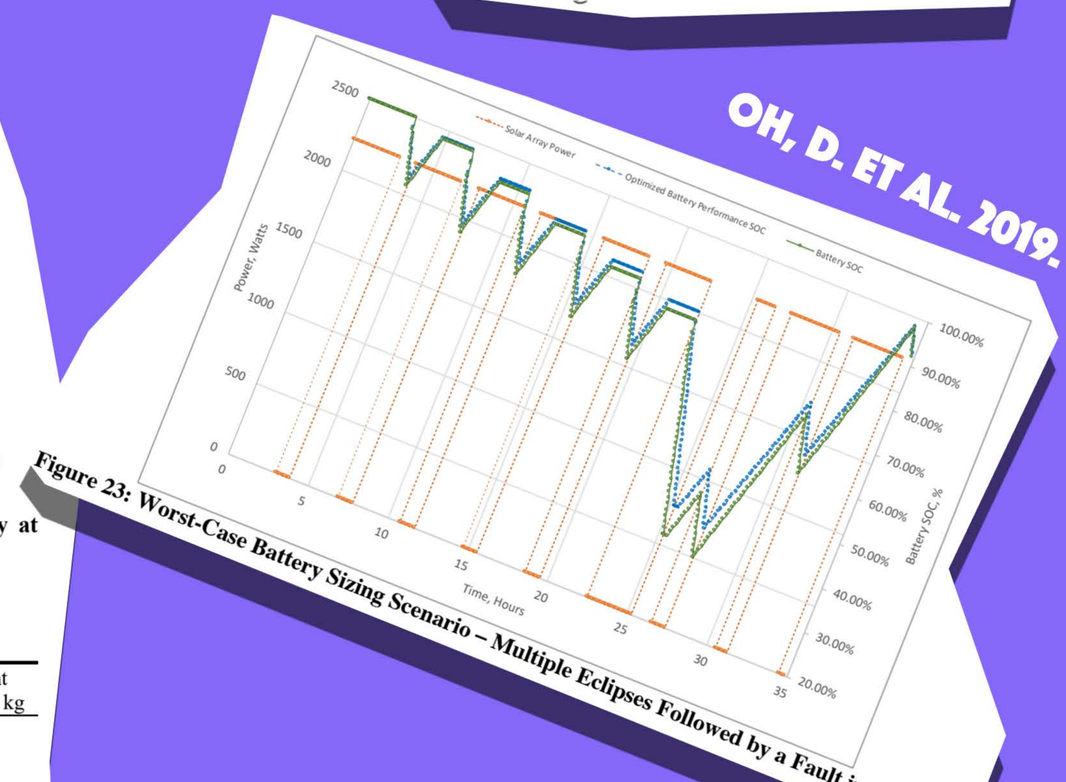

Figure 23: Worst-Case Battery Sizing Scenario – Multiple Eclipses Followed by a Fault in Orbit D

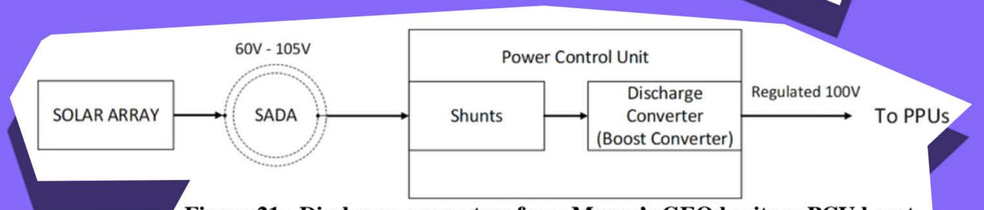

Figure 21: Discharge converters from Maxar's GEO heritage PCU boost Solar Array Voltage and Create 100 V Regulated Power for the PPU

OH, D. ET AL. 2019.

Requirement		Rationale
Fault tolerance	Single	Allows for a single hardware failure without impacting mission
Tank capacity	>45kg	Allows for multiple 3-sigma contingency scenarios if fully loaded. Final decision on loaded mass is not required until late in the build.
Minimum propellant load	12.5kg	Budget for propulsive maneuvers not feasible via Hall Thrusters, hold-up, leakage
Torque across any axis	>0.5N-m	Allows for contingency mitigation under required durations
Thrust	>0.25N	
Minimum impulse bit	<32mN-sec	Allows for dead-banding and precise momentum management

Table 8: Overview of Psyche Cold Gas Subsystem Requirements

OH, D. ET AL. 2019.

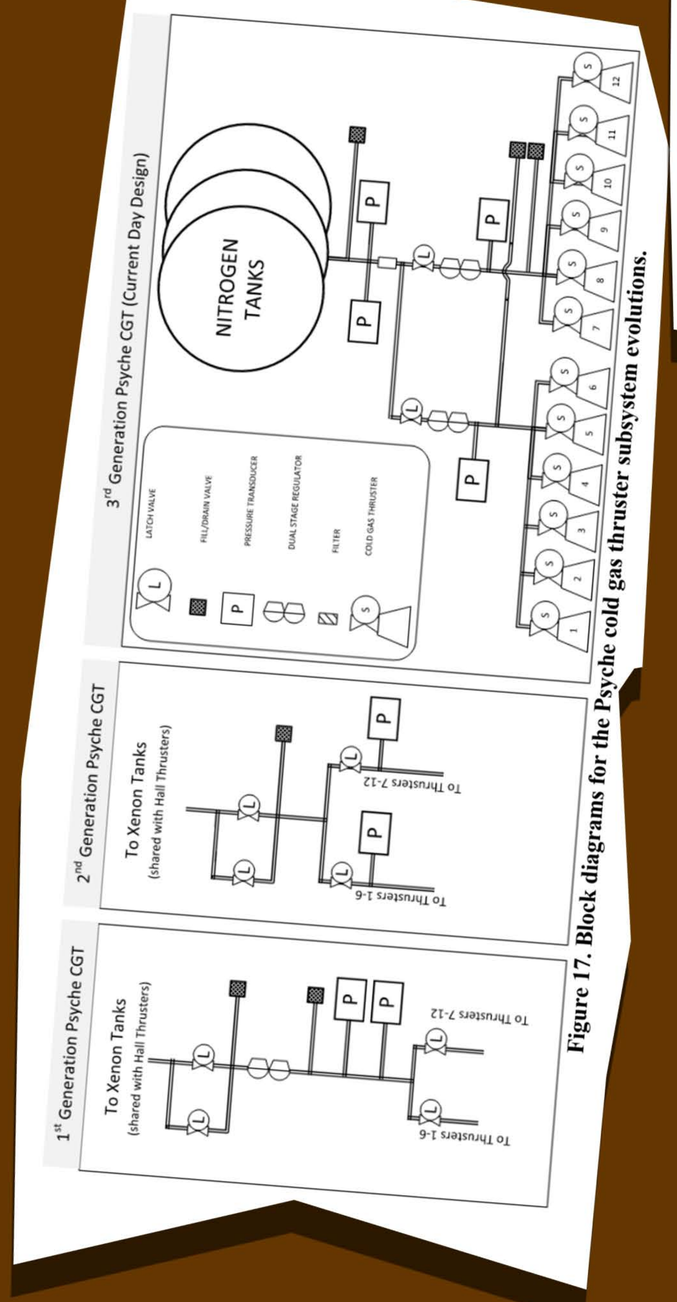

Figure 17. Block diagrams for the Psyche cold gas thruster subsystem evolutions.

OH, D. ET AL. 2019.

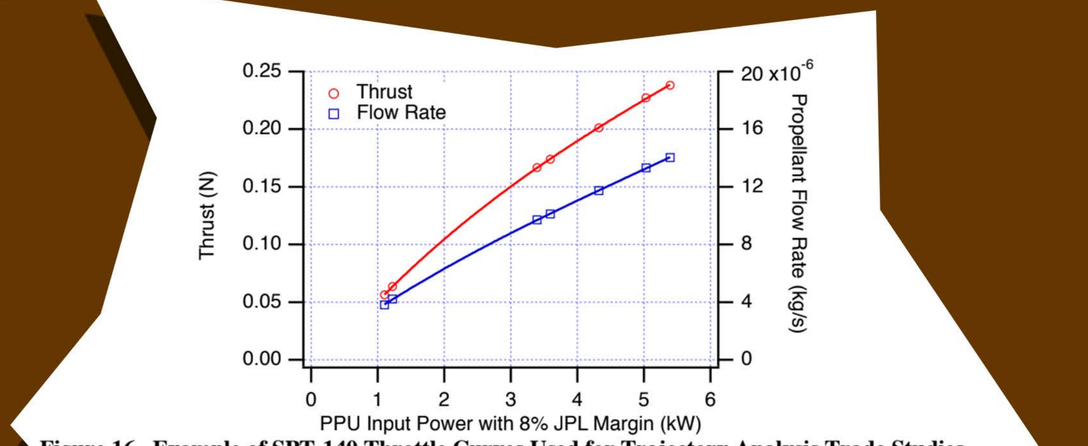

Figure 16. Example of SPT-140 Throttle Curves Used for Trajectory Analysis Trade Studies.

OH, D. ET AL. 2019.

Table 7: Planned Usage of Electric Propulsion and Cold Gas Propulsion Systems for Psyche

	Electric Propulsion	Cold Gas
Launch		
Post-Launch Detumble and Sun Acquisition		X
Cruise		
Primary Propulsion	X	
Momentum Management	X	
Asteroid Orbital Ops (Prox Ops)		
Orbit Transfers	X	
Orbit Maintenance	X	
Momentum Management	X	
Off-Nominal Scenarios		
Safe Mode Wheel Desaturation	X	
Safe Mode Turns	X	

OH, D. ET AL. 2019.

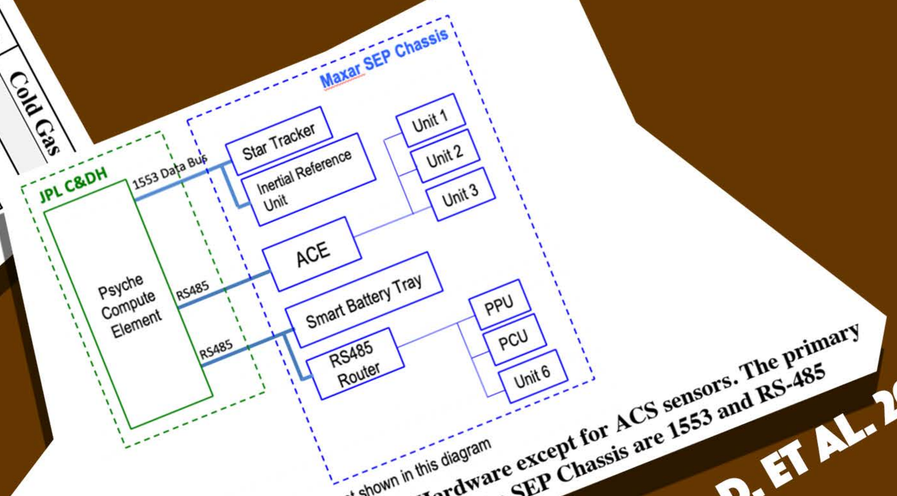

Figure 14: Maxar C&DH Units control all SEP Chassis Hardware except for ACS sensors. The primary interfaces between JPL provided Compute Element and the SEP Chassis are 1553 and RS-485

OH, D. ET AL. 2019.

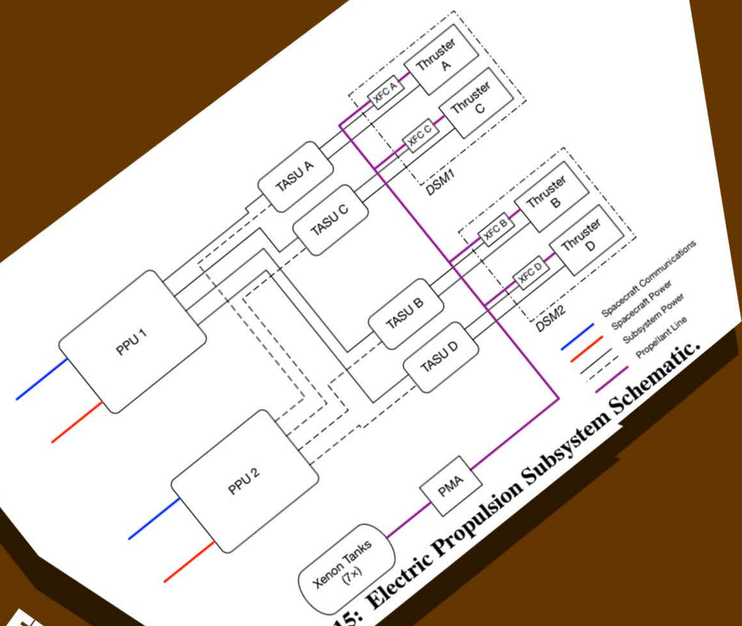

Figure 15: Electric Propulsion Subsystem Schematic.

OH, D. ET AL. 2019.

Figure 13: Central Cylinder Structure for the Psyche Spacecraft

OH, D. ET AL. 2019.

	PDR March 2019	CDR April 2020	SIR Dec 2020	Launch August 2022
Bus Dry Mass Margin	15%	7%	4%	0%
Bus Power Margin	20%	15%	10%	10%
Xenon Propellant Mass Margin	8%	4%	4%	4%
Electric Propulsion Power Margin	12%	5%	5%	5%

Table 6: Lifecyle Requirements for Mass and Power Margin

OH, D. ET AL. 2019.

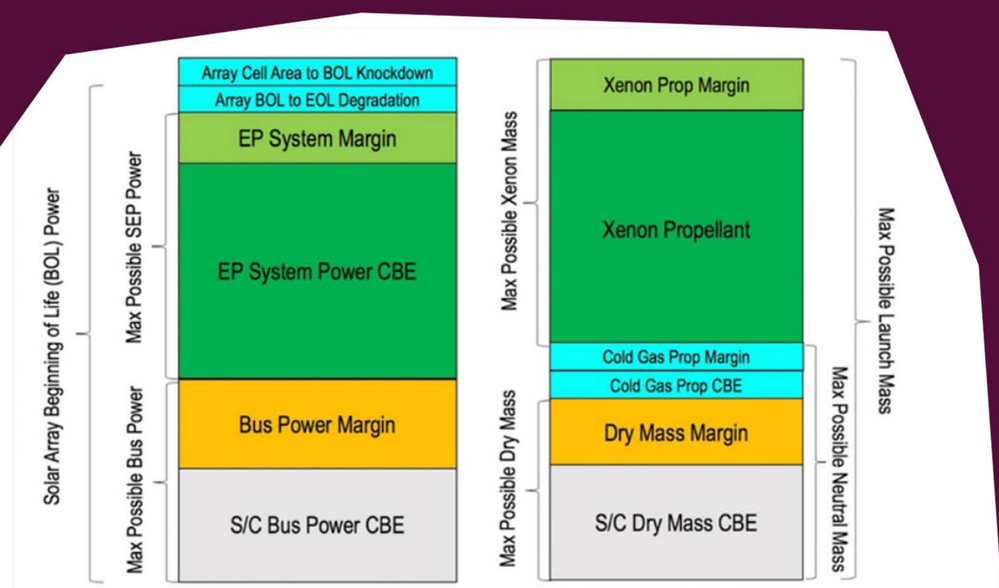

Figure 10: Power and Mass Margins for the Bus and Electric Propulsion System

Nominal Thrust Duty Cycle
Up to 80% duty cycle between Earth and Mars
Up to 85% duty cycle between Mars and Psyche
Up to 50% duty cycle during Psyche Approach and Orbital Operations
Off-Nominal Missed Thrust Accommodation
Tolerate 16 days of missed thrust per year
Tolerate 10 day missed thrust outage at any time
Tolerate 22 day missed thrust outage during solar conjunctions

Table 5: Requirements for Trajectory Robustness

OH, D. ET AL. 2019.

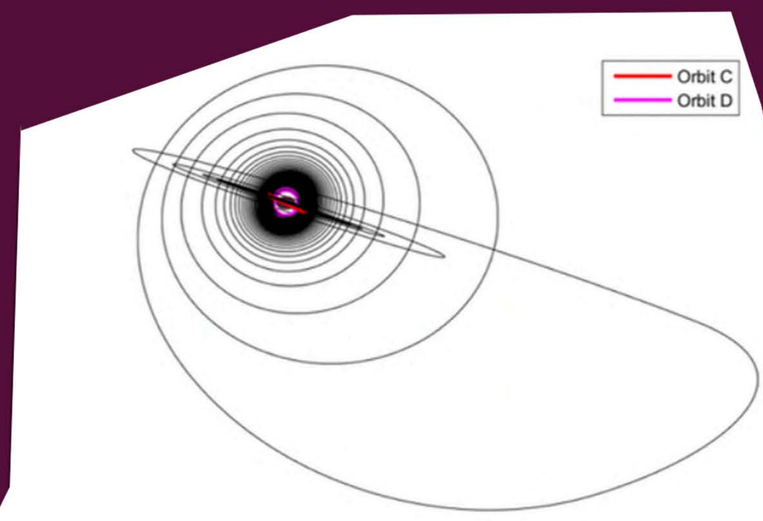

Figure 9: Polar View of Reference Transfer to Orbit D

OH, D. ET AL. 2019.

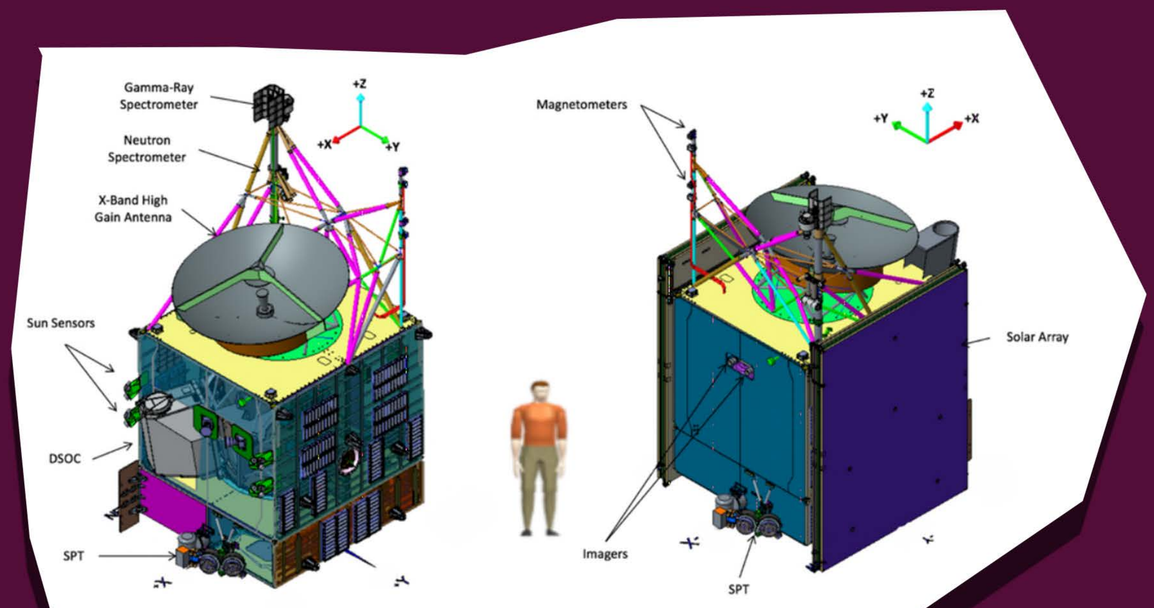

Figure 11: Psyche Spacecraft Overview

OH, D. ET AL. 2019.

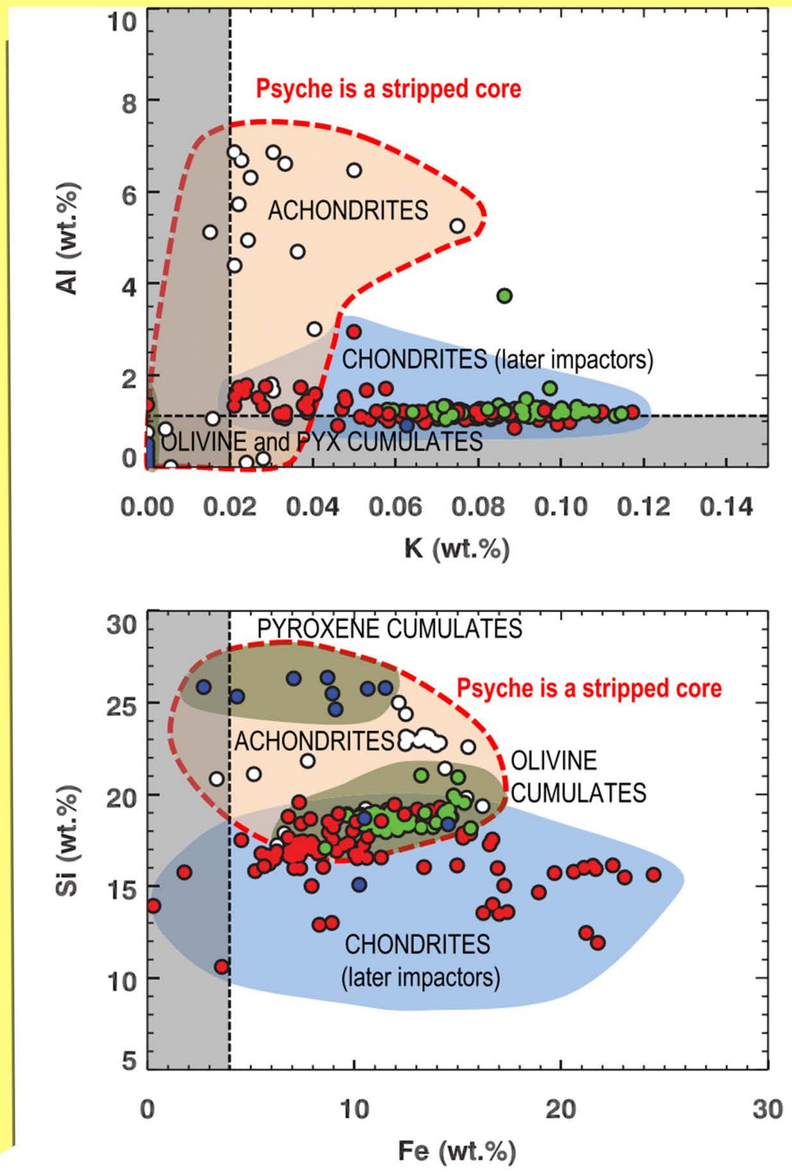

Figure 4. The elemental compositions of silicates that may be detected on Psyche can be used via GRNS data to constrain formation models for Psyche. Pyroxenes and olivines dominating a region are assumed to be cumulate material from solidification of a planetesimal magma ocean. Therefore, they would likely be from Psyche's parent body's mantle and, thus, indicate that Psyche is the remnants of a differentiated planetesimal. Extensive achondritic material would be assumed to be the bulk silicate mantle or lid from Psyche's parent body, fallen back during stripping impacts, and also therefore indicate that Psyche is the remnants of a differentiated planetesimal. Chondritic material lying atop metal, in contrast, would likely be accreted by later impacts and therefore would not be indicative of Psyche's formation process. The grey bands block compositions below the detection limit of Psyche instruments. Chondrite and achondrite compositional data from Jarosewich (1990); pyroxene and olivine from pallasites and IIE irons from Mittlefehldt et al. (1998); orthopyroxenes from Steinbach meteorite from Scott et al. (1996). In addition to the natural materials, the olivine cumulate date in the Si versus Fe figure also includes compositions of modeled olivines each calculated as the first-solidifying phase with Fe-Mg K_D of 0.32 from a hypothetical bulk silicate magma ocean composed of the total oxides of a chondrite measured by Jarosewich (1990).

ELKINS-TANTON, L., ET AL. 2019.

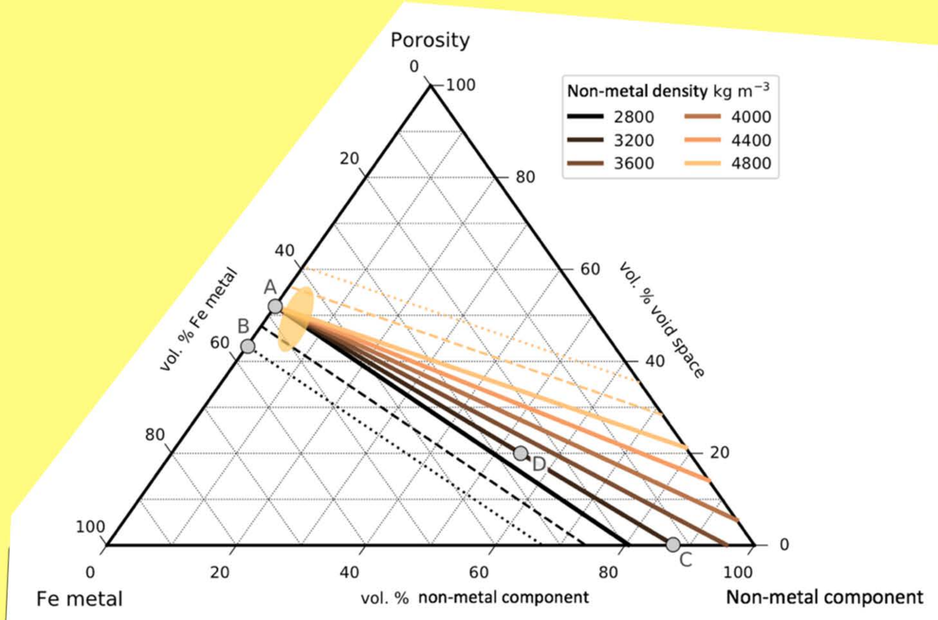

Figure 3. Interpretation of the bulk density of Psyche as a mixture of iron-nickel metal, a nonmetal component, and porosity implies that Psyche's metal content may be between ~30 and 55 vol%. The bulk density used is 3,780 ± 340 kg m^{-3}, the density of metal that of kamacite (7,870 kg m^{-3}), and the density of the nonmetal varied from 2,800 to 4,800 kg m^{-3} (see text). Each solid line shows the possible makeup using a different nonmetal density, and the dashed and dotted lines show how the results change when using the 1σ and 2σ limits of the bulk density. The yellow oval marks regions where nonmetals total 10% of the solid, as suggested by remote sensing (see text). At point A, Psyche consists solely of 48% metal and 52% pore space. At the 2σ of our density estimate, point B reaches 57% metal and 43% pore space. Point C represents another end-member possibility, where there is no porosity in Psyche, and metal combined with enstatite at 3,200 kg m^{-3} implies a maximum of ~13% metal by volume. The addition of 20% porosity increases the abundance of iron metal from 13% to 27% (point D).

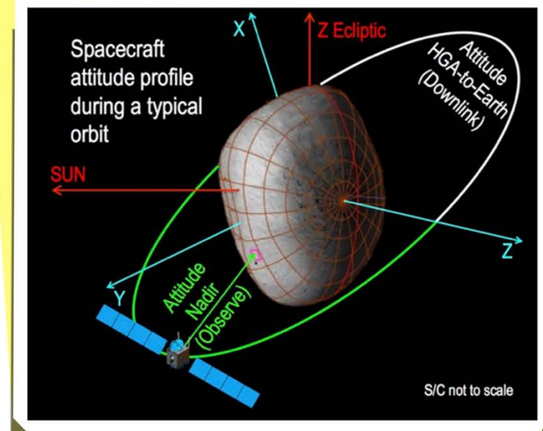

Fig. 2 Attitude strategy for a single orbit.

POLANSKEY, C. ET AL. 2018.

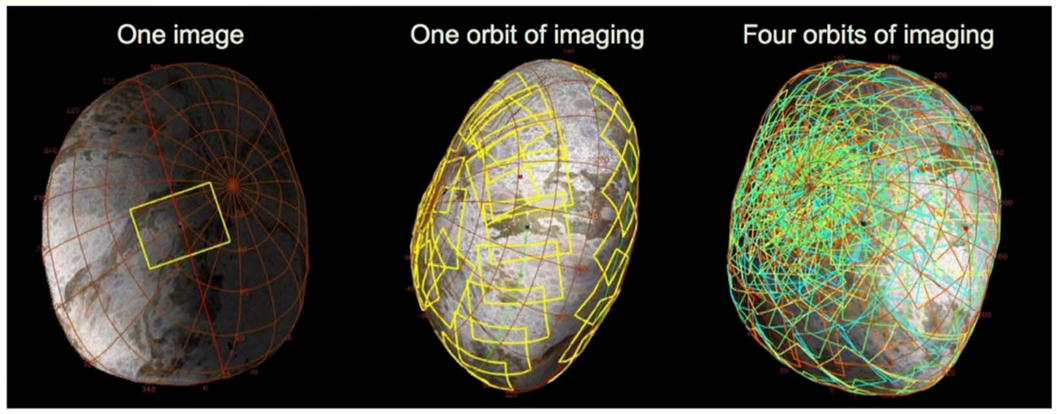

Fig. 3. Orbit A imaging provides complete coverage in four orbits (six days).

POLANSKEY, C. ET AL. 2018.

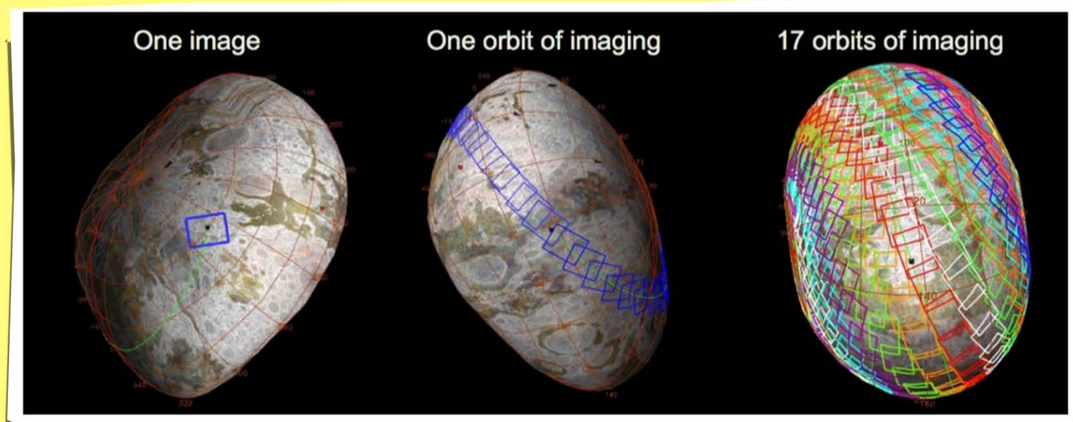

Fig. 4 Orbit B imaging provides complete coverage in 17 orbits.

POLANSKEY, C. ET AL. 2018.

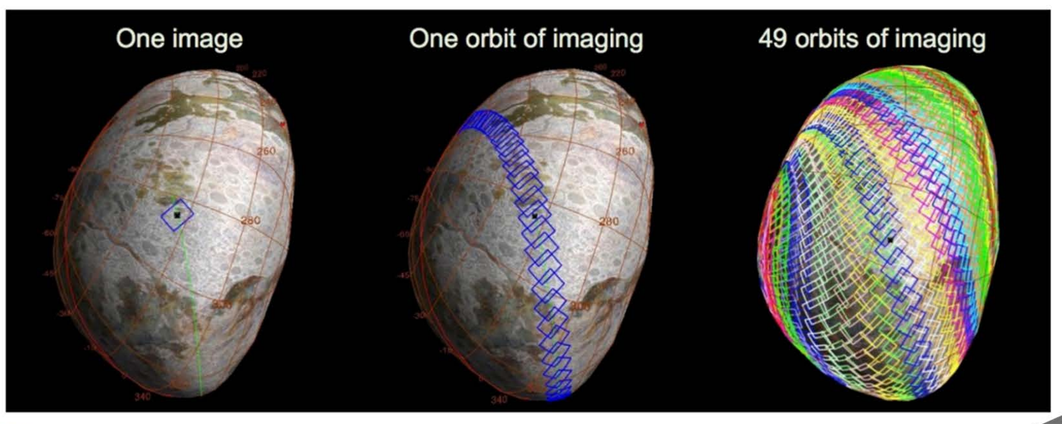

Fig. 6 Orbit C imaging provides complete coverage in 49 orbits.

POLANSKEY, C. ET AL. 2018.

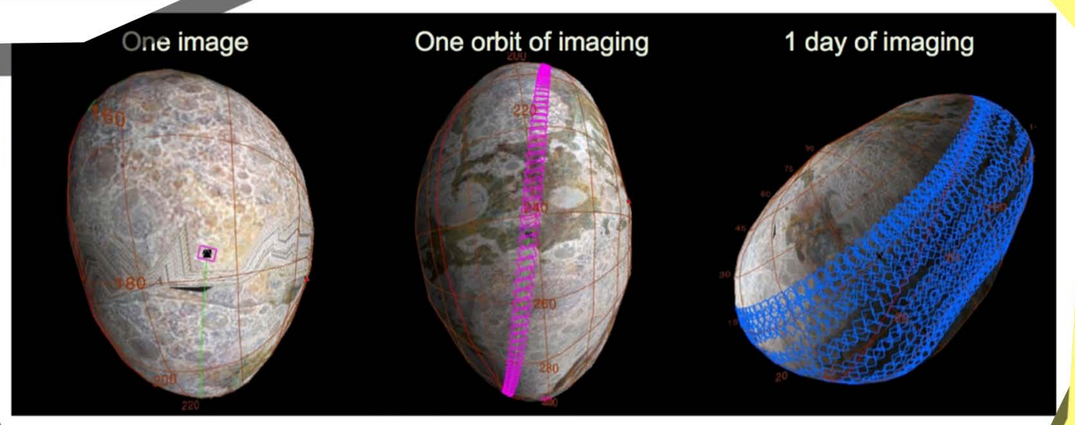

Fig. 7 Orbit D imaging provides high resolution coverage near the equator.

POLANSKEY, C. ET AL. 2018.

BPG 14

STUDENT WORK INCORPORATED

ESSENCE OF PSYCHE
AARTI PATEL
COVER PAGE

SOLIDARITY WITH PSYCHE
NOAH KEIME
COVER PAGE

EMPATHY
CHRISTINE ZHOU
PAGE 2

IMPACTING THE FUTURE
LEVI KEATTS
PAGE 5

ORBITING THE UNKNOWN IN VR
WILLIAM STRUNK
PAGE 5

TRAJECTORY: READY, SET, GO.
JULIA GRETEMAN
PAGE 5

METAL CLOUDS
FINN WITT
PAGE 5

MEETING PSYCHE
CHASE MORTENSEN
PAGE 5

PSYCHE DESIGNS 1, 2, 3
SOPHIE HULLINGER
PAGE 5

BREAKING BARRIERS
CHLOE CARRIERE
PAGE 5

THE FORMATION OF PSYCHE
BRIANNA YOUNG
PAGE 5

BEADED ORBITS
SHANNON HACK
PAGE 5

WHAT IS THE NASA PSYCHE MISSION?
JOYCE TSUI
PAGE 5

MAGNETIC FIELD
MONICA MORENO
PAGE 5

HELLO, PSYCHE
CHASE MORTENSEN
PAGE 5

A MAGICAL EXPEDITION
SHANNON HACK
PAGE 5

LIGHT CURVES
LEVI KEATTS
PAGE 5

IN 2026
JOYCE TSUI
PAGE 5

PSYCHE JOURNEY
SILVIA VALLADARES
PAGE 5

PSYCHE TWINKLES
SHANNON HACK
PAGE 5

ORBIT KINETIC RING
MONICA MORENO
PAGE 5

PSYCHE: DISCOVERY TO EXPEDITION
SOPHIE HULLINGER
PAGE 5

INTERVIEW WITH PSYCHE: PART 1
ANNA VANDERBERG
PAGE 5

THE SPACECRAFT
OLIVIA FERREL
PAGE 5

ORBIT
STACY WOODRUFF
PAGE 5

MILESTONES IN SPACE AND MUSIC EXPLORATION
CHLOE CARRIERE
PAGE 5

FLIPPING THROUGH PSYHCE
ANGELA WROBLEWSHKI
PAGE 5

PARTS AND PIECES
OLIVIA FERREL
PAGE 5

LATE NIGHT
MIGUEL MONTAÑEZ
PAGE 5

TRANSFER
RACHEL MCNEIL
PAGE 5

HEAVY METAL LIGHT SHOW
CHRIS VASQUEZ
PAGE 5

PIXELATED PSYCHE
SOFIA GARCIA
PAGE 5

AD ASTEROID
JANANI LAKSHMANAN
PAGE 5

UNTITLED
SILVIA VALLADARES
PAGE 5

PSYCHE'S PROJECTED ORBITS
FIONA SCHNEIDER
PAGE 5

VOYAGE
SHANNON HACK
PAGE 5

PSYCHE'S PROJECTED ORBITS
FIONA SCHNEIDER
PAGE 5

PSYCHE THROUGH THE MULTISPECTRAL IMAGER
RAL VANDENHOUDT
PAGE 5

PLANT YOUR SEED
RACHEL MCNEIL
PAGE 5

INTERVIEW WITH PSYCHE PART 3
ANNA VANDERBERG
PAGE 5

BACKYARD TELESCOPE
CARALIE CEDARLEAF
PAGE 6

IMPACT
BINH-AN NGUYEN
PAGE 8

HEART OF GOLD
SAM HOLLASCH
PAGE 11

PSYCHE'S JOURNEY
BEN CONWAY
PAGE 14

References

Biswas, A., Srinivasan, M. Piazzolla, S. Hoppe, D. 2014. *Deep Space Optical Communications*.

Elkins-Tanton, L., Asphaug, E., Bell III, J. F., Bercovici, H., Bills, B., Binzel, R., Bottle, W. F., Dibb, S., Lawrence, D. J., Marchi, S., McCoy, T. J., Oran, R., Park, R. S., Peplowski, P. N., Polansky, C. A., Prettyman, T. H., Russell, C. T., Schaefer, L., Weiss, B. P., Wieczorek, M. A., Williams, D. A., Zuber, M. T. 2019. *Observations, Meteorites, and Models: A Preflight Assessment of the Composition and Formation of (16) Psyche*.

Lenguito, G., Neff, K., Barbarits, J., Snyder, J. S., Chaplin, V. 2019. *Versatile Xenon Flow Controller for Extended Hall-Effect Thruster*

Malone, S., Aghazadeh, F., Lenguito, G., Staley, M., Kerl, T., Tomescu, B., Snyder, J. S. 2019. *Deep Space Power Processing Unit for the Psyche Mission*.
Power Range.

Mikellides, I., Lopez Ortega, A., Chaplin, V. H., Snyder, J. S., Lenguito, G. 2019. *Mechanism Behind the Dependence of Thrust on Facility Backpressure and Implications on the Operation of the SPT-140 Onboard the Psyche Mission*.

Oh, D., Collins, S., Drain, T., William, H., Imken, T., Larson, K., Marsh, D., Muthulingam, D., Snyder, J. S., Trofimov, D. 2019. *Development of the Psyche Mission for NASA's Discovery Program*.

Lopez Ortega, A., Mikellides, I. G., Chaplin, V. H., Snyder, J. S., Lenguito, G. 2019. *Facility Pressure Effects on a Hall Thruster with an External Cathode, I: Numerical Simulations*.

Polanskey, C. A., Marsh, D. M., Moore, R. R., Park, R. S., Soria-Santacruz Pich, M., Wenkert, D., Elkins-Tanton, L.

T., Williams, D. A., Jaumann, R., Russell, C. T., et al. 2018. *Psyche Science Operations Concept: Maximize Reuse to Minimize Risk*.

Snyder, J. S., Goebel, D. M., Chaplin, V., Lopez Ortega, A., Mikellides, I. G., Aghazadeh, F., Johnson, I., Kerl, T., Lenguito, G. 2019. *Electric Propulsion for the Psyche Mission*.